Old Dominion University
ODU Digital Commons

Electrical & Computer Engineering Theses & Disssertations

Electrical & Computer Engineering

Winter 2011

Hybrid Inorganic/Organic Nanostructured Tandem Solar Cells: Simulation and Fabrication Methods

Patrick Michael Boland Jr.
Old Dominion University

Follow this and additional works at: https://digitalcommons.odu.edu/ece_etds

Part of the Chemical Engineering Commons, Electrical and Computer Engineering Commons, and the Oil, Gas, and Energy Commons

Recommended Citation
Boland, Patrick M.. "Hybrid Inorganic/Organic Nanostructured Tandem Solar Cells: Simulation and Fabrication Methods" (2011). Doctor of Philosophy (PhD), dissertation, Electrical/Computer Engineering, Old Dominion University, DOI: 10.25777/kd3d-ga57
https://digitalcommons.odu.edu/ece_etds/44

This Dissertation is brought to you for free and open access by the Electrical & Computer Engineering at ODU Digital Commons. It has been accepted for inclusion in Electrical & Computer Engineering Theses & Disssertations by an authorized administrator of ODU Digital Commons. For more information, please contact digitalcommons@odu.edu.

HYBRID INORGANIC/ORGANIC NANOSTRUCTURED TANDEM SOLAR CELLS: SIMULATION AND FABRICATION METHODS

by

Patrick Michael Boland Jr.
B.S.E. December 1990, University of South Carolina
M.E.M. August 1995, Old Dominion University

A Dissertation Submitted to the Faculty of
Old Dominion University in Partial Fulfillment of the
Requirements for the Degree of

DOCTOR OF PHILOSOPHY

ELECTRICAL AND COMPUTER ENGINEERING

OLD DOMINION UNIVERSITY
December 2011

Approved by:

Gon Namkoong (Director)

Helmut Baumgart (Member)

Ravindra Joshi (Member)

Tarek Abdel-Fattah (Member)

ABSTRACT

HYBRID INORGANIC/ORGANIC NANOSTRUCTURED TANDEM SOLAR CELLS: SIMULATION AND FABRICATION METHODS

Patrick Michael Boland Jr.
Old Dominion University, 2011
Director: Dr. Gon Namkoong

Organic solar cell technologies continue to be an extremely active area of scientific research. With their promise of providing low-cost, easily-processable, multi-application photovoltaics, these devices could very possibly be the most viable and practical form of renewable energy among many being explored. However, significant technological obstacles remain that must be overcome if this technology is to successfully realize the goal of providing abundant energy while simultaneously reducing dependence on fossil fuel-based sources. Compared with *inorganic* solar photovoltaics, power conversion efficiencies in organics are still too low to compete economically.

Much research has been accomplished over the past three decades in an attempt to optimize the performance characteristics of planar organic solar cell devices. Unfortunately, the limitations of device physics and the optical and electrical characteristics inherent in semiconducting polymers restrict the achievable efficiency for this type of structure. A "next generation" approach to surmounting this shortcoming is to stack multiple planar devices in such a way that enhanced performance is achieved. This tactic requires *hybridization* through the inclusion of inorganic metal oxide components that serve a number of functions such as electron and/or hole transporters/blockers and optical spacers. In this work, these "tandem" devices are modeled and their functionality simulated using computer-based algorithms in an effort

to ascertain the ideal structural, optical, and electrical properties that must be designed into actual hybrid inorganic/organic photovoltaic devices. Additionally, several solar cells are fabricated and the methods described to show the many factors to be accounted for and controlled to achieve high-efficiency devices.

Results produced in this study show that hybrid inorganic/organic solar cells can significantly improve power conversion efficiency over standard planar devices – simulated results show efficiencies over 9% are possible. Such factors as electron and hole mobilities, structural layer thicknesses, and choice of polymer and fullerene materials were found to be critical to the optimization of these structures. A key finding is that charge carrier mobilities in the subcells must be balanced so that space charge current limitations are avoided, thereby ensuring the maximum achievable current through the tandem structures.

Hybrid inorganic/organic solar cells have tremendous promise as an alternative means of renewable energy production. Modeling and simulation are valuable tools that allow for the assessment of a multitude of various interdependent factors that impact the performance of these devices. By conducting this type of analysis prior to fabricating actual solar cells, considerable time and materials resources can be conserved while, at the same time, rapid prototyping can be accomplished and improvements in performance characteristics realized more quickly.

To my wife, Julie, and my two sons, Andrew and Robert, for their love, support and patience as we persevered through our shared "odyssey" toward whatever comes next.

ACKNOWLEDGMENTS

I thank my teacher, advisor, and mentor, Dr. Gon Namkoong, for his wisdom, guidance, and patience during my journey toward achieving this Ph.D. He's been a guiding force, an inspiration, and a true blessing to me and my family.

I gratefully acknowledge my committee members, Dr. Helmut Baumgart, Dr. Ravindra Joshi, and Dr. Tarek Abdel-Fattah for their for their insights and recommendations to make this work better and more complete. They are scientists of the highest order.

A special thank you to Dr. Keejoo Lee for his remarkable work in creating the software code for our simulation program. His creation made so much excellent research possible.

My gratitude extends to those friends and colleagues who were there along the way; I appreciate your friendship, advice, and all the help. Thanks to Sampath Chennuri, Kevin Colvin, Dr. Shirshak Dhali, Kurniawan Foe, Pam Foshee, Dr. Diefeng Gu, Jefferson Lanier, Kevin Latimer, Linda Marshall, Hannah Matthews, Romina Samson, Sri Sabarinadh Sunkavalli, Dr. Kandabara Tapily, and Jessica Walker.

Finally, none of this would have been possible without the love and tireless support of the most important person in my life, my wife, Julie. We always get there in the end – we just have to go "round the houses". Thank you for always being there through the ups and downs and all my love for making the trip with me.

NOMENCLATURE

AFM	Atomic force microscopy
Ag	Silver
AGW	Anthropogenic global warming
Al	Aluminum
ALD	Atomic layer deposition
AM	Air mass
Ar	Argon
ASTM	American Society for Testing and Materials
BHJ	Bulk heterojunction
c	Speed of light = 3×10^8 m/s
Ca	Calcium
CA	Cellulose acetate
CDA	Clean dry air
CdTe	Cadmium telluride
CIGS	Copper indium-gallium diselenide
CO_2	Carbon dioxide
CT	Charge transfer (state)
CTZSSe	$Cu_2ZnSn(S,Se)_4$
$Cu(InGa)Se_2$	Copper indium-gallium diselenide
d_{bottom}	Thickness of the bottom cell
DIW	Deionized water

DOS	Density of states
d_{top}	Thickness of the top cell
DUT	Device under test
e	Elementary electronic charge (1.6×10^{-19} C)
E	Electric field
E_a	Activation energy
Ebeam	Electron beam evaporation
$E_{g,bottom}$	Energy bandgap, bottom subcell
$E_{g,top}$	Energy bandgap, top subcell
$E_{h\nu}$	Energy of a photon
EBL	Electron blocking layer
EQE	External quantum efficiency
eV	Electron volt
FBG	Fiber Bragg grating
FF	Fill factor
GaAs	Gallium arsenide
Ge	Germanium
G(z)	Photon absorption rate profile
h	Planck's constant = 6.626×10^{-34} m^2kg/s
H_20	Water
HBG	High bandgap
HBL	Hole blocking layer
HOMO	Highest occupied molecular orbital

I	Irradiance
I_{SC}	Short circuit current
I_{mpp}	Current at maximum power point
IPCE	Incident photon to current efficiency
IQE	Internal quantum efficiency
ITO	Indium tin oxide
IV	Current-voltage
J_{max}	Current density at the maximum power point
J_{ph}	Photocurrent density
J_{SC}	Short circuit current density
J-V	Current density-voltage
k_B	Boltzmann's constant = 1.38×10^{-23} J/K
LBG	Low bandgap
L_D	Exciton diffusion length
LED	Light-emitting diode
LUMO	Lowest unoccupied molecular orbital
meV	Milli electron volts
MoO_3	Molybdenum oxide
N_2	Nitrogen
NiO	Nickel oxide
nIR	Near infra-red
N_{ph}	Number of photons
NREL	National Renewable Energy Laboratory

O_2	Oxygen
OPV	Organic photovoltaic
OSC	Organic solar cell
P3HT	Poly-3 hexylthiophene
$PC_{61}BM$	[6,6]-phenyl C_{61}-butryic acid methyl ester
$PC_{71}BM$	[6,6]-phenyl C_{71}-butryic acid methyl ester
PCE	Power conversion efficiency
PCPDTBT	Poly[2,1,3-benzothiadiazole-4,7-diyl[4,4-bis(2-ethylhexyl)-4H-cyclopenta[2,1-b:3,4-b']dithiophene-2,6-diyl]]
PEDOT:PSS	Poly(ethylenedioxythiophene):poly(styrene sulfonate)
P_{in}	Incoming optical power
PL	Photoluminescence
P_{max}	Maximum solar power
ppm	Parts per million
P_{out}	Output electrical power
PV	Photovoltaic
q	Electron charge = 1.6×10^{-19} C
QD	Quantum dot
R_P	Parallel resistance
RR	Regioregular
R_S	Series resistance
R_{SH}	Shunt (parallel) resistance
SCLC	Space charge limited current
SEM	Scanning electron microscope

Si	Silicon
SMU	Source measurement unit
STC	Standard test conditions
T	Temperature in K
TCO	Transparent conductive oxide
TEM	Transmission electron microscopy
TiO_x	Titanium oxide
TMM	Transfer matrix method
UV	Ultraviolet
UV-VIS	Ultraviolet-Visible
V_2O_5	Vanadium oxide
V_{max}	Voltage at maximum power
V_{mpp}	Voltage at maximum power
V_{OC}	Open circuit voltage
WO_3	Tungsten trioxide
XPS	X-ray photoelectron spectroscopy
XRD	X-ray diffraction
ZnO	Zinc oxide
α	Absorption coefficient
β_L or η	Langevin recombination coefficient
ε_o	Permittivity of free space
ε_r	Relative permittivity
ϕ	Work function

μ_n	Electron mobility
μ_h	Hole mobility
η	Power conversion efficiency
λ	Wavelength
λ_B	Bragg reflectance wavelength
Λ_B	Bragg period

TABLE OF CONTENTS

Page

LIST OF TABLES.....xv

LIST OF FIGURES.....xvi

Chapter

I. INTRODUCTION.....1
MOTIVATION AND SCOPE OF RESEARCH.....1
RENEWABLE ENERGY SOURCES.....4
SOLAR AS THE PRIMARY RENEWABLE ENERGY.....6
ORGANIC BULK HETEROJUNCTION SOLAR CELLS.....10
HYBRID INORGANIC/ORGANIC DEVICES.....15
RELATED WORK.....18
ORGANIZATION.....19

II. THEORY.....21
SOLAR ENERGY CONVERSION IN ORGANIC POLYMERS.....21
CARRIER MOBILITY IN A GAUSSIAN DENSITY OF STATES.....35
CHARGE CARRIER RECOMBINATION.....46
OPTICAL AND ELECTRICAL MODELING.....52
ORGANIC/METAL OXIDE INTERFACES.....60

III. COMPUTER SIMULATION AND RESULTS.....69
OVERVIEW OF SIMULATIONS CONDUCTED.....69
OPTICAL SIMULATION: OPTIMIZING ACTIVE LAYER THICKNESS.....71
OPTIMIZING LOW-BANDGAP PCPDTBT:PCBM SOLAR CELLS.....79
ORGANIC TANDEM CELLS: LOW- & HIGH-BANDGAP DONOR POLYMERS.....92
ORGANIC TANDEM CELLS: PCPDTBT:PC_{61}BM & P3HT:PC_{71}BM SUBCELLS.....109

IV. FABRICATION METHODS AND CHARACTERIZATION.....122
FABRICATION FACTORS – LAYER-BY-LAYER.....122
INFLUENCE OF ANNEALING ON POLYMER BLEND PROPERTIES.....128
FABRICATION OF P3HT:$PC_{61/71}$BM PLANAR SOLAR CELLS.....137
FABRICATION OF PCPDTBT: $PC_{61/71}$BM PLANAR SOLAR CELLS.....139

FABRICATION OF P3HT:$PC_{61/71}BM$ & PCPDTBT: $PC_{61/71}BM$ TANDEM SOLAR CELLS.....141

V. CONCLUSION AND FUTURE WORK.....148
CONCLUSION.....148
FUTURE WORK.....149

REFERENCES.....152

APPENDICES
SOL-GEL SYNTHESIS USING A ROTARY EVAPORATOR.....165
SUBSTRATE PREPARATION & CLEANING PROCEDURES.....170
SPIN-CASTING OF POLYMERS AND SOLUTION-BASED OXIDE LAYERS.....173
ELECTRON BEAM EVAPORATION OF CATHODE MATERIALS.....175
COPYRIGHT PERMISSIONS / AUTHORIZATIONS.....177

VITA.....182

LIST OF TABLES

Table Page

1. Four different combinations of polymer: fullerene structures used in the tandem solar cell study.....97

2. Overview of material parameters used in the fit to the experimental data.....111

3. Mobilities of electrons and holes for Cases I, II, and III.....113

LIST OF FIGURES

Figure Page

1. U.S. renewable energy resource map by source type (August 2009).....1

2. U.S. Photovoltaic Solar Resource (October 2008).....2

3. Renewable energy sources directly or indirectly receive energy from the sun.....5

4. Standard solar spectra for space and terrestrial use.....8

5. Air mass values in space and through Earth's atmosphere.....9

6. Structures of commonly-used donor and acceptor polymers.....12

7. Schematic of bilayer device with separate donor and acceptor layers.....13

8. Schematic of bulk-heterojunction device with a combined donor/acceptor layer.....14

9. Schematic of series tandem inorganic/organic bulk heterojunction solar cell.....16

10. Verified Best Research-Cell Efficiencies (current September 2011).....17

11. Solar irradiance and absorption profiles for *Rhodobacter sphaeroides* (anoxygenic bacterium) and *Synechocystis* (oxygenic cyanobacterium).....21

12. Chlorophyll *a* and *b*, Bacteriochlorophyll *a*, B-Carotene, and Peridinin.....22

13. Photosynthetic antennas and reaction center involved in the transduction of light energy to stored energy.....23

14. P3HT monomer unit.....24

15. Segment of RR-P3HT polymer showing conjugated backbone.....25

16. PCPDTBT monomer unit.....25

17. PCPDTBT conjugated polymer segment showing alternating single and double bonds between carbon atoms.....26

18. Schematic of sp^2-hybridized carbon atom.....26

19. Overlap of non-hybridized p_z carbon atoms ((sp^2 orbitals are not shown).....27

20. Absorption spectra; P3HT HBG polymer, an LBG polymer, and the solar spectrum.....28

21. Exciton dissociation at the interface of the donor polymer, PCPDTBT, and acceptor $PC_{61}BM$.....33

22. Mobility as a function of carrier density for different T and E.....38

23. Effects of annealing on P3HT.....48

24. Coulomb radius and recombination.....50

25. Polymer-coating on fiber containing a single Bragg grating.....54

26. Graphical user interface for Fiber Bragg grating simulation tool.....55

27. Number of photons (N_{ph}) absorbed in the top and bottom subcell layers.....57

28. FF, series and parallel resistances, and schematic of a solar cell.....62

29. Basic charge transfer mechanism donor polymer to acceptor metal oxide.....64

30. Energy level diagram of TiO_x-incorporated hybrid OSC.....65

31. Conventional cell and a device incorporating an optical spacer.....66

32. Energy levels for a device with an optical spacer.....67

33. Simulated current densities for P3HT:$PC_{61}BM$ as a function of layer thickness.....73

34. J_{SC}, FF, η, and V_{OC} vs. active layer thickness for equal carrier mobilities.....74

35. J_{SC}, FF, η, and V_{OC} vs. active layer thickness with decreased hole mobility ($\mu_e = 10\mu_h = 10^{-3}$ cm^2 V^{-1} s^{-1}).....74

36. Efficiency as a function of active layer thickness for two electron/hole mobility combinations in P3HT:$PC_{61}BM$.....75

37. J_{SC} vs active layer for IQE = 100% (dotted lines) and P3HT:$PC_{61}BM$ and P3HT:$PC_{71}BM$ mobilities (solid lines) equal to $\mu_e = \mu_h = 10^{-3}$ cm^2 V^{-1} s^{-1}.....78

38. P3HT:$PC_{71}BM$ efficiency vs. active layer thickness for $\mu_e = \mu_h = 10^{-3}$ cm^2 V^{-1} s^{-1}, $\mu_e = 10\ \mu_h$, and $\mu_e = 100\ \mu_h$.....78

39. Simulated and experimental absorption data for PCPDTBT:PC_{71}BM and PCPDTBT:PC_{61}BM.....85

40. Current density as a function of active layer thickness for three combinations of electron/hole mobilities in PCPDTBT:PC_{71}BM and PCPDTBT:PC_{61}BM.....86

41. Electrical characteristics for PCPDTBT:PC_{71}BM simulations.....88

42. V_{OC} vs. hole mobility in PCPDTBT:PC_{71}BM simulations based on two electron mobilities.....89

43. Efficiency as functions of photoactive layer thickness and electron/hole mobility ratios for PCPDTBT:PC_{71}BM and PCPDTBT:PC_{61}BM.....90

44. Schematic of the organic tandem structure used in the simulations.....95

45. Isoline graph of photocurrent density (J_{ph}) plotted as a function of active layer thickness for both the top P3HT:PC_{71}BM (d_{top}) and bottom PCPDTBT:PC_{61}BM (d_{bottom}) cells.....98

46. Photocurrent densities, Tandems I and II–J_{ph} vs. bottom subcell thickness, and Tandems I and II–J_{ph} vs. top subcell thickness.....100

47. Comparison of J_{ph} and J_{SC} for Tandems I and II as a function of subcell thicknesses.....103

48. Tandems I and II device power conversion efficiencies as a function of top cell thickness.....104

49. Simulated values for J_{SC}, FF, η, and V_{OC} for Tandem II as functions of the thickness of the top subcell.....105

50. J–V curves for Tandem II structure for different active layer thicknesses.....106

51. Schematic diagram of tandem P3HT:PCBM / PCPDTBT:PCBM structures.....110

52. Comparison of current density and efficiencies between experimental and simulation data of P3HT:PCBM and PCPDTBT:PCBM devices.....112

53. Isolines matching current densities between a PCPDTBT:PC_{61}BM bottom cell and a P3HT:PC_{71}BM top cell for different Cases I, II, and III.....114

54. Variation in isolines with different carrier mobilities for Cases I and III.....116

55. Current density, *FF*, V_{OC}, and efficiency for Cases I, II, and III as a function P3HT:PC_{71}BM thickness.....118

56. IV characteristics of each subcell in the tandem structures for Cases I and III with different active layer thicknesses.....120

57. Fabrication parameters impacting device efficiency.....122

58. Tandem solar cell energy level diagram for PCPDTBT:PC_{61}BM and P3HT:PC_{71}BM subcells.....127

59. UV-Vis spectra of PC_{61}BM and PC_{71}BM before and after thermal annealing.....130

60. Surface morphologies of PC_{61}BM and PC_{71}BM before and after thermal annealing.....133

61. Photoluminescence spectra from P3HT, P3HT:PC_{61}BM, and P3HT:PC_{71}BM.....134

62. IV characteristics of the OSCs measured at 100 mW cm^2.....136

63. Schematic of P3HT:PC_{71}BM planar cell with TiOx optical spacer.....138

64. IV curve for a P3HT:PC^{71}BM solar cell with TiOx layer.....138

65. IV curve for PCPDTBT:PC_{61}BM cell with TiOx layer.....140

66. IV Curve: PCPDTBT: PC_{61}BM (bottom) and P3HT:PC_{71}BM (top) Tandem solar cell.....144

67. P3HT:PC_{71}BM thin film after annealing for 10 minutes at 80°C.....145

68. PCPDTBT:PC_{71}BM thin film after annealing for 10 minutes at 80°C.....145

69. PCPDTBT:PC_{61}BM thin film after annealing for 10 minutes at 80°C.....146

70. Varied coloration of thin film donor:acceptor blends.....147

71. SEM micrograph revealing infiltration of photoactive organic blends of P3HT:PCBM into 1.0 μm (diameter) pores of an Si template.....150

72. IKA Rotary Evaporator setup.....166

73. Rotary flask lowered into silicone oil bath.....167

74. Mixture appears pink after 1 hour at 80°C.....168

75. Mixture appears dark red after 1 hour at 120°C.....168

76. Sol-gel-produced TiOx material ready for dilution and spin-casting.....169

77. Scored 1" x 3" ITO/glass slide.....170

78. 1" x 1" substrate with backside marked.....170

79. Nine-sample substrate holder and schematic of individual mask.....175

CHAPTER I
INTRODUCTION

MOTIVATION AND SCOPE OF RESEARCH

Renewable energy sources are recognized worldwide as being scientifically, politically, and economically critical to furthering economic development, spurring job creation, enhancing national security, and ensuring a cleaner environment. In the United States, the entire spectrum of renewable resources from biomass – to geothermal – to solar – to wind, is being explored simultaneously in efforts to develop these technologies and reduce dependence on fossil fuels. As seen in Figure 1, nearly every location in the

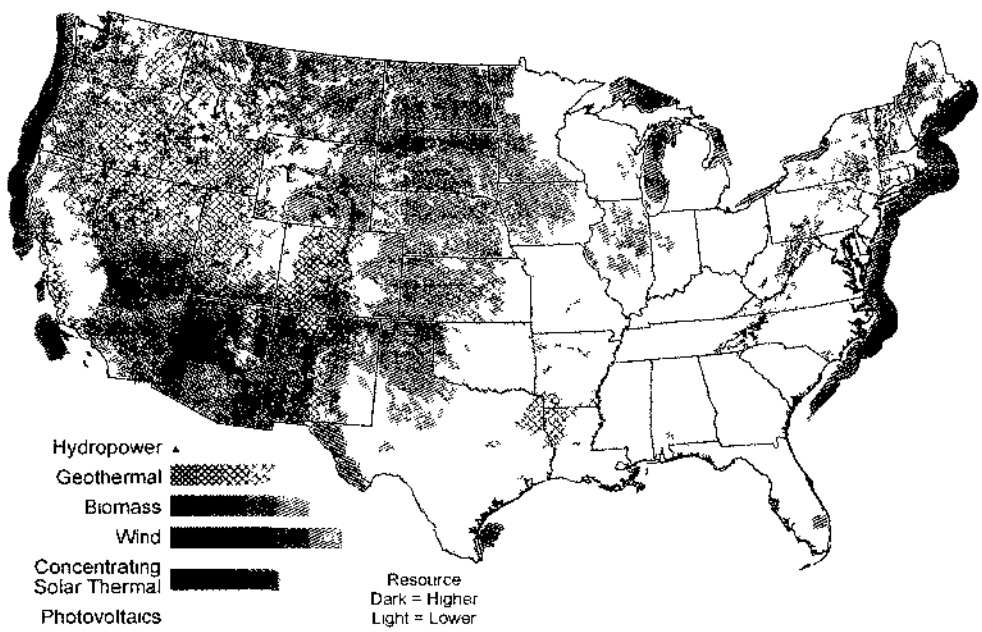

Figure 1. U.S. renewable energy resource map by source type (August 2009) [1].

continental United States can take advantage of the energy available from renewable sources. While most technologies are particularly suited to specific geographic regions, solar is readily available all across the country. In Figure 2, the photovoltaic solar resource map for the entire U.S. including Alaska and Hawaii shows that insolation – the amount of solar radiation received over a given area per unit time – is sufficient to make photovoltaic research and development a worthwhile endeavor.

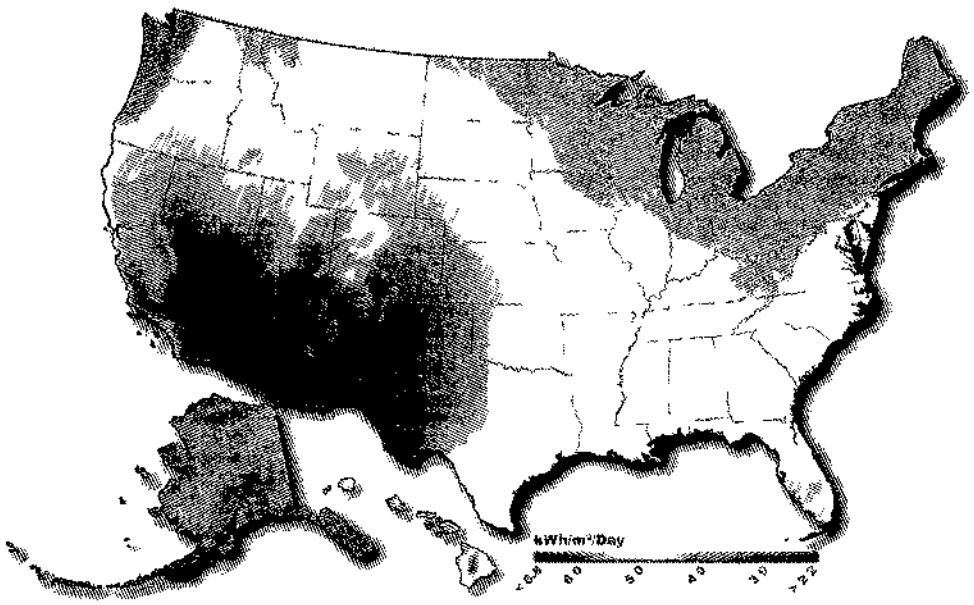

Figure 2. U.S. Photovoltaic Solar Resource (October 2008) [1].

This is especially relevant and important in light of the fact that in 2010, the U.S. was ranked second globally in total energy use at 19%; China was first at 20.3%. The demand for energy from all sources (i.e., oil, natural gas, coal, nuclear, hydroelectricity, and renewables) is increasing in both developed and developing nations as consumption growth reached 5.6% last year [2]. As a result, competition for resources will increase in

the coming decades as nations like China and India undergo their own "Industrial Revolutions."

One of the areas of scientific research focused on developing this alternative renewable source is a relatively new concentration in solar energy exploration; organic photovoltaics (OPV). OPV technologies differ from their conventional *inorganic* counterparts, which are based primarily on such materials as silicon (Si) and germanium (Ge), in that semi-conducting organic polymer materials are used as the "light-to-electricity" conversion media. Unfortunately, current state-of-the-art devices experience poor photon-to-photocurrent efficiency, mainly due to *inferior charge transport* and *high carrier recombination* that are a result of poor electrical characteristics in disordered polymer-fullerene networks. Current research and development efforts remain focused on fabrication methods that the larger scientific community agrees require advanced technologies to overcome the problems that limit increases in efficiency [3,4]. Other methods of device improvement will need to be incorporated, such as invention of new semi-conducting polymers and exploitation of novel device structures that overcome the current limits of the physics as they are understood today.

This dissertation describes computer simulation of two low- and high-bandgap organic polymers incorporated in tandem planar solar cell devices. Inorganic metal oxide layers are included in the structures to assess their impact on energy conversion efficiency. Sequential ordering of the subcells of these *tandem* structures is also examined. The goal of this work is to develop a means for designing controlled device platforms via accurate computer modeling and innovative nanofabrication technologies that advance photon-to-photocurrent efficiency in hybrid inorganic-organic solar cells.

RENEWABLE ENERGY SOURCES

The moniker "renewable" refers to energy sources that occur naturally, are continually replenished, and are essentially of indefinitely limitless quantity. In contrast, oil, coal, and natural gas – the primary energy sources currently used in the United States – are believed to be in finite supply and have a number of negative attributes associated with them including their expense and potential for causing adverse environmental impact. With these concerns in mind, the U.S. and other industrialized countries around the world seek to exploit the benefits of renewable energy. There are seven primary types currently being explored and/or utilized to varying degrees:

1. *Geothermal*; energy generated within the core of the Earth that radiates to the surface through a thermal gradient. This is a clean and sustainable heat retained in shallow ground, hot water, rocks, and in magma [5].
2. *Ocean Energy*; includes the phenomena of sunlight, wave power, and tidal energy. Oceans are the Earth's greatest collectors of solar energy; thermal energy from the sun and mechanical energy from waves and tides can be combined to produce electricity [6].
3. *Wind*; energy in wind is collected via various technologies and converted from its mechanical form to electricity. The most common wind transducer is some form of turbine device connected to an electrical distribution grid that supplies power to end-users [7].
4. *Biomass*; a class of renewable energy that includes organic matter (e.g., plants, agricultural/forest residues, organic waste, etc.) to produce electric and chemical (biofuel) power. The energy contained in biomass originates from the sun [8].

5. *Hydroelectric*; energy generated from the mechanical force of water falling through a height (under gravitational force) or flowing though a suitable transducer to produce electricity. Also referred to as *hydropower* [9].
6. *Hydrogen / Fuel Cells*; an energy source contained in many materials including water, organic compounds, and some bacteria and algae. Hydrogen is a high-energy source that produces virtually no pollution upon combustion. Also, the sun can be used to produce storable hydrogen for later use in fuel cells [10,11].
7. *Solar*; the *primary* renewable energy source. As can be seen in Figure 3, virtually all other renewable sources (with the exception of geothermal) get their energy directly or indirectly from the sun [12].

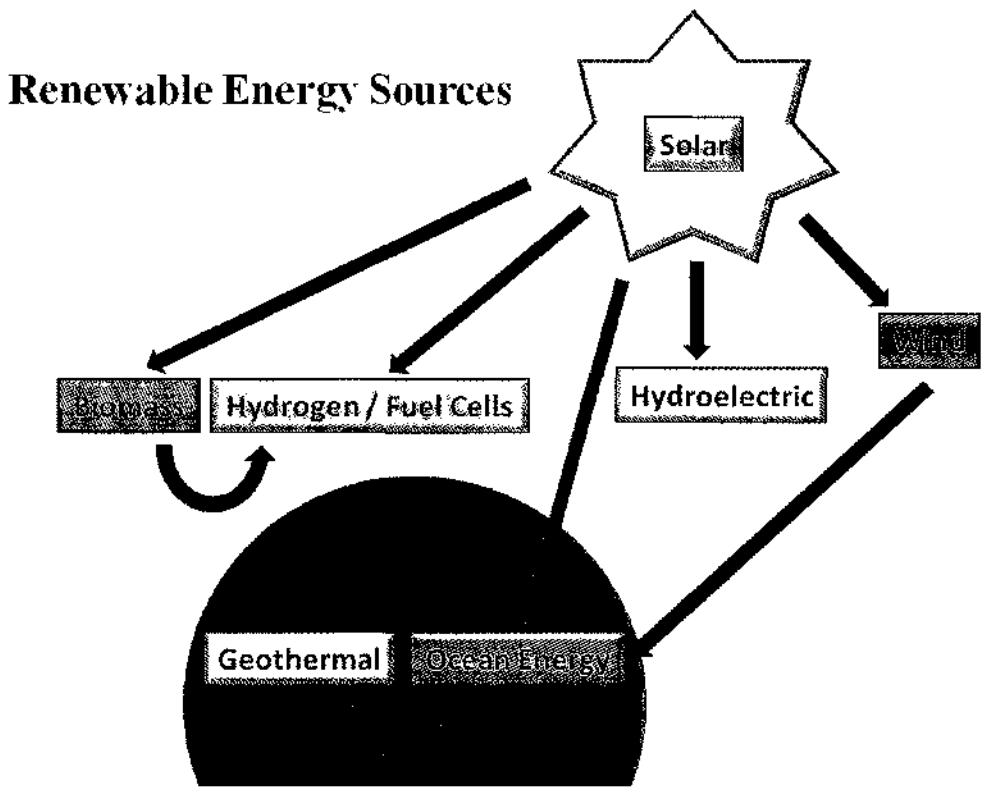

Figure 3. Renewable energy sources directly or indirectly receive energy from the sun.

Solar energy comes in two basic forms; heat and light. These are employed to provide numerous useful technologies including [13]:

a) Photovoltaic Systems (electricity *directly* from sunlight)

b) Solar Hot Water

c) Solar Electricity (electricity from the sun's *heat*)

d) Passive Solar Heating/Lighting

e) Solar Process Space Heating/Cooling

Since the genesis of most types of renewable energy is the sun itself, the exploration and understanding of the properties, characteristics, and capabilities of solar energy are critical. Much effort continues to go into improving our understanding of solar energy and increasing its application on a widespread basis in hopes that it will decrease dependency on non-renewables.

SOLAR AS THE PRIMARY RENEWABLE SOURCE

Not being a priority solely unique to the scientific realm, the topic of renewable energy is omnipresent in virtually every other area of modern life from politics – to the economy – to education – to entertainment. One has only to look at packaging in retail stores, or view television commercials, or hear politicians and members of the music and movie industries to realize that the subject is being taken seriously worldwide. In fact, many high schools these days are requiring students to take at least one "green" course as part of their curriculum for graduation, politicians are pressed to state their positions on matters such as "anthropogenic global warming" (AGW) and sustainable energy programs, and entertainment personalities actively promote a myriad of environmental causes. While the sociological, political, and economic facets of renewable energy often

tend to be contentious and subject to debate, one fact remains true; virtually all other forms of renewable energy derive from the sun and solar technology continues to improve. More importantly, in comparison with most non-solar renewables, it is clear that solar has the greatest theoretical (i.e., available) and technical (i.e., useable) potential [14]. Eventually, currently achievable efficiency limitations and the cost-prohibitive nature of manufacturing will be negated. A recent indication of this reality is the fact that over 100 countries added photovoltaic (PV) capacity to their power production infrastructures during 2010 as solar photovoltaics continue to be the world's fastest-growing power generation technology [15]. It is with this in mind that the focus of this dissertation is on an application of the *primary* renewable energy – solar – and its use in hybrid inorganic-organic solar cells.

The conversion of sunlight – in the form of photons – to electricity is called the photovoltaic (PV) effect. While French physicist Edmond Becquerel first discovered the PV effect as far back as 1839 [16], more than one hundred years elapsed before the physics behind the phenomenon could be explained. This transduction from one energy form to another takes place through the use of semi-conducting materials such as doped crystalline silicon and germanium. Other inorganic elements can also be used, as well as some *organic* (i.e., carbon-containing) materials as will be discussed later. Basically, photons strike a semi-conducting absorbing media and dislodge electrons that are then available for conduction, thereby producing electricity. The primary determinant of the quality of this energy conversion process is *efficiency*; in other words, how much power is produced for a given number of photons striking the device? When silicon-based solar

cells were first made in the 1950s, efficiencies were less than 4% [17]. Today, however, commercially-produced cells have efficiencies in excess of 15%.

Numerous factors impact efficiency and one of the most important is spectral absorption of the device – a parameter describing the fraction of incident radiation absorbed by the solar cell over a range of light frequencies (wavelengths). Spectral absorption is primarily determined by the absorbing material itself (i.e., the ability of the semi-conducting media to absorb photons), but is also impacted by several physical considerations including wavelength of the incident light, reflection from the surface of the device, and atmospheric conditions. Spectral absorption is essentially a *dynamic* factor since the Earth's rotation in relation to the Sun is continually changing insolation at every location on the planet. Figure 4 shows spectral irradiance from the sun in units of W m^{-2} nm^{-1} as a function of wavelength.

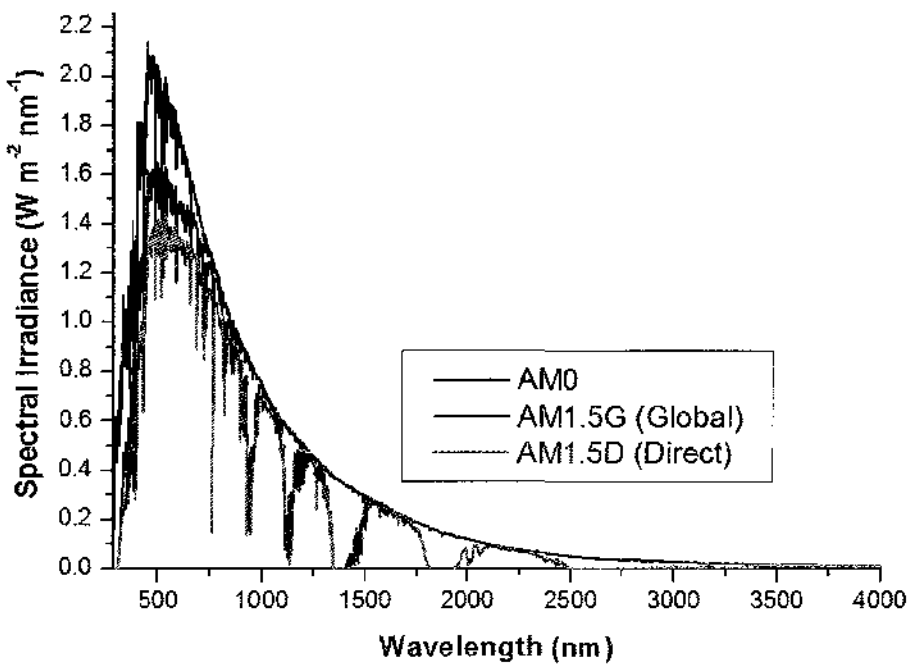

Figure 4. Standard solar spectra for space and terrestrial use [18].

Standard reference spectra are defined to allow for accurate performance comparison of photovoltaic devices from different manufacturers and research laboratories [19]. The inset in the figure indicates the *air mass* (AM) standards that have been established by the American Society for Testing and Materials (ASTM) to account for changes in each spectrum resulting from light transmission through space and Earth's atmosphere. AM is the *amount* of atmosphere light passes through from the Sun to the surface of the Earth [20]. As seen in Figure 5, AM 0 indicates that light travels solely through the void of space to the outermost perimeter of Earth's atmosphere. In contrast, AM 1.0 represents the amount of atmosphere light traverses from the edge of space to the Earth's surface at the equator; this is the shortest possible travel distance from the space/atmosphere junction to the surface. In order for sunlight to reach higher latitudes, it must travel greater distances. AM 1.5 represents the amount of atmosphere light passes through to reach locations in the United States and Europe. Two standards for AM 1.5 exist; AM 1.5G ("global") and AM 1.5D ("direct"). The difference between the two lies in the way

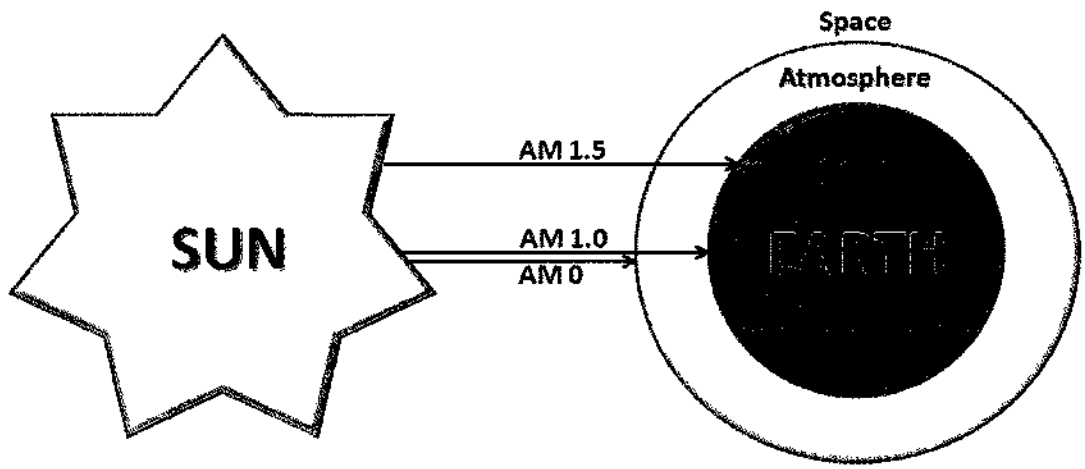

Figure 5. Air mass values in space and through Earth's atmosphere.

the spectra are obtained, however AM 1.5G is most often used in research for practical reasons.

Even with such efficiency-diminishing factors as atmospheric spectral absorption and scattering, far more light energy is generated by the Sun and transmitted to Earth than could ever be used by humans. It therefore follows that the arguably finite amount of non-renewable energy sources makes technological development and implementation of photovoltaics on a worldwide basis critical to the continual improvement and sustainment of life. As well, other renewable forms of energy – most having the Sun as their source – are either too inefficient or of inadequate quantity to be of practical use. Essentially, even a cursory cost/benefit analysis shows they are too expensive for the amount of power they produce. To date, silicon-based PV cells are the most ubiquitous, well-understood, and commercially-viable technology that is based on renewable energy. Still, their cost per unit power (e.g., dollars/Watt) is still too high to allow for widespread implementation nationwide. A potential alternative that has been gaining much interest over the past few decades is organic photovoltaics. These come in the form of carbon-based semi-conducting polymer materials that demonstrate a photovoltaic effect when illuminated with sunlight. The primary appeal of this novel approach is the potential for realizing inexpensive PV devices that are easily produced and offer wider application using a myriad of substrates.

ORGANIC BULK HETEROJUNCTION SOLAR CELLS

Even with silicon solar cells dominating the photovoltaic market with an 85% share, alternative PV technologies are being explored that will more effectively take advantage of the Sun's endless supply of energy [21]. As previously mentioned, a very

active area of research over the past three decades involves the use of semi-conducting polymer materials that perform as light absorbers or generators in solar cell and light-emitting diode (LED) devices. The first indication that organic solar cells could possibly become a reality occurred in 1954 when organic compounds were doped with halogens and found to demonstrate dark conductivity [22]. However, it wasn't until the late 1970s when Shirakawa, Heeger, and MacDiarmid successfully used halogens to dope the polymer polyacetylene ($[C_2H_2]_n$) and demonstrate its conductivity. It was this achievement that earned them the 2000 Nobel Prize in Chemistry [23].

Since the remarkable discovery that carbon-based polymers could conduct electricity, a non-stop flurry of exploration into the possibilities and capabilities of organic electronics has continued to this day. In the most basic sense, an electron-donating polymer is paired with an electron-accepting polymer in such a way that charge transfer from the former to the latter is energetically favorable. While many types and combinations of donor-, and acceptor-polymers have been studied, a relative few have risen to the forefront of technological viability. The most extensively studied donor to date is the high-bandgap, regioregular (RR), poly-3 hexylthiophene (P3HT) conjugated polymer. Regioregularity refers to the alternating single and double bonds between the carbon atoms in the polymer backbone. It is this structural arrangement that allows electron delocalization and gives rise to electrical conductivity. Also, some low-bandgap polymers are being examined based on their absorption characteristics and responsiveness to different portions of the solar spectrum. The most common electron-accepting polymers in use today are [6,6]-phenyl (C_{61} or C_{71})-butyric acid methyl ester ($PC_{61}BM$ and $PC_{71}BM$). These are essentially fullerenes with added functional groups

that make them capable of being dissolved more effectively in a variety of organic solvents (e.g., chlorobenzene, dichlorobenzene, chloroform, etc.). Figure 6 shows schematic representations of the molecular structures of P3HT, $PC_{61}BM$, $PC_{71}BM$, and the low-bandgap polymer, PCPDTBT.

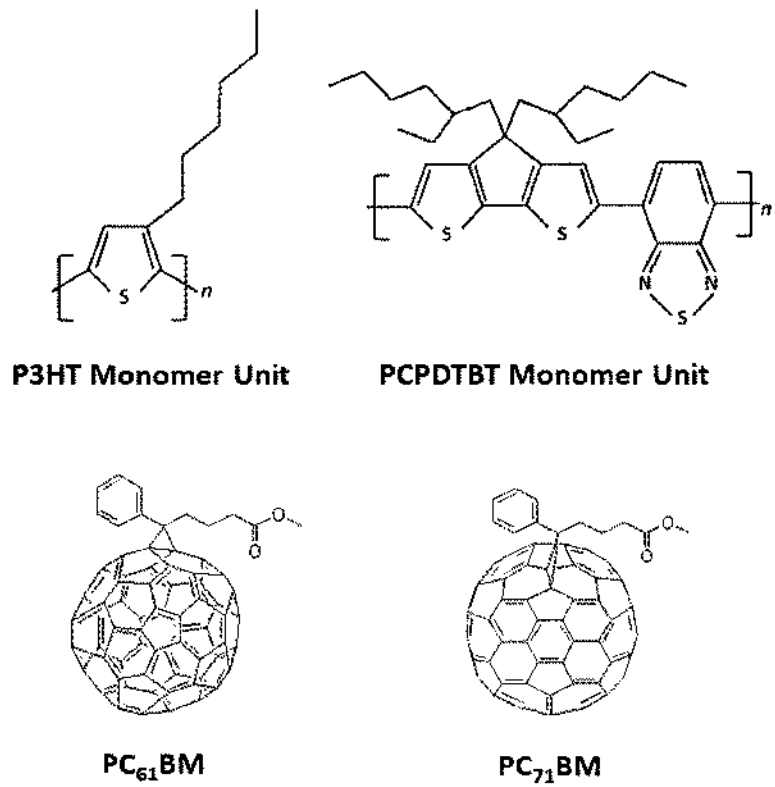

Figure 6. Structures of commonly-used donor and acceptor polymers [24, 25].

What is critical – besides the *electrical properties* of the semi-conducting materials – is the manner in which the two physically interface with each other. Many physical configurations and spatial orientations have been assessed over the years to determine which will yield the highest device efficiencies. One of the original schemes featured a bilayer device like the one shown in Figure 7. A bilayer heterojunction device

contains separate donor and acceptor layers that interface over a large two-dimensional area (i.e., relative to layer thickness) and together form the "active layer" capable of producing a PV effect. The overall structure is essentially one where several thin-film layers are

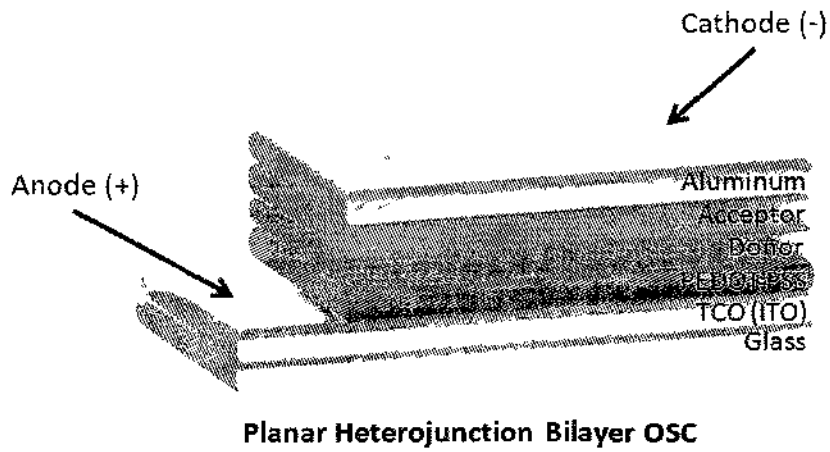

Figure 7. Schematic of bilayer device with separate donor and acceptor layers.

stacked on top of each other on a clear glass substrate. The first layer is a transparent conducting oxide (TCO) that serves as the hole-collecting anode. Indium tin oxide (ITO) is the most commonly used TCO due to its transparency and low sheet resistivity ranging from about 4 – 8 ohm/square. It is highly conductive, but suffers from a variable work function (ϕ) depending on how it has been processed [26]. To account for this, a layer of poly(ethylenedioxythiophene):poly(styrene sulfonate) (PEDOT:PSS) is placed on top of the ITO. PEDOT:PSS serves as a hole-transporter/electron-blocker layer between the ITO and the donor layer. After an electron-donating material is placed over the PEDOT:PSS, it is subsequently overlaid by the electron-acceptor. Finally, an aluminum cathode is deposited on the backside of the device to conduct the negative charge carriers

out of the device and produce useable power. The PV effect is produced by light that traverses the entire structure from the glass side all the way through to the backside aluminum cathode.

Unfortunately, the bilayer configuration suffers from poor exciton dissociation. Excitons are electrostatically-bound hole-electron charge pairs. Dissociation of excitons into separate hole and electron charge carriers must take place at the donor/acceptor interface. In a bilayer arrangement, this interface is limited in size when considering the volume of the donor and acceptor materials in their respective layers. In an effort to increase the donor/acceptor interface, a new technique was introduced where the polymer materials were mixed together in a suitable solvent and deposited on the substrate as a single *bulk-heterojunction* (BHJ) layer. This has the effect of dramatically increasing overall interfacial area between the donor and acceptor polymers. This in turn leads to much greater exciton dissociation. Figure 7 shows a schematic of the modified solar cell device.

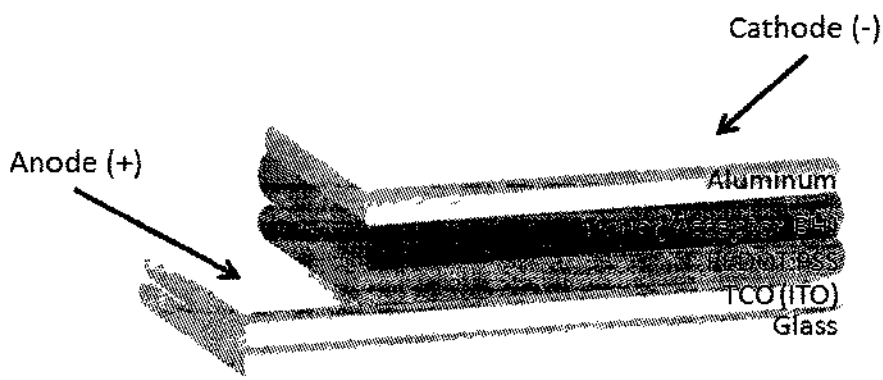

Bulk Heterojunction (BHJ) OSC

Figure 8. Schematic of bulk-heterojunction device with a combined donor/acceptor layer.

Power conversion efficiencies (PCE) are markedly increased in BHJ devices compared to their bilayer counterparts. Still, improvements can be made as the evolution from planar bilayer and BHJ cells has led to the introduction of hybridized "tandem" PV devices.

HYBRID INORGANIC/ORGANIC DEVICES

With power conversion efficiencies for conventional BHJ planar organic solar cells that use the best available donor and acceptor polymers appearing to plateau around 8%, exploration of new organic materials and device structures is accelerating. One focus is on the incorporation of transition metal oxides to create novel hybrid inorganic/organic solar cell architectures and push PCE beyond current limits. Already, the metal oxide ITO is commonly used as one of the solar cell electrodes. However, other oxide materials have properties that make them suitable for use at other locations within the device. Two materials getting a great deal of attention are titanium oxide (TiO_x) and zinc oxide (ZnO). These serve various functions such as electron transporters, optical spacers, and as structural supports between subcells in tandem devices. Other metal oxides can be used as hole transporters (e.g., V_2O_5, MoO_3, NiO, and WO_3, etc.) [27,28,29,30].

From the standpoint of structural changes, efforts are currently underway to create composite solar cells composed of subcells interconnected either in parallel or series [31]. Each configuration has its pros and cons in addition to unique fabrication considerations. A tandem solar cell composed of subcells connected in *parallel* will generate a total open circuit voltage (V_{OC}) equal to that of the subcell with the *smallest* individual open circuit voltage. The short circuit current density (J_{SC}) is the *sum* of the currents produced by

each subcell. The following expressions describe the relationships in a tandem solar cell with subcells connected in parallel:

$$V_{OC(\text{parallel})} = \min\,[V_{OC(\text{subcell 1})}, V_{OC(\text{subcell 2})}, \ldots, V_{OC(\text{subcell } n)}] \quad (1)$$

$$J_{SC(\text{parallel})} = J_{SC(\text{subcell 1})} + J_{SC(\text{subcell 2})} + \ldots + J_{SC(\text{subcell } n)} \quad (2)$$

In contrast, tandem solar cells with subcells connected *in series* have different voltage and current characteristics. The total V_{OC} for the overall structure is the *sum* of the individual subcell voltages while the current density is limited to that observed in the subcell with the *smallest* current:

$$V_{OC(\text{series})} = V_{OC(\text{subcell 1})} + V_{OC(\text{subcell 2})} + \ldots + V_{OC(\text{subcell } n)} \quad (3)$$

$$J_{SC(\text{series})} = \min\,[J_{SC\,(\text{subcell 1})}, J_{SC\,(\text{subcell 2})}, \ldots, J_{SC\,(\text{subcell } n)}] \quad (4)$$

A schematic representation of a tandem hybrid inorganic/organic series solar cell can be seen in Figure 9.

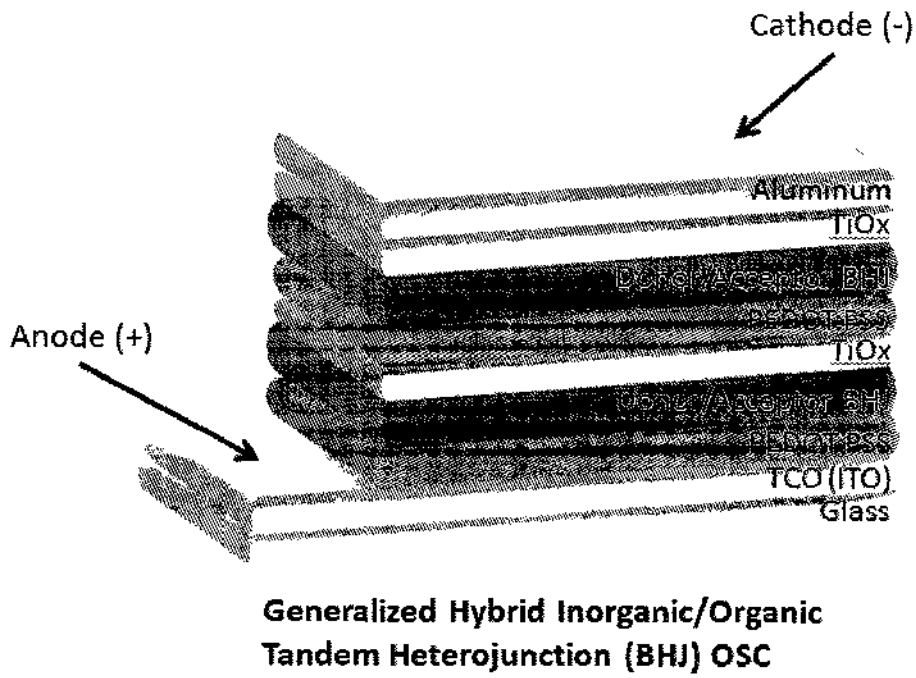

Figure 9. Schematic of series tandem inorganic/organic bulk heterojunction solar cell.

In this scenario, one TiO_x layer is placed in the middle of the tandem structure to serve as an electron transporter/hole blocker between the top and bottom subcells. It also serves as a structural support for the top subcell. The TiO_x layer in the top subcell immediately beneath the aluminum cathode serves as an electron transporter and also as an optical spacer. As in single planar organic cells, the PEDOT:PSS layers function as hole transporters and provide a smoother energy level transition between the ITO anode and the BHJ active layer. The BHJ donor/acceptor layers – the "active layers" where the PV effect is produced – are comprised of high- and low-bandgap conjugated polymer and fullerene materials. With the exception of the aluminum cathode, all layers can be applied via solution processing. It is the structure in Figure 9 upon which the computer simulations described in this dissertation are based.

PV research continues at a tremendous pace as can be seen in Figure 10.

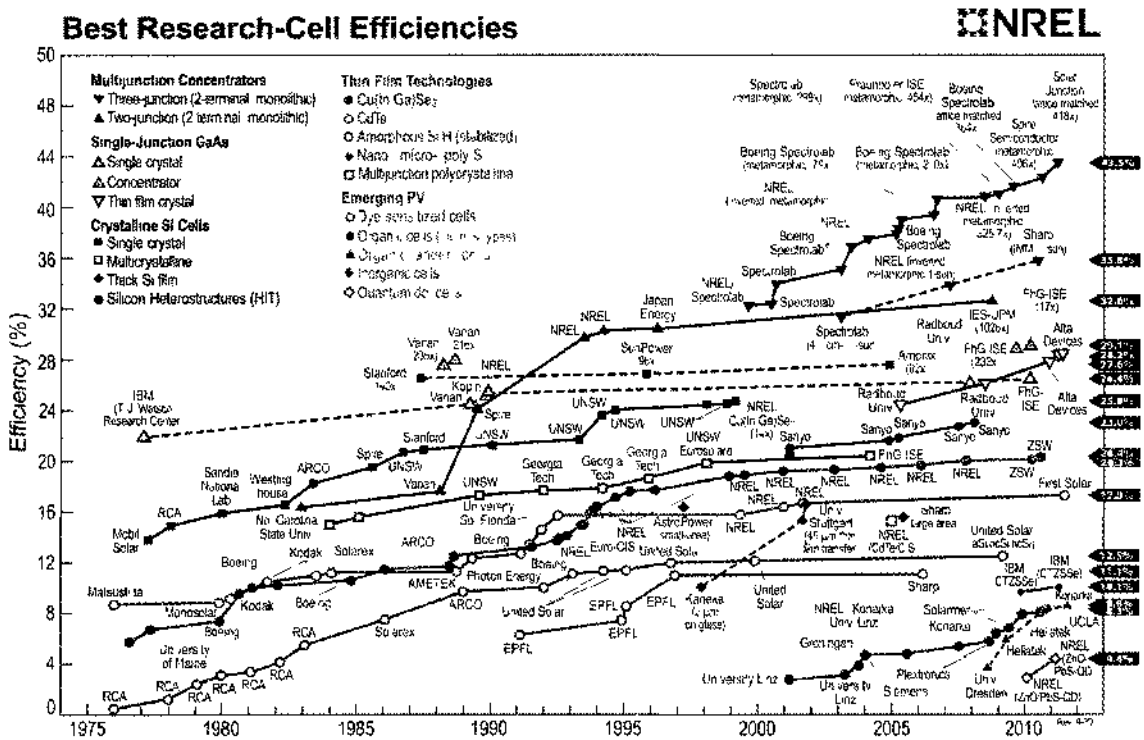

Figure 10. Verified best research-cell efficiencies (current September 2011) [32].

While the best research cell efficiencies to date are achieved using inorganic materials, the study of organics and hybrid inorganic/organic devices is well worth the time, effort, and expense. The highest efficiencies achieved thus far are with double and triple multi-junction concentrator configurations – primarily made from silicon (Si), germanium (Ge), and gallium arsenide (GaAs) absorbers. However, these are extremely expensive and unlikely to be commercially viable. Crystalline Si (single and multi-crystalline) continues to be a mainstay in the PV market worldwide, but improvement in PCE has been essentially static. Well-established thin-film technologies (e.g., CdTe, $Cu(InGa)Se_2$, multi-junction poly-crystalline, etc.) continue to garner widespread interest, but their improvement has also been relatively flat – and at significant financial cost. A final category loosely referred to as "emerging technologies" includes dye-sensitized cells, various organic cells, *organic tandem cells*, novel inorganics (e.g., CTZSSe), and quantum dot (QD)-based devices. It is in this class where remarkable improvements in PCE can be found over a very short period of time – particularly with organic tandem cells. In fact, efficiency in these devices has increased more than 100% (from 4% to ~8^+%) in just the past three years [32].

RELATED WORK

With the promise demonstrated so recently in rapidly increasing PCE in organic tandem solar cells and realizing the potentially significant impact this could have both technologically and economically, researchers around the globe are working to make even greater improvements in these novel solar cell architectures. Kim, et al., fabricated series tandem hybrid inorganic/organic solar cells using all-solution processing and achieved power conversion efficiencies exceeding 6% [33]. Their work involved

connecting two subcells – one made from low-bandgap polymer mixed with $PC_{61}BM$ and the other from high-bandgap polymer combined with $PC_{71}BM$ – on either side of a TiO_x spacer. From an optical modeling perspective, Andersson, Persson, and Inganas used computer simulations to compare current and PCE in one folded, and four stacked tandem solar cells [34]. They used finite element and transfer matrix methods on the folded and stacked cells, respectively. They found that for serially-connected subcells, these techniques were suitable for comparing all five configurations. Dennler, et al., also carried out a series of optical simulations on series tandem cells [35]. It was their work that was the starting point for the simulations conducted in our lab and described in this dissertation. Their work showed that Kim's tandem solar cell [33] ensured that absorption is balanced in the top and bottom subcells. Study is also being conducted on parallel tandem organic cells. Guo, et al., created their parallel device using P3HT:$PC_{61}BM$ and PCPDTBT:$PC_{61}BM$ subcells separated by a semi-transparent metal layer that was combined with inorganic semiconductors [36]. They found the short circuit current to be the sum of the currents from each of the subcells (as predicted by Equation (2)), while the V_{OC} was "similar to the subcells". Developing an alternative technique, Sun, et al., used a MoO_3/Ag/Al/Ca intermediate layer between two P3HT:$PC_{61}BM$ BHJ active layers to create an *inverted* series tandem organic solar cell [37]. The maximum PCE achieved was 2.78% under simulated 100 mW cm-2 (AM 1.5G) illumination and the FF was 61.8%.

ORGANIZATION

This dissertation is divided into five chapters. Chapter II details the theory behind solar energy conversion in organic polymers and addresses such issues as carrier

mobility, types and causes of carrier recombination, and the mathematical techniques needed to describe these phenomena. In Chapter III, the results from several computer simulations are discussed with a focus on such critical factors as optimization of active layer thickness, charge carrier mobility, use of low- and/or high-bandgap donor polymers, selection of electron-accepting fullerene materials, and spatial ordering of subcells in a tandem configuration. Chapter IV gives a detailed explanation of the key issues involved in actual device fabrication and characterization. Numerous fabrication considerations must be taken into account including type/amount of polymer, fullerene, and solvent used, annealing times and temperatures, and device layer thicknesses to name just a few. To characterize the performance of the photovoltaics produced, current-voltage (I-V), absorption (UV-VIS), surface morphology (Atomic Force Microscopy (AFM)), and refractive index (spectrometric ellipsometry (SE)) data were collected and are described. Finally, conclusions and recommendations for future research are presented in Chapter V.

CHAPTER II

THEORY

SOLAR ENERGY CONVERSION IN ORGANIC POLYMERS

Conversion of solar energy to other forms of energy by organic matter is not something novel or unique to the field of synthetic polymer photovoltaics. It's been occurring continually for millions of years in the biological world in the form of *photosynthesis*. Photosynthesis is a natural process where light is absorbed by organic organisms (e.g., plants, algae, cyano-, and anoxygenic bacteria, etc.) and stored in the form of biochemical energy. This energy is subsequently used to power cellular functions.

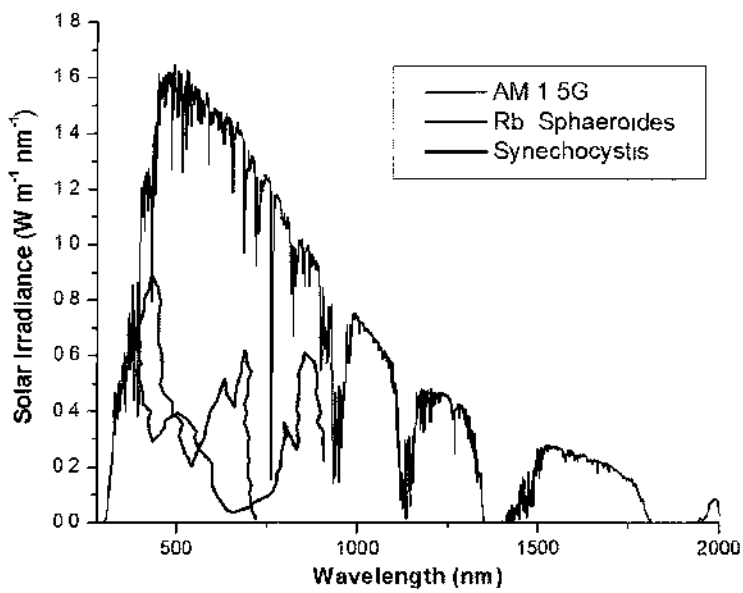

Figure 11. Solar irradiance and absorption profiles for *Rhodobacter sphaeroides* (anoxygenic bacterium) (red line) and *Synechocystis* (oxygenic cyanobacterium) (blue line) [38].

Most organisms capable of undergoing photosynthesis are sensitive to sunlight in the visible range (400 – 700 nm) while some others are reactive in the near infrared (nIR) range (700 – 1000 nm) [38]. Figure 11 shows a comparison between solar irradiance at the Earth's surface and absorption profiles of two representative photosynthetic organisms. It is clear that photosynthesis is a process primarily driven by the visible portion of the electromagnetic spectrum.

Plants, for example, have photo-receptive pigments called chlorophyll (there are several types) that absorb solar light and begin the process of photosynthesis. Several of these structures are shown in Figure 12.

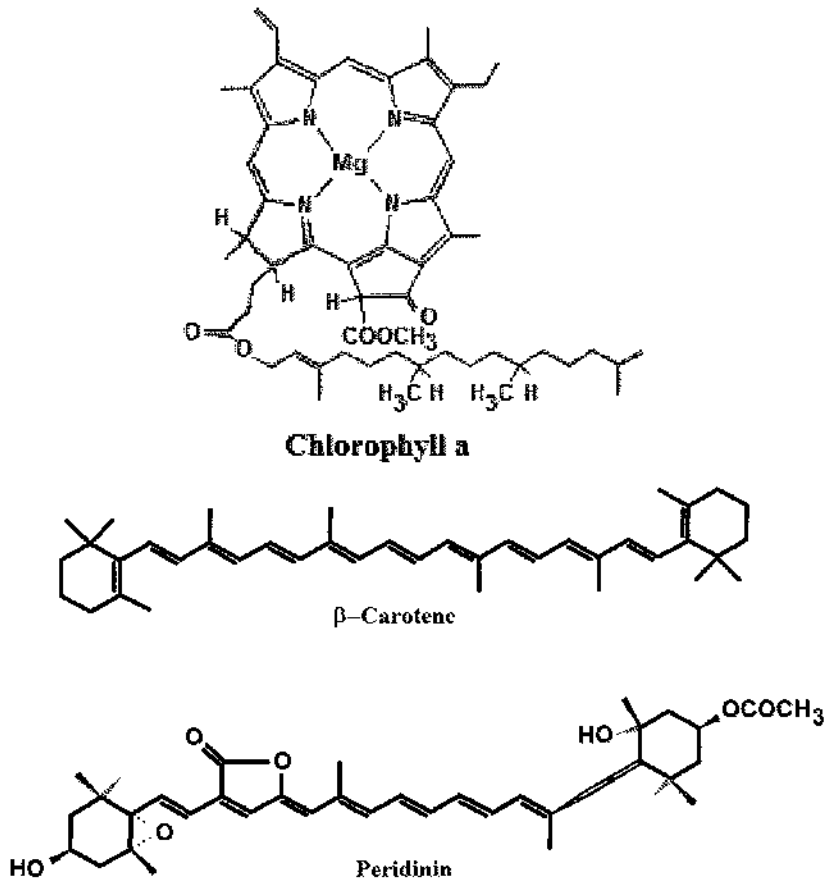

Figure 12. Chlorophyll *a*, β-Carotene, and Peridinin [38].

In the simplest description, light impinges on the plants' *antennae* where the chlorophyll pigments are located. Next, the absorbed energy results in electrons achieving an "excited" state. This additional energy is delivered to a *reaction center* where electron transfer takes place and the energy is stored. Antenna sites contain several types of chlorophyll as well as auxiliary structures such as β-Carotene and Peridinin. Of particular interest is the structure of these linearly-shaped molecules. Note the alternating single and double bonds between carbon atoms along the backbone of these pigments (Figure 12). This configuration is referred to as *conjugation* and is critical to the photovoltaic properties of synthetic polymers. A schematic representation of the natural biological process is seen in Figure 13.

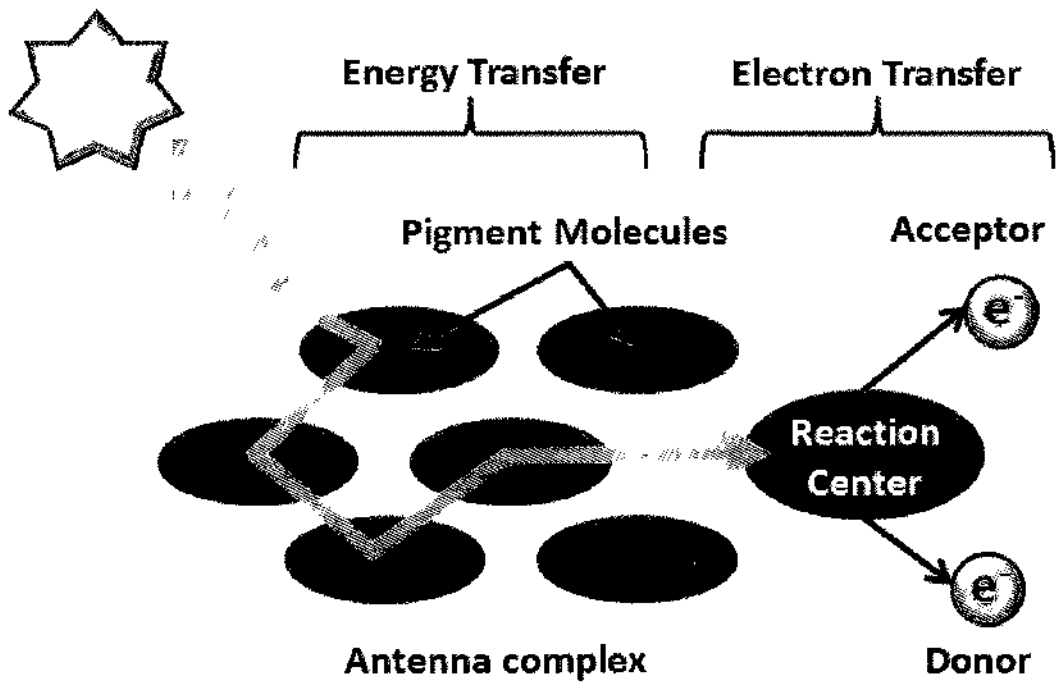

Figure 13. Photosynthetic antennas and reaction center involved in the transduction of light energy to stored energy [38].

In an analogous manner, synthetic polymers can absorb sunlight, causing electrons to be stimulated to a higher energy level, thereby forming *excitons*. These are coulombically-bound electron-hole pairs. The excitons then translate to a reaction center, which, in the case of BHJ active layer materials, is the interface between the donor and acceptor polymers. The excitons then dissociate into separate electron and hole charge carriers. The charge carriers are not stored, but instead flow to their respective electrodes and are available in the form of electricity external to the device.

Conjugated synthetic polymers like P3HT and PCPDTBT are comprised of backbones made of alternating single and double bonds between the carbon atoms. The monomer unit of P3HT is shown in Figure 14. The cyclopentathiophene (sulphur-containing) ring has an attached six-carbon (hexyl) functional group connected to carbon 3.

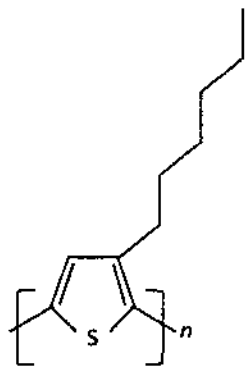

Figure 14. P3HT monomer unit.

When connected in series, the monomers form the regio-regular (RR) polymer *poly (3-hexylthiophene)* seen in Figure 15. Regio-regularity refers to the hexyl functional group being attached to the same carbon (number 3) in each monomer unit.

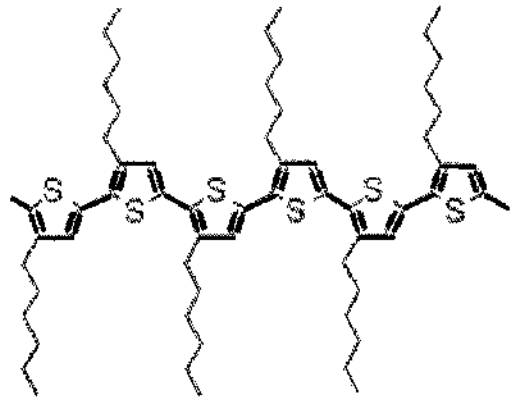

Figure 15. Segment of RR-P3HT polymer showing conjugated backbone.

This configuration is important for several reasons. Compared to regio-random P3HT where the functional groups are located arbitrarily on the carbons, RR-P3HT has a much higher hole-mobility (up to 0.1 $cm^2 V^{-1} s^{-1}$) [39]. This is due to lamellar stacking of the polymer in relatively straight chains thereby encouraging more efficient charge transfer along the conjugated backbone. Similarly, the low-bandgap polymer PCPDTBT contains a conjugated backbone. Figures 16 and 17 show the monomer unit and a segment of the polymer, respectively.

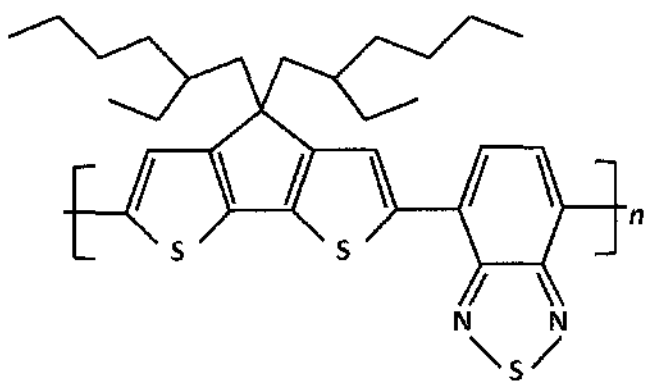

Figure 16. PCPDTBT monomer unit.

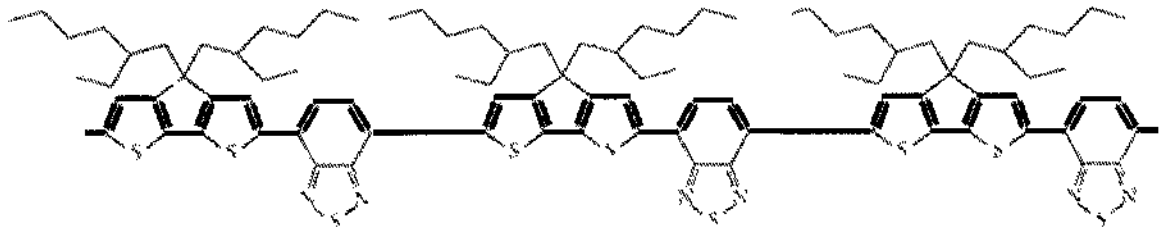

Figure 17. PCPDTBT conjugated polymer segment showing alternating single and double bonds between carbon atoms.

It is this arrangement of alternating single and double bonds between carbon atoms that gives rise to the polymers' electrical conductivity. Each carbon in the backbone is sp^2–hybridized. This mean the carbon atoms have three hybridized orbitals that are oriented 120° apart from each other as this is the most stable configuration.

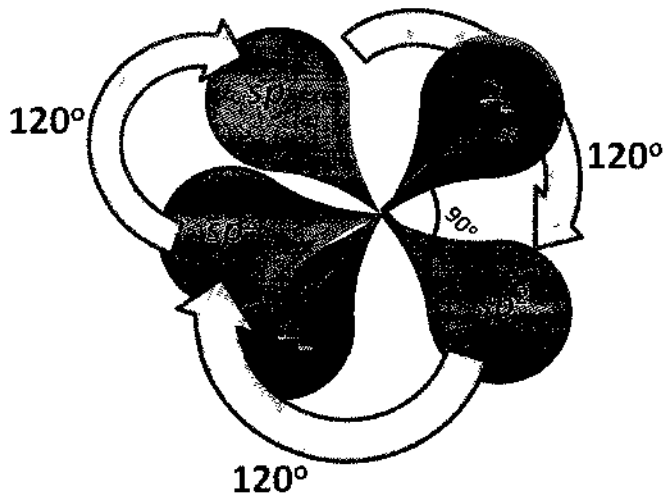

Figure 18. Schematic of sp^2-hybridized carbon atom. Each carbon atom in the backbone of the conjugated polymer, P3HT, has the trigonal structure seen; the p_z orbital lies perpendicular to the plane of sp^2 orbitals that are 120° apart from each other.

A single hybridized orbital contains one s and two p orbitals (p_x and p_y). One non-hybridized orbital remains; p_z. This orbital is perpendicular to the plane of the sp^2 orbitals as seen in Figure 18.

Along the polymer backbone, the p_z orbitals overlap each other (Figure 19) to form pi (π) bonds that allow for delocalization of charges and the subsequent flow of electrons. These bonds are parallel to the backbone and centered separately above and below the single and double bonds.

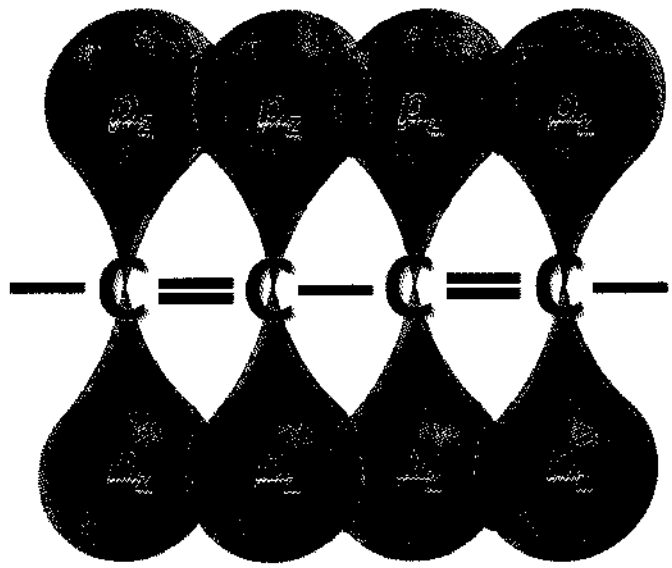

Figure 19. Overlap of non-hybridized p_z carbon atoms (sp^2 orbitals are not shown).

As a result of the Peierls instability, two energy bands are formed. These are called the *highest occupied molecular orbital* (HOMO) and the *lowest unoccupied molecular orbital* (LUMO) which are the bonding (π) and anti-bonding (π^*) orbitals, respectively [23]. Electrons travel the length of the polymer chain (and sometimes between chains) and can be "donated" to an "acceptor" polymer having higher electron

affinity [23]. Commonly used acceptors include the functionalized fullerene species [6,6]-phenyl C_{61} and C_{71}-butryic acid methyl ester ($PC_{61}BM$ and $PC_{71}BM$). C_{60} fullerene is a spherical molecule having sixty carbons. C_{70} has seventy carbons and is more "egg-shaped" than C_{60}. While the two acceptors have different absorption properties, their energy levels and bandgaps are comparable; HOMO = -6.1 eV, LUMO = -4.3 eV, and bandgap = 1.8 eV [40,41].

Much like the two bacteria and their absorption spectra shown in Figure 11, low-bandgap (LBG) and high-bandgap (HBG) donor polymers possess different absorption profiles. LBG polymers absorb light having wavelengths (λ) longer than 600 nm. P3HT – an HBG polymer – absorption extends to about 650 nm, but there is a large mismatch between its spectrum and that of the sun [3]. A comparison of the spectra of P3HT, a generic LBG, and the sun is shown in Figure 20.

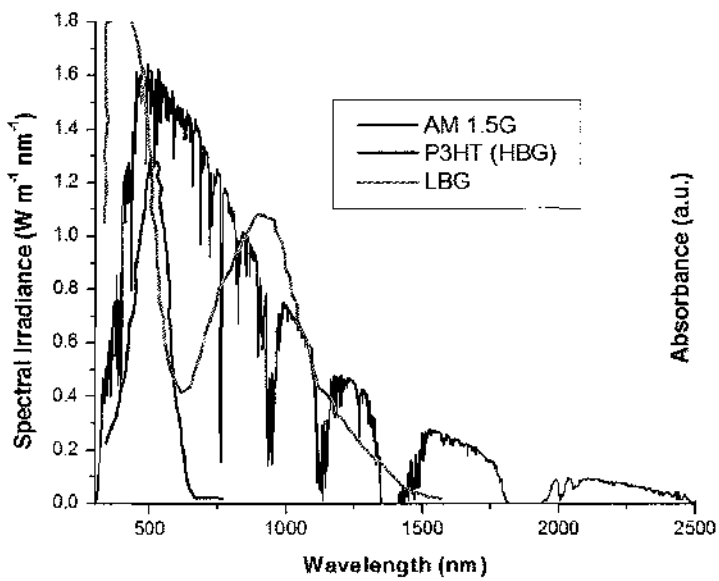

Figure 20. Absorption spectra; P3HT HBG polymer, an LBG polymer, and the solar spectrum [42].

There are primarily seven steps in the conversion of sunlight to electricity in organic solar cells. All steps introduce some degree of loss in efficiency and must be carefully considered during the fabrication of actual cells to minimize their impact. The steps are:

1. Collection of photons by the device from the environment
2. Absorption of photons in the solar cell's active layer
3. Exciton generation in the active layer
4. Exciton transport to the donor/acceptor interface
5. Exciton dissociation at the interface into separate charge carriers
6. Electron and hole transport to their respective electrodes
7. Charge collection external to the device

The details behind each step are many and only the most critical will be addressed here. The goal is to give a basic understanding of the factors critical to the "direct" conversion of solar energy to electricity through an organic solar cell.

Collection of photons by the device from the environment; Sunlight travels ninety-three million miles from the sun to reach Earth. Light must travel through Earth's atmosphere which can cause irradiance loss at the surface through a host of mechanisms including cloud cover, water vapor, and carbon dioxide (CO_2) levels. Additionally, solar cells are encapsulated by various means and this, too, adds an additional loss factor. Most often, photons must pass through glass or quartz to reach the active layer in the device and reflection can be a problem. Efforts are made to ensure that these interfaces are *optically pure*, but invariably some loss is incurred. Sometimes anti-reflection coatings are applied to the glass/quartz surface to more

seamlessly match their refractive indices to that of air. This is an important consideration since refraction occurs at every layer in a thin-film solar cell. The more dissimilar the indices are from layer-to-layer, the more severe the losses will be. Other techniques are also employed to transfer the greatest number of photons from the environment into the solar cell. One example is the manipulation of surface morphology both of the glass/quartz and subsequent layers to effectively increase the path length traversed by the light within the device. This works by maximizing the number of excitons that can be created and ultimately converted to useable charge carriers.

Absorption of photons in the solar cell's active layer; The irradiance within a solar cell at every point along the path from the front to the back of the device is proportional to the amplitude of the electric field squared and is given by the relationship:

$$I = \varepsilon_o c \langle E^2 \rangle_T \tag{5}$$

where ε_o is the permittivity of free space, c is the speed of light, $\boldsymbol{E}$ is the electric field, and the subscript T refers to the fact that irradiance corresponds to the average energy per unit area per unit time. The electric field, $\boldsymbol{E}$, is normally referred to as the *optical field* [43]. There is a strong correlation between irradiance and absorption, so it must be maximized in the active layer portion of the solar cell. This can be done in a number of ways, including through control of absorption coefficients, thickness, and sequence of all layers comprising the device. Other methods exist to enhance absorption and one of the most important in organic solar cells is to increase and improve the crystallinity of the active layer. A common technique is to use annealing

to make the BHJ absorber more like its inorganic counterparts. Annealed semi-conducting polymers achieve a greater degree of crystallinity that serves to broaden their absorption bands.

Exciton generation in the active layer; Photons of sufficient energy impinging upon electrons in a semi-conducting polymer will cause excitons to be generated. These are coulombically-bound electron/hole pairs with an overall neutral charge and binding energies generally in the range of several hundred meV [44]. Factors to be addressed in maximizing exciton generation include minimizing the attendant losses associated with such issues as spectral mismatch between the polymer and incident photons, inefficient photon capture by extremely thin nanoscale films, and physical limitations imposed due to the nature of narrow electronic transitions inherent in organics [24]. Perhaps an even more critical consideration is the very short lifetime of excitons. Once generated, the energized exciton state only lasts for approximately 1 ns. After that, radiative decay ensues in the form of photoluminescence and the exciton recombines. Therefore, it is critical that excitons undergo the next step in the energy-conversion process – diffusion to a *reaction center* – very quickly. This center is the junction of the semi-conducting donor polymer and an electron-accepting molecular species having an electron affinity greater than that of the donor. The most commonly used acceptors are the functionalized fullerenes, $PC_{61}BM$ and $PC_{71}BM$.

Exciton transport to the donor/acceptor interface; An exciton located on a polymer chain can move along the backbone due to the delocalization effects provided by the overlapping p_z orbitals on the sp^2-hybridized carbons. Excitons, in

the form of polarons, can also jump to another chain if it is in close enough proximity. However, what is key is that the exciton arrives at a donor/acceptor interface before recombination occurs. There is a typical distance an exciton is generally able to travel before recombining – the *exciton diffusion length*, L_D. This distance is approximately 5 – 10 nm. Therefore, the number of donor/acceptor interfaces should be plentiful and their spatial phase separation very small in order for the excitons to reach them in time. This is where BHJ active layers are vastly superior to bilayer types of solar cells. Still, a multitude of factors remain that will impact the efficiency of both diffusion and dissociation including the respective choice/concentrations of donor and polymer materials, the solvent used in preparing the BHJ layer (affects morphology), and crystallinity of the active layer after fabrication is complete.

Exciton dissociation at the interface into separate charge carriers; When excitons arrive at the interface of two donor/acceptor polymers having a difference in their LUMO levels greater than the exciton binding energy, dissociation – a cleavage into separate electron and hole charge carriers – can occur. Figure 21 shows a representation of exciton dissociation at the junction of the LBG polymer, PCPDTBT, and the acceptor $PC_{61}BM$. At this critical stage of the PV process, two common loss mechanisms can adversely impact ultimate device efficiency: geminate and bimolecular recombination. In geminate recombination, the nascent electron and hole carriers merge back into an exciton at the interface because the field strength established by the donor/acceptor LUMO energy levels is insufficient to overcome the combined electrostatic attraction and the additional energy loss associated when

the electron transfers to the acceptor. The newly reconstituted exciton will then fully recombine.

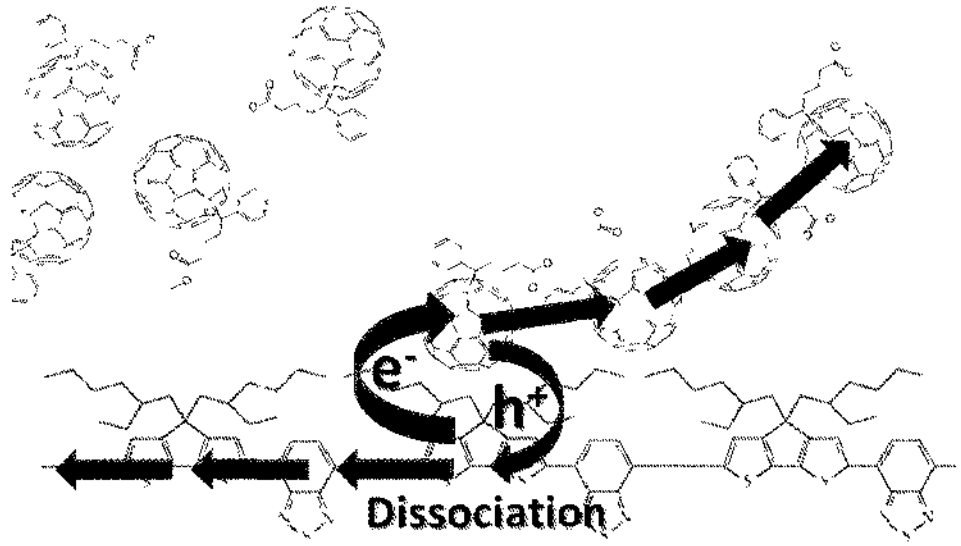

Figure 21. Exciton dissociation at the interface of the donor polymer, PCPDTBT, and acceptor $PC_{61}BM$.

An additional type of recombination is non-geminate bimolecular, or *Langevin*, recombination. In this mode, electrons and holes from *different* excitons merge. This takes place in the bulk and not at interfaces. Trapped charge carriers can also combine with those that are mobile for a third type of recombination loss.

Electron and hole transport to their respective electrodes; Similar to inorganic semi-conductors, charge carriers transport to their respective electrodes via drift and diffusion. Drift current results from the internal electric field established by the energy difference between the HOMO of the donor and the LUMO of the acceptor.

This field not only induces carrier drift, but is also a key determinant of the maximum V_{OC} achievable [45]. Diffusion current is a result of charge carrier concentration gradients. However, unlike charge transport in highly-crystalline, well-ordered inorganic semi-conductors, disordered semi-conducting polymers suffer from lower carrier mobilities and greater degrees of charge trapping. These factors alone have a marked impact on overall achievable device current and voltage as well as power conversion efficiency. Also, recombination continues to be a problem throughout the entire transport process from dissociation to charge collection at the electrodes. In BHJ organic solar cells where long range structural order does not exist as it does with inorganics, charge transport occurs via carrier hopping between localized energy states. Donor polymer chains transport the holes to the anode while acceptors (e.g., fullerene) conduct electrons to the cathode. This dictates that charge transport will be slow and mobilities much lower than in inorganics. A primary technological focus aimed at mitigating the limitations inherent in charge transport involves improvement of active layer morphology by increasing its crystallinity.

Charge collection external to the device; The journey from photon absorption in the BHJ active layer to charge collection at the electrodes is a long one. Macroscopic characteristics such as serial and shunt resistances in the device are impacted by many factors such as inter-layer interface characteristics (transparency, resistance, etc.), polymer blend factors (donor/acceptor concentrations, solvent choice, fabrication methods, etc.), and layer morphology (absorption coefficient, dielectric constant, thickness, etc.). These and many other issues determine the efficiency with which charge carriers successfully arrive at their respective electrodes and can be conducted

efficiently from the PV device to external circuitry. An active area of research continues to be exploring the best ways in which to connect metal oxide and metal electrode materials to organic matter in such a way as to maximize current collection.

CARRIER MOBILITY IN A GAUSSIAN DENSITY OF STATES

Disordered organic blends do not have a predictable isotropic crystal lattice structure, and therefore the descriptive physics are different from those used for inorganic crystalline structures. In particular, the equations depicting the mechanisms behind charge transport are basically derivative of those commonly used to describe the phenomena in inorganics. This works to a large extent, but there are difficulties in the case of carrier mobility – a critical factor impacting transport. More specifically, charge carrier mobility (μ_e *and* μ_h) is considerably different both qualitatively and quantitatively in semi-conducting organic polymer BHJ devices. For example, in crystalline semi-conductors such as silicon, charge transport occurs via band transport as opposed to the *hopping* between localized energy states in disordered organics [23]. Carrier *concentration* is also inextricably linked with mobility in all cases. Mobilities in doped Si at room temperature can be as high as 450 and 1400 $cm^2\ V^{-1}\ s^{-1}$ for p-type and n-type, respectively [46]. By comparison, hole and electron mobilities in BHJ organic blends consisting of P3HT and PCBM are very slow in the range of 10^{-3} to 10^{-7} $cm^2\ V^{-1}\ s^{-1}$.

For disordered semiconducting polymers, it is widely assumed that hopping mobility must be analyzed from the standpoint that the density of states (DOS) is represented by an exponential or Gaussian distribution [47,48,49,50]. In donor/acceptor BHJ structures, the donor polymer is primarily a hole-conductor while the acceptor molecule transports the electrons [23]. Over the years, several models have been

proposed to accurately describe mobility with varying degrees of success. With this in mind, four models are briefly described as they apply to the issue of mobility and carrier concentration in organic semiconductor materials. The models are the 1), Pasveer, 2) Movaghar-Schirmacher (MS), 3) Vissenberg-Matters (VM), and 4) Arkhipov.

Pasveer Model; This model starts from the "master equation" for hopping transport behavior in disordered materials having a *Gaussian density of states* and presents a model intended to comprehensively describe charge carrier mobilities in disordered semiconducting polymers. He incorporates the impact of temperature, electric field, and charge carrier density on mobility and the subsequent influence on the current/voltage characteristics in experimental polymer devices. The model is reported to accurately describe real devices and two important temperature regimes are identified; 1) at *room temperature*, mobility is primarily impacted by carrier density, and 2) at *low temperatures* (and correspondingly high field strength) the mobility is strongly dependent on the electric field.

A critical parameter determining polymer device performance is the charge-carrier mobility, μ. In disordered polymers, charge transport is understood to take place via a hopping process along and between the segments of the conjugated chain. The energy level variations at each site in the chain can be described by a Gaussian distribution. In previous models, the affects of temperature and electric field have been examined in order to understand how these factors impact μ. More recently, the significance of charge carrier density, p, has been realized and its influence on mobility taken into account. It's been found that at room temperature, only charge

carrier density need be considered when determining mobility, but that at low temperatures μ will depend on the electric field.

The master equation that describes charge carrier hopping on an ordered lattice is:

$$\sum_{j \neq i} [\, W_{ij}\, p_i(1 - p_i) - W_{ji} p_{ji}(1 - p_i] = 0 \tag{6}$$

p_i is the probability that site i is occupied by a charge, W_{ij} represents transition rate from i to j, and $(1 - p_i)$ ensures that only one charge can occupy a site at any particular time. The transition rates are of the following form:

$$W_{ij} = \begin{cases} v_0 \exp[-2\alpha R_{ij} - \beta(\varepsilon_j - \varepsilon_i)], & \varepsilon_j \geq \varepsilon_i, \\ v_0 \exp[-2\alpha R_{ij}], & \varepsilon_j < \varepsilon_i \end{cases} \tag{7}$$

β is equivalent to $1/k_BT$, v_0 is an intrinsic rate value, and R_{ij} is equivalent to $|\mathbf{R}_j - \mathbf{R}_i|$ which represents the distance between hopping sites i and j. ε_i represents the energy at site i and α is the inverse localization length. Not shown is a contribution due to the electric field having a value of $-eER_{ijx}$. e is the charge of the carriers and x indicates the direction of the field is in the x direction. When an electric field is absent, charge occupational probability is described by the Fermi-Dirac distribution.

To simplify the model, Pasveer assumed a cubic lattice structure with lattice constant a. The inverse localization length, α, is equal to 10/a. By varying α, the mobility prefactor can be changed which allows the model to employ variable-range hopping. Figure 22 shows the mobility as a function of carrier density for a selection

of temperatures and decaying electric field. The symbols in the figure represent numerical results and the solid lines are fits based on the following parameterization methodology:

$$\mu(T, p) = \mu_0(T)\exp[\tfrac{1}{2}(\hat{\sigma}^2 - \hat{\sigma})(2pa^3)^\delta],$$
$$\mu_0(T) = \mu_0 c_1 \exp[-c_2\hat{\sigma}^2],$$
$$\delta \equiv 2\frac{\ln(\hat{\sigma}^2 - \hat{\sigma}) - \ln(\ln 4)}{\hat{\sigma}^2}, \quad \mu_0 \equiv \frac{a^2\nu_0 e}{\sigma}, \tag{8}$$

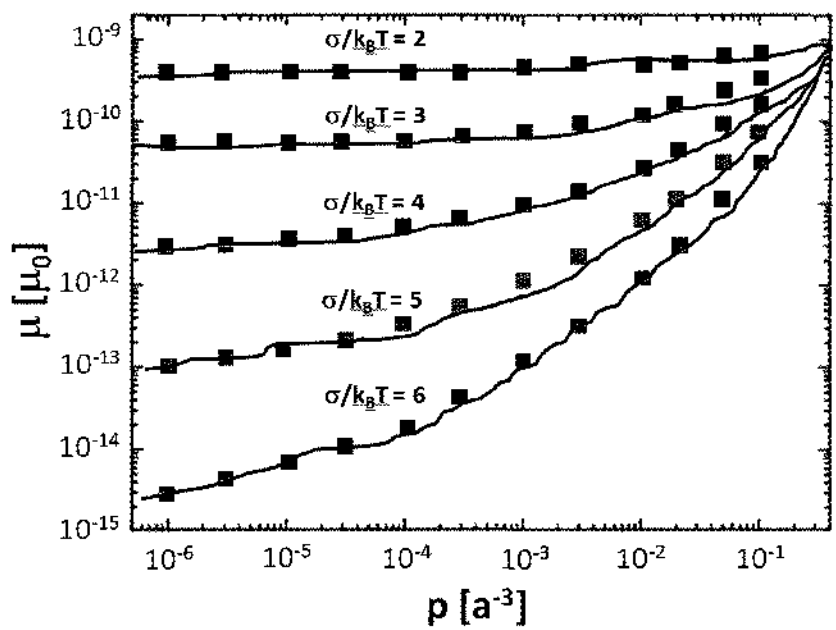

Figure 22. Mobility as a function of carrier density for different T and E [49].

The coefficients c_1 and c_2 are determined empirically and are equal to 1.8e-9 and 0.42, respectively. This parameterization is suitable when densities are not too high.

This model accurately uses a Gaussian distribution to describe energy variations at sites located on polymer chains in disordered semiconductor materials. It also

shows that mobility is primarily dependent on carrier density at higher temperatures, but a consideration of electric field is necessary to accurately detail *J-V* characteristics at low temperatures and high fields. A limitation of this model is that a uniform, regularly-spaced lattice structure is assumed. This is a "drastic approximation" that differs markedly from the reality found in actual polymers [49]. As a result, the researchers suggest their results be considered as "the effective result of an average of intrachain and interchain hopping" [49].

Movaghar-Schirmacher (MS) and Vissenberg-Matters (VM) models; These models had either not been applied previously to the analysis of organic materials with disordered states having a Gaussian distribution, or were used but found to have inaccuracies that required modifications [47]. It was found that mobility is constant below certain charge-carrier concentrations. Mobility will decrease when the ratio of the width of the DOS to the thermal energy, k_BT, increases. This ratio is designated as "$\hat{S}$". Correspondingly, mobility will increase with larger carrier concentrations up to an identifiable limit. At very high concentrations the mobility will be limited by final state effects – although there can even be a decrease in mobility at these high concentration levels. For each of the models, an analytical expression for mobility, μ, is given where

μ = (mobility of low concentration) x (concentration (c)) x ($\hat{S}$-dependent factor)

Depending on the value of the concentration, c, $\ln(\mu)$ will vary in an approximately linear way as $1/T$ or $1/T^2$ where T is temperature.

Both the MS and VM models describe two basic mobility regimes. There is a "crossover" point between the first and second regimes that depends on charge-carrier

concentration. In the first, the mobility is independent of the concentration and carriers effectively obey Boltzmann statistics as opposed to Fermi-Dirac statistics. Above a critical concentration level, mobility increases with increasing carrier concentration. In a Gaussian disorder model, the density of states is described by the following relation:

$$g(E) = \frac{N_t}{\sqrt{2\pi}\sigma_{\mathrm{DOS}}} \exp\left(-\frac{E^2}{2\sigma_{\mathrm{DOS}}^2}\right) \tag{9}$$

where σ_{DOS} is the width of the DOS and N_t is the total number of hopping sites in a cubic meter (m^3). When carrier concentration is low and Ŝ >>1, charge carriers are effectively independent and mobility is independent of concentration in this "Boltzmann regime". As more carriers are added, a critical point ($E_f = E_0$) is exceeded and the density of states is filled to higher energy levels. As a result, the "average number of unoccupied neighbor sites within a certain spatial and energetic distance is then on average larger, so that the mobility increases with increasing concentration" [47]. Two key results are observed. First, when Ŝ is greater than 2, the mobility at the crossover carrier density point ($E_f = E_0$) is approximately equal to twice the mobility of the low carrier density limit as described by

$$\frac{\mu[n(E_F = E_0)]}{\mu(n = 0)} \cong 2 \tag{10}$$

This relation holds regardless of the GDM used. In addition, carrier concentration ($c = n/N_t$) at the crossover point between the low and high concentration regimes is given exactly by

$$c(E_F = E_0) = \tfrac{1}{2}\exp\left(-\tfrac{1}{2}\hat{s}^2\right) \tag{11}$$

Both of these relationships allow the estimation of the width of the DOS from the carrier concentration dependence of the mobility at specific fixed temperatures.

As described in the Pasveer model, both the MS and VM models use the Miller-Abrahams rate constants given by Equation (7) and which is shown again here for convenience:

$$W_{ij} = \begin{cases} \nu_0 \exp[-2\alpha R_{ij} - \beta(\varepsilon_j - \varepsilon_i)], & \varepsilon_j \geq \varepsilon_i, \\ \nu_0 \exp[-2\alpha R_{ij}], & \varepsilon_j < \varepsilon_i, \end{cases} \tag{7}$$

The hopping rate is w_{ij}, ε_i is the initial site, ε_j is the destination hopping site, and R_{ij} is the distance between the two. ν_0 is an "attempt frequency" and α is the inverse of the decay length of the localized wave functions – taken to be equal for all sites. ν_0 depends on "electron-phonon coupling strength, phonon density of states, and other material properties" [48].

In the MS model, conductivity is expressed as follows:

$$\sigma \cong \frac{e^2}{k_B T}\frac{\langle R^2 \rangle}{6} B_{\mathrm{MS}} \nu_0 \int_{-\infty}^{+\infty} g(E)\sigma_1(E)dE. \tag{12}$$

Conductivity is an integral function that accommodates contributions from all the energy sites where $<R^2>$ is the average of the square of the hopping distances. The full expression for σ is given by

$$\sigma_1(E) = \frac{4\pi}{B_{MS}} \int_{-\infty}^{\infty} g(E')dE' \int_0^{\infty} \frac{R^2}{\exp\left(2\alpha R + \frac{|E - E_F| + |E' - E_F| + |E - E'|}{2k_B T}\right) + \frac{1}{\sigma_1(E')}} dR \tag{13}$$

This is a more accurate representation of σ since it is a double integral that accounts for both R and E. The simplified version is used when the hopping processes considered are those whose contributions are based on the average distance between sites. B_{MS} is a "percolation correction factor" given by B_{MS} = exp(Equation (9)). The MS model must be solved iteratively which means the mobility calculation can be computationally demanding.

The VM percolation model addresses an exponential DOS and views the system as a random resistor network. Conductance between hopping sites is given by $G_{ij} = G_0 \exp(-s_{ij})$ where $G_0 = e^2 \nu_0/(k_B T)$ and

$$s_{ij} = 2\alpha R_{ij} + \frac{|E_i - E_F| + |E_j - E_F| + |E_i - E_j|}{2k_B T} \tag{14}$$

This relationship expresses equilibrium current densities based on contributions proportional to the Miller-Abrahams parameters described in Equation (7). These parameters are multiplied by the initial and final state Fermi factors under a zero-field

limit and under the condition that the relevant hopping energies are large when compared to the thermal energy (k_BT). In this model, the conductivity is proportional to the "critical conductance" given by $\sigma = \sigma_0 \exp(-s_c)$ and σ_0 is proportional to G_0. If all "resistor" connections in the network for which $s_{ij} > s_c$ are disregarded, each energy site that is not disconnected from all other sites will have an average of "B_{VM}" connections or "bonds" to the other sites. Based on numerical calculations, B_{VM} is found to be equal to 2.8 and only states within $s_c k_B T$ from E_F participate in the percolation network. s_c can be found by solving Equation (15):

$$\frac{N_b(s_c)}{N_s(s_c)} = B_{\mathrm{VM}} \tag{15}$$

where N_s is the density of participating sites and N_b is the density of bonds between these sites. By applying this model to the case of an exponential DOS, Vissenberg and Matters were able to develop an analytical expression for the mobility. The problem can be solved numerically for a Gaussian DOS where the density of participating sites is given by

$$N_s = \frac{N_t}{2}\left(\mathrm{erf}\left[\frac{E_F + s_c k_B T}{\sqrt{2}\sigma_{\mathrm{DOS}}}\right] - \mathrm{erf}\left[\frac{E_F - s_c k_B T}{\sqrt{2}\sigma_{\mathrm{DOS}}}\right]\right) \tag{16}$$

and the density of bonds is

$$N_h = \int d^3 R_{ij} \int_{-\infty}^{+\infty} dE_i \int_{-\infty}^{+\infty} dE_j \, g(E_i) g(E_j) \theta(s_c - s_{ij}) \tag{17}$$

In Equation (16), "erf" is the error function. In Equation (17), R_{ij} is the integral over the entire space and θ is the Heaviside unit step function.

Arkhipov model; An assumption made with the Arkhipov model is that the first carrier hop from a site having energy E is to a neighbor site where the Miller-Abrahams hopping rate is the greatest. In other words, to the site where the function

$$u = 2\alpha R + \theta(E' - E)\frac{E' - E}{k_B T} \tag{18}$$

is the smallest. R is the distance between the sites where E' is the final energy state. θ is the Heaviside step function and the mobility is then described as

$$\mu = \frac{e\nu_0}{k_B T} \int_{-\infty}^{\infty} \exp[-\langle u \rangle(E)] \langle R^2 \rangle(E) h(E) dE \tag{19}$$

$\langle u \rangle(E)$ is the average value of the mobility when the charge carrier hops to the next site and $\langle R^2 \rangle(E)$ represents the average of the square of the hopping distance to the next site. $h(E)$ is the normalized density of occupied states which can also be written as

$$g(E)f(E)/n \tag{20}$$

Here, $f(E)$ is the Fermi-Dirac distribution function and $g(E)$ is the density of states. $\langle u \rangle(E)$ can be further expanded as follows:

$$\langle u \rangle(E) = \int_0^{\infty} \exp\left(-\frac{n(E,u')}{B_{\mathrm{Ark}}}\right) du' \tag{21}$$

$n(E,u')$ is the average number of neighbor sites for $u < u'$ and is given by

$$n(E,u') = \frac{4\pi}{3}\left(\frac{u'}{2\alpha}\right)^3 \left[\int_{-\infty}^{E} g(E)dE + \int_{E}^{E+k_B Tu'} g(E') \times \left(1 - \frac{E'-E}{kTu'}\right)^3 dE' \right]. \tag{22}$$

In this model, B_{Ark} represents the *average number of connections (or "bonds")* to *other sites* and is equal to 1. It is a "percolation parameter" analogous to B_{MS} and B_{VM} in the Movaghar-Schirmacher and Vissenberg-Matters models, respectively.

Equation (19) above is derived by making two assumptions: 1) the contribution to the diffusion constant due to carriers at sites with energy E is given by $\nu_0 \exp[-\langle u \rangle(E)]\langle R^2 \rangle(E)$, and 2) the diffusion constant is related to the mobility via the Einstein equation for non-interacting particles. By integrating over the initial state energy E and realizing that for hopping at low carrier concentrations in a Gaussian DOS that the average square hopping distance is approximately equal to the square of the average intersite distance, the full expression for $\langle R^2 \rangle(E)$ does not have to be used and the mobility can be obtained.

The analysis of carrier mobility in disordered semiconducting polymers is critical to understanding charge transport mechanics in organic photovoltaics. However, there are considerable differences between organic materials and homogeneous inorganic structures where physical parameters are often more amenable to objective definition. Currently, Gaussian disorder models are the best means for describing hopping mobility inherent in disordered polymers. Still, as more is learned, other methods and modifications will likely be necessary to comprehensively elucidate the true mechanisms behind this phenomenon.

CHARGE CARRIER RECOMBINATION

The primary measure of an organic solar cell's performance is its power conversion efficiency, η. This is defined as the ratio of output electrical power (P_{out}) to the input optical power (P_{in}). Equivalently, the fill factor, current density, and open circuit voltage determine the PCE as shown in Equation (23):

$$\eta = \frac{P_{out}}{P_{in}} = \frac{FF\ J_{SC}\ V_{OC}}{P_{in}} \tag{23}$$

As can be seen in the relationships above, current density, J_{SC}, is a factor upon which PCE is heavily dependent. Several mechanisms work to diminish the overall efficiency and many of them do so by directly impacting current density. Current through an OSC device is of two types; drift and diffusion. The relationship in Equation (24) shows the components making up each kind of current and how they add to describe current *density*. Current density is not only a function of the amount and rate of charge carrier flow, but is

also dependent on the *volume* through which it passes. This becomes critical when dealing with the extremely thin layers typically found in organic solar cells.

$$J_{total} = J_{drift} + J_{diffusion} = en\mu E + kT\mu\nabla n \tag{24}$$

where e is the elementary electronic charge, n is charge carrier concentration, μ is carrier mobility, E is the applied electric field, and ∇n is the carrier concentration gradient [51]. It's clear that mobility and concentration are the most important influences on current density.

Carrier concentration, n, is a function of electron/hole lifetime. Therefore, the deleterious effects of recombination must be controlled. Excessive recombination results in an unacceptable decrease in available charge carriers, which reduces current density and ultimately drives down the PCE. The lower mobility of carriers in organic semi-conducting polymers is also more problematic when compared to crystalline inorganics. Lower mobility in bulk materials results in greater recombination and a subsequent reduction in efficiency. It is therefore necessary that organic thin film layers be made exceedingly thin (nanoscale) [52]. As previously addressed, other steps (e. g., annealing, choice of donor/acceptor polymers and solvents, etc.) are also taken during solar cell fabrication to mitigate the problems associated with low carrier mobility in BHJ polymer layers. One of the most powerful techniques involves thermal annealing of the active layer. This has the effect of making chain polymers assume a more ordered, lamellar conformation that, to varying degrees, mimics the structure in inorganic solar cells. This, in turn, increases charge carrier mobility and reduces recombination. In this study,

regioregular P3HT is the HBG polymer modeled in the simulations. In actual device fabrication, P3HT:PCBM active layers are post-annealed in an H_2O- and N_2-free environment to achieve an enhanced semi-crystalline morphology. Figure 23 shows a representation of post-annealed P3HT.

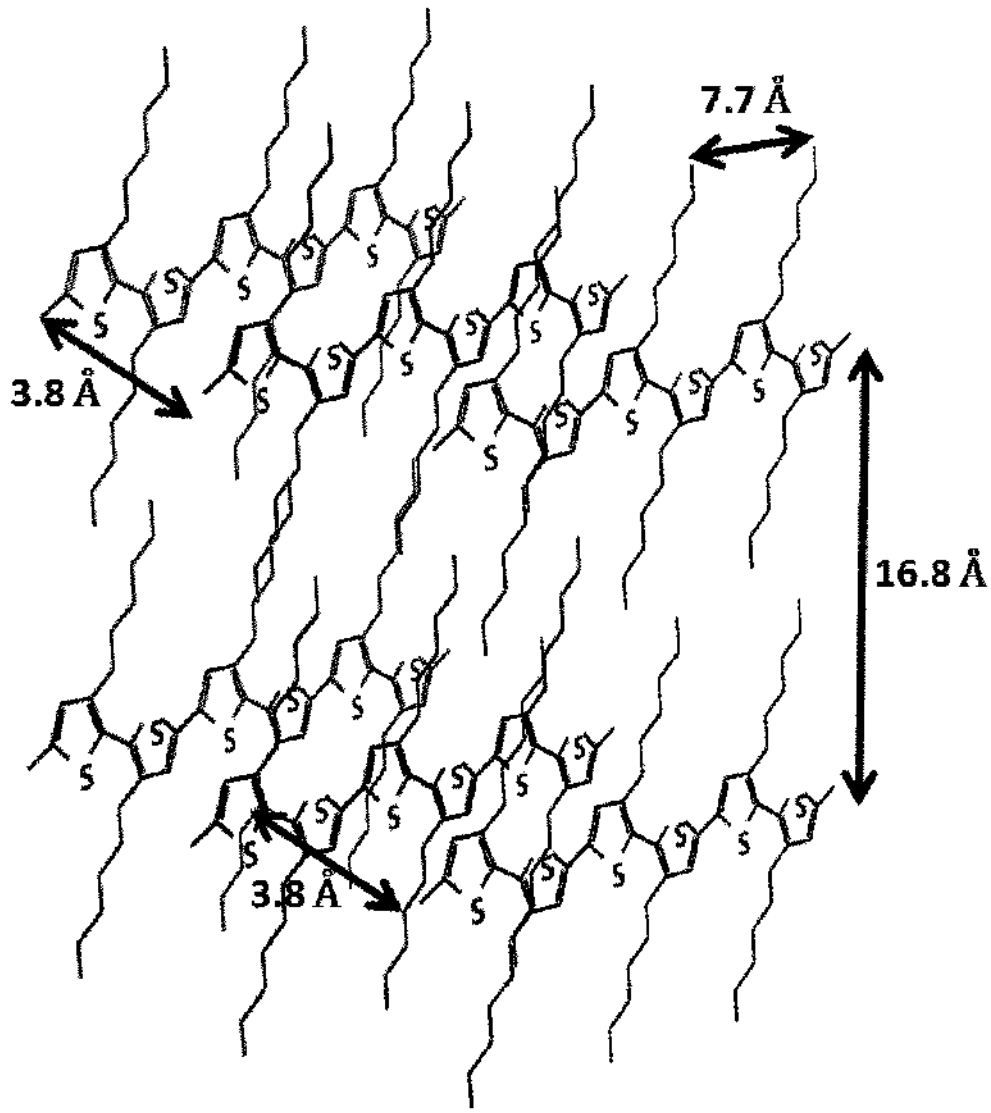

Figure 23. Effects of annealing on P3HT; the polymer becomes more lamellar and ordered and therefore more semi-crystalline [53].

Using diffraction techniques such as grazing-incidence x-ray diffraction (XRD), researchers have been able to determine some of the physical features of semi-crystalline P3HT [54,55]. Figure 23 shows that in a lamellar configuration, there is a distance of about 3.8 Å between "sheets" of polymer. The inter-chain distance between polymer segments in the same sheet is 16.8 Å and 7.7 Å separate adjoining hexyl groups on each carbon 3.

When excitons are photogenerated in an organic BHJ active layer, they diffuse to the donor/acceptor interface and, if conditions are energetically favorable, dissociate into separate electron and hole charge carriers. However, this separation must be maintained so that transport to their respective electrodes can occur. At the moment of dissociation, the Coulomb force must be overcome or *geminate* recombination occurs. Originally, the mechanics behind ion recombination were described for inorganic crystalline materials by Onsager and his theory of ion recombination. The theory posits that when photo-ionization occurs, the electrons and holes are quickly thermalized causing a small separation between the two (*excitons* in organic semi-conductors) – a point in time when the charges are in the *charge transfer* (CT) state. From that point, the Coulomb force and the internal electric field work on the charge pairs until one of two things happen: 1) the charges recombine, or 2) they overcome the Coulomb force, fully separate, and transport to electrodes to become useful current [56]. Figure 24 shows a diagram of the Coulomb radius and some representative mobile charges. In this scenario, both an electron and a hole are attracted to each other by the Coulomb force. If the hole is within the Coulomb radius, the external field is zero, and the thermalization energy is insufficient or hopping distance is too great to overcome the Coulomb force, the charges will recombine.

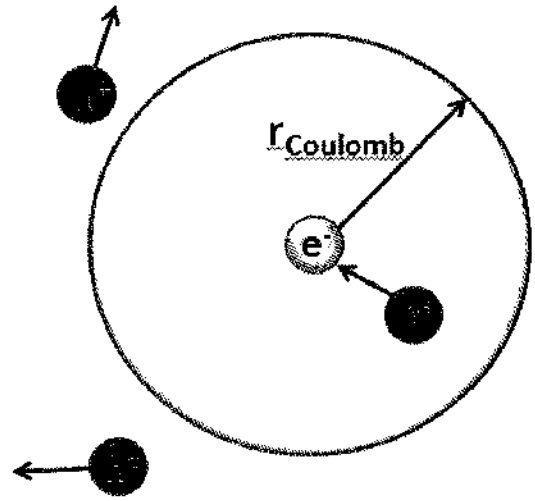

Figure 24. Coulomb radius and recombination.

In the absence of an external electric field, the Coulomb radius is given by the following:

$$r_{coulomb} = \frac{e^2}{4\pi\varepsilon_r\varepsilon_0 kT} \tag{25}$$

where e is the charge on the electron, ε is the relative permittivity, ε_0 is the permittivity of free space, k is the Boltzmann constant and T is temperature. This radius is correlated with the probability of charge separation [51]. Holes that lie outside the radius will not combine and be available for conduction.

There is a second type of recombination referred to as *bimolecular*, or *Langevin* recombination that occurs not at donor/acceptor interfaces, but in the bulk of the active layer. Electrons and holes that recombine there originate from different excitons. In this case, a rate equation is defined to describe generation, recombination, and charge collection:

$$R_{Generation} = R_{Collection} + R_{Recombination} \tag{26}$$

where $R_{Recombination}$ in simplified form is given by Equation (27):

$$R_{Recombination} = \beta np = \beta n^2 = \frac{n}{\frac{1}{\beta p}} = \frac{n}{\tau_\beta} \tag{27}$$

τ_β is the bimolecular, concentration-dependent carrier lifetime, n and p are the electrons and holes, respectively, and β is the recombination coefficient that defines recombination rate and carrier lifetime [51]. Langevin recombination is normally observed in low mobility materials having small carrier hopping distances, but a large $r_{Coulomb}$, pristine π-conjugated polymers [57], and unannealed, low-efficiency solar cells [58]. In this case, a Langevin recombination coefficient, β_L, is defined as

$$\beta_L = \frac{e(\mu_{faster} + \mu_{slower})}{\epsilon_r \epsilon_0} \tag{28}$$

where μ_{faster} and μ_{slower} refer to the relative speeds of the charger carriers. Ideally, the mobility rates would be equal. This would mean that electrons and holes are collected at the same rate, thereby avoiding charge buildup at the interfaces. In response to this fact, Equation (27) was adapted by Braun to allow for a *spatial averaging* of the electron and hole mobilities since both charge carriers are confined to different phases [59]:

$$\beta_L = \frac{e}{\epsilon_r \epsilon_0} \langle \mu_n + \mu_p \rangle \tag{29}$$

The brackets denote the spatial averaging. Still, it remains that charge collection will be dictated by the charger carrier with the lowest mobility. Therefore, it is more accurate to write Equation (29) as

$$\beta_L = \frac{e}{\epsilon_r \epsilon_0} \min(\mu_n, \mu_p) \tag{30}$$

In inorganic semi-conductors, the Langevin recombination constant is normally taken to be 1. However, in organic polymer blends, the value is ~0.1. This is the value used in the simulations in Chapter 3 as it has been shown empirically to be reasonably accurate.

OPTICAL AND ELECTRICAL MODELING

The first two steps in the solar energy conversion process enumerated on Page 29 are:

1. Collection of photons by the device from the environment, and
2. Absorption of photons in the solar cell's active layer

Both of these steps are inherently *optical* in nature and are commonly described using well-established and highly effective formalisms recognized in the science of matrix mathematics. In particular, the *Transfer Matrix Method* (TMM) is frequently used to calculate the irradiance as a function of the electric field squared within each cell layer at a continuum of points while traversing the entire depth of the multi-layer structure. The two primary inputs to any such algorithm are the thickness and the real and imaginary components (n and k) of the complex indices of refraction for each layer in the device.

A step-wise, scalar wave approach to simulating the optical characteristics of multi-layer structures has widespread application to many types of problems. Previous

work done by this researcher involved the application of TMM to the study of fiber Bragg grating (FBG)-based chemical sensors used to detect toxic industrial chemicals and toxic industrial materials (TIC/TIM) [60]. These chemicals and materials can be used by terrorist organizations to contaminate food and water supplies and the U.S. government has identified a need to develop technology capable of detecting them [61]. Fiber Bragg gratings are formed in specially doped fiber optic glass core materials by irradiating the fiber with UV light through a mask. This produces "layers" of periodic, alternating indices of refraction within the fiber. FBGs will then reflect specific light frequencies and transmit the others through unimpeded. The wavelength that will be reflected is determined based on the thickness and refractive indices of the FBG segments or *planes*. This makes FBGs useful as optical filters or wavelength-specific reflectors. As an example, Figure 25 shows the schematic of an FBG sensor that was designed using the polymer cellulose acetate (CA) as a transducer. The CA is deposited on the outside of the FBG-containing glass fiber and allowed to cure. While transmitting a reference light wavelength through the fiber, it is then dipped into an analyte (e.g., oxalic acid, ethylene glycol, sodium hypochlorite, etc.). The polymer coating interacts with the analyte and swells to varying degrees depending on which target chemical is being tested. This swelling of the polymer subsequently strains the fiber and the FBG contained within. This elongation of the fiber effectively changes the *thickness* of each layer in the FBG which causes an increase in Bragg period (Λ_B) and a resultant shift in Bragg reflectance wavelength (λ_B) [60].

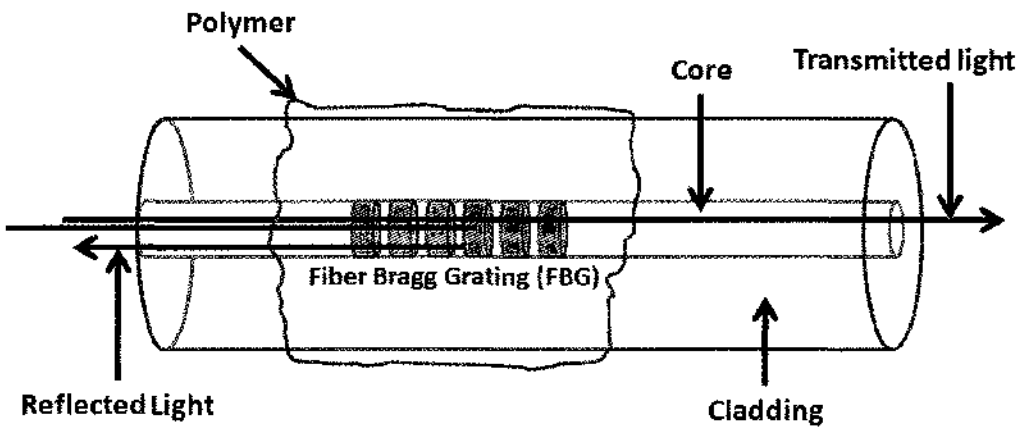

Figure 25. Polymer-coating on fiber containing a single Bragg grating [60].

The experimental work in the study was augmented with computer simulation as well. Using MatLab©, an FBG modeling tool was developed based on the TMM. The tool allows transmittance and reflectivity to be calculated over a user-selected range of wavelengths and variables such as indices of refraction and number and thickness of Bragg planes in the grating can be manipulated. Figure 26 shows the user interface for the simulation tool.

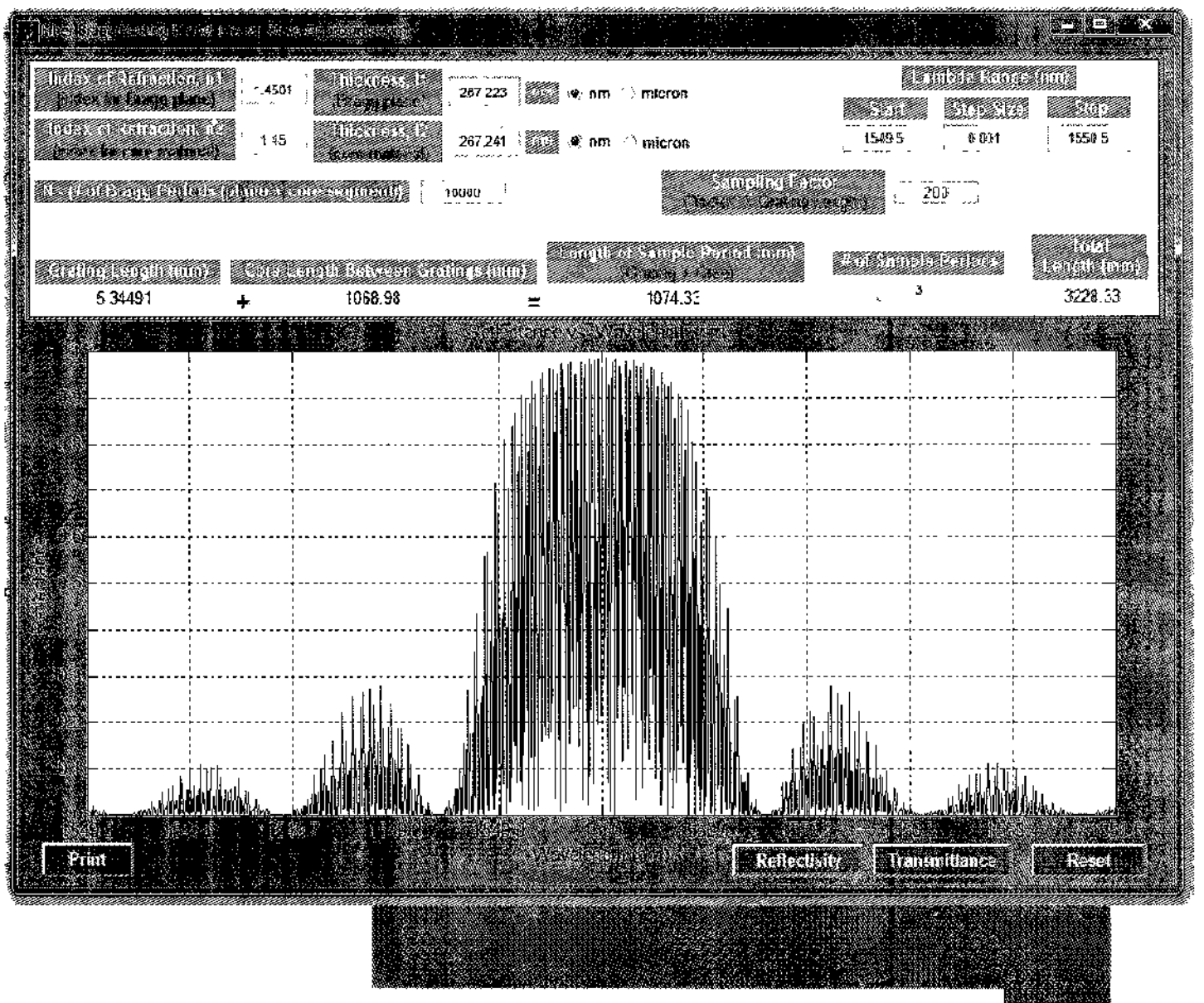

Figure 26. Graphical user interface for Fiber Bragg grating simulation tool.

In this dissertation, TMM-based modeling of stacked layers lends itself well to research on organic solar cells. MatLab© was used to develop the algorithms to calculate reflectivity, transmission, and absorption profiles in multi-layer structures using a conservation of energy approach:

$$R + T + A = 1 \tag{31}$$

where R is reflection, T is transmission, and A is absorption. Additional outputs include electron and hole current densities, charge carrier densities, and exciton generation statistics. A one-dimensional, or scalar wave approach is suitable considering the cell layers are stacked on top of each other and the angle of light incidence is taken to be perpendicular to the plane of each layer. Other assumptions are that the layers are smooth (morphology is not considered in this model) and all layers are parallel.

For the optical analyses conducted on tandem cells in this study, the TMM was implemented over a wavelength range from 350–900 nm using standard AM 1.5 sunlight spectra. The optical properties of all the layers are described based on their complex refractive indices, $n' = n(\lambda) + ik(\lambda)$, which are either experimentally obtained from spectroscopic ellipsometry or from the literature [35]. In particular, the refractive index values for P3HT:$PC_{71}BM$ and PCPDTBT:$PC_{61}BM$ are extracted from Ref. [35]. For a given set of bottom and top active layer thicknesses, the number of photons (N_{ph}) absorbed in the top and bottom layers are calculated in each subcell as shown in Figure 27. The absorbed photons are converted to photocurrent by considering charge carrier transport and bimolecular recombination processes and designing optimal bottom layer

(d_{bottom}) and top layer (d_{top}) thicknesses for each subcell. The maximum thickness considered was around 300 nm due to the fact that both bimolecular recombination and internal resistance of the device significantly increase with excessive thickness. Both of these factors adversely affect energy conversion efficiency.

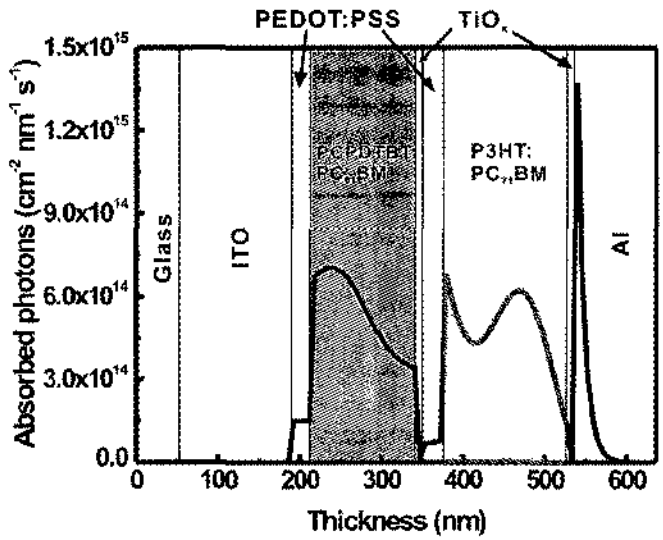

Figure 27. Number of photons (N_{ph}) absorbed in the top and bottom subcell layers [130].

Outputs from the model are used to calculate such device parameters as J_{SC}, V_{OC}, FF, and PCE. Graphical representations of these calculations for several tandem organic solar cell structures can be seen in Chapter 3.

Steps 3 through 7 listed on Page 28 can be classified as *electrical* in nature. Standard equations used in the description of inorganic semi-conductor physics can be used to describe organic semi-conductor phenomena, albeit with some modifications. The absorbed photons in organic blends generate electron-hole (e-h) pairs or excitons, some of which subsequently dissociate into free-charge carriers at the BHJ interfaces as described by Onsager–Braun theory [59,62]. The transport of dissociated free-charge

carriers and Langevin bimolecular recombination [63] are incorporated into a one-dimensional drift-diffusion model and used to estimate the current density and efficiency of organic solar cells. In this model, the mobilities of electron and hole carriers are assumed to be independent of the electric field which is taken to be constant within the organic blends. The net generation rate, $U(x)$, of free-charge carriers can be expressed as [64]

$$U(x) = P(x)[G_{\text{e-h}}(x) + R(x)] - R(x), \tag{32}$$

where $P(x)$ is the dissociation probability of bound e-h pairs. $G_{\text{e-h}}(x)$ is the generation rate of photo-induced e-h pairs and R(x) is the Langevin bimolecular recombination rate (also β_L) expressed as

$$\beta_L = k_r[n(x)p(x) - n^2{}_{\text{int}}], \tag{33}$$

where

$$k_r = (q/\varepsilon)\ \min(\mu_n, \mu_p) \tag{34}$$

The electron and hole charge carriers are recombined at the rate, k_r, with respect to the intrinsic carrier density $n^2{}_{\text{int}}$. One should note that k_r is dictated by the mobility of the slower carrier in Eq. (34).

More specifically, the e-h pair dissociation probability at a given pair distance, ξ, is given by

$$p[\xi, F(x), T] = \frac{k_d[\xi, F(x), T]}{k_d[\xi, F(x), T] + k_f(T)} \tag{35}$$

where k_d is the e-h dissociation rate and k_f is the decay rate to the ground state. The dissociation rate is a function of the e-h pair distance, field strength (F), and temperature (T)

$$k_d[\xi, F(x), T] = \left(\frac{3k_r}{4\pi\xi^3}\right)\left(e^{-\frac{E_b}{k_B T}}\right)\frac{J_1\left(2\sqrt{-2b}\right)}{\sqrt{-2b}} \tag{36}$$

where

$$b = \frac{q^3 F(x)}{8\pi\varepsilon k_B^2 T^2} \tag{37}$$

E_b is the e-h binding energy, and J_1 is the Bessel function of the first kind. In disordered polymer-fullerene systems, the e-h pair distance, ξ, is not constant. Accordingly, the overall dissociation probability of e-h pairs must be treated statistically by integrating the probability function in Eq. (35) over all spatial e-h pair distances (ξ=0, ∞) as

$$P[a, F(x), T] = \int_{\xi=0}^{\xi=\infty} p[\xi, F(x), T]\, \frac{4\xi^2}{\sqrt{\pi}a^3}\, e^{-(\xi/a)^2}\, d\xi \tag{38}$$

where a Gaussian function normalized to the most probable distance a is used to represent a selected distribution profile.

Using the Poisson equation, potential $\psi(x)$ and electric field are calculated at the position x as

$$\varepsilon\frac{\partial^2\psi(x)}{\partial x^2} = -\varepsilon\frac{\partial F(x)}{\partial x} = q[n(x) - p(x)] \tag{39}$$

where ε is the dielectric constant of organic blend, q is the elementary charge, and $n(x)$ and $p(x)$ are the electron and hole densities, respectively. The current densities in terms of drift-diffusion of the charge carriers are calculated using the continuity equations for the electron $[J_n(x)]$ and hole $[J_p(x)]$ current densities

$$q\frac{\partial J_n(x)}{\partial x} + U(x) = 0 \tag{40}$$

$$-q\frac{\partial J_p(x)}{\partial x} + U(x) = 0 \tag{41}$$

$$J_n(x) = -q\mu_n\left[n(x)\frac{\partial\psi(x)}{\partial x} - V_t\frac{\partial n(x)}{\partial x}\right] \tag{42}$$

$$J_p(x) = -q\mu_{pn}\left[p(x)\frac{\partial\psi(x)}{\partial x} + V_t\frac{\partial p(x)}{\partial x}\right] \tag{43}$$

where μ_n and μ_p are the mobilities of the electrons and holes, respectively, and $V_t = k_B T/q$ is the thermal voltage. The coupled nonlinear equations described above are solved iteratively to obtain the steady state condition for the electric potential, free-charge concentrations, and current densities.

ORGANIC / METAL OXIDE INTERFACES

Based on new insights and increased understanding of organic materials, device concepts and organic physics, the quality and performance of organic solar cells (OSC) continue to evolve at a rapid pace [65,66,67]. Still, the energy conversion efficiencies needed to make OPVs viable commercially have yet to be realized. The highest power conversion efficiencies achieved to date remain at approximately 5~6.5% [33,68] while inorganic devices have efficiencies exceeding 15%. There are several reasons why organic solar cell performance levels are still lacking and, ironically, many relate to the

inherently poor electrical characteristics found with the organic polymers used in device fabrication [69, 70, 71, 72]. Higher exciton binding energies ranging from 0.2~0.5 meV, charge carrier mobilities less than 10^{-2} cm^2 V^{-1} s^{-1}, and extremely short exciton diffusion lengths between 5-20 nm are obstacles that must be overcome if OSCs are to be made practically and commercially viable [73, 74, 75, 76, 77].

In recent years, much has been learned regarding the mechanics behind charge transport between organic donor polymers/acceptor fullerenes that are mixed together in a BHJ configuration [65, 66, 67]. The close proximity and large mutual interfacial areas of the nanoscale constituents promote efficient dissociation of excitons approaching 100% [78]. However, this excellent *internal quantum efficiency* (IQE) is not the only driving force behind attaining high power conversion efficiencies. The charge carriers resulting from dissociated excitons must be efficiently collected at the device electrodes in order to be useful in the form of electricity. A number of factors impede this process including high electrical resistance at the electrode interfaces, and geminate and bimolecular recombination at the polymer/fullerene interfaces and within the bulk of the active layer, respectively.

A relatively new approach to alleviating the aforementioned technical problems involves the inclusion of n- and p-type metal oxide semiconductors in device fabrication. These materials can be used in several ways to improve charge carrier conduction to both the anode and cathode electrodes in an OSC. Metal oxides have been used as electron/hole blocking layers (EBL/HBL), as transport layers, and even as "optical spacers" between electrodes/active layers where they can improve absorption and ultimately increase short circuit current densities (J_{sc}), fill factors (FF), and ultimately,

power conversion efficiencies. The concept of implementing so-called *hybrid* organic-inorganic solar cells is gaining widespread interest, but the technical challenges in doing so are still many. For example, metal oxides and organic materials have dielectric constants that differ greatly and this could lead to a build-up of charge carriers at the interfaces [79]. This would impact device series (R_S) and parallel or *shunt* (R_{SH}) resistances that, in turn, have a direct influence on fill factor. *FF*, an important fundamental indicator of solar cell performance, is the ratio of the product of the current and voltage at maximum power to the product of the open circuit voltage and the short circuit current. It is desirable for FF to be high (i.e., greater than 0.6). Correspondingly, R_S should be as low as possible while R_{SH} would ideally approach infinity. The interrelationships between R_S, R_{SH}, current density, bias voltage, and *FF* are depicted in Figure 28.

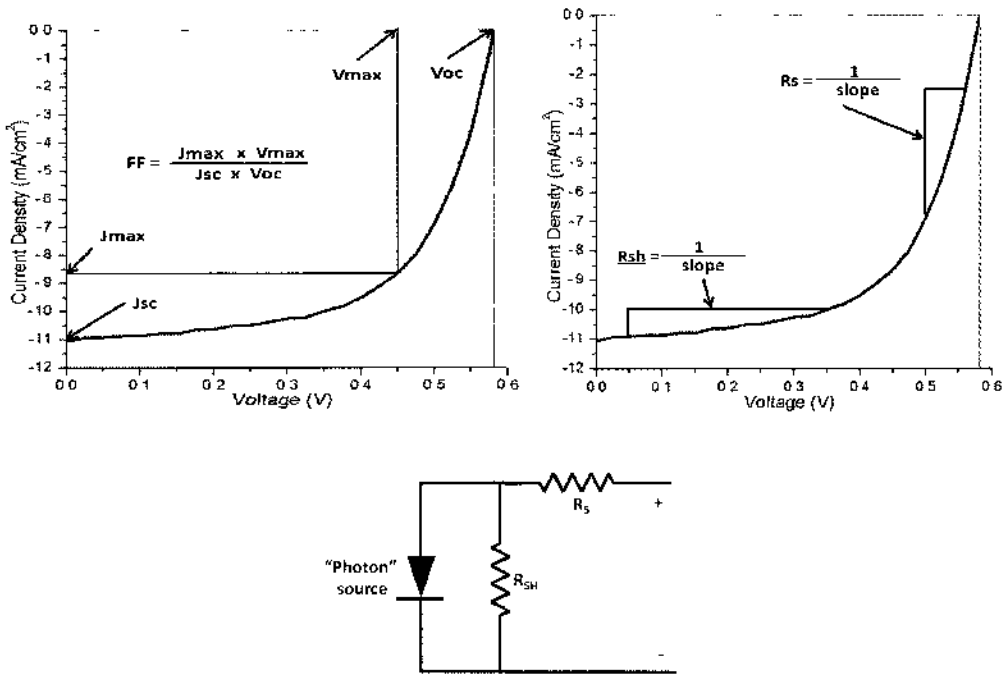

Figure 28. (a) FF, (b) series and parallel resistances, and (c) schematic of a solar cell. [80].

Figure 28 (a) shows the variables that determine fill factor in a solar cell. J_{max} and V_{max} are the current density and voltage bias measured at the maximum value (knee of the curve) of the J-V graph, respectively. J_{SC} and V_{OC} represent the short circuit current density and open circuit voltage, respectively. As previously described, it is the ratio of the product of J_{max} and V_{max} to the product of J_{sc} and V_{oc} that defines FF. Figure 28 (b) shows a schematic representation of a solar cell. Ideally, R_S would approach a value of zero ohms while R_{SH} would be infinite. The photodiode represents the organic active layer which is the source of the charge carriers. In the fourth quadrant of the J-V curves shown in Figure 28 (c) and (d), the inverse slope taken at the areas of the curves shown gives the values for R_S and R_{SH}. The series resistance is also impacted by such factors as the morphology, intrinsic resistance, and thickness of the organic active layer while shunt resistance is subject to the effects of the type and degree of active layer defects and impurities that cause carrier recombination and leakage current [80].

It has long been known that surface modification of the transparent conducting electrode (typically indium tin oxide (ITO)) can improve OSC performance. However, despite being optically transparent and having high conductivity, ITO also has a low work function that must be overcome since a high work function anode is necessary to decrease series resistance [81, 82]. The most commonly-used material to address this problem is PEDOT:PSS. It serves as a hole-transporter between the organic active layer and the ITO anode [83]. Still, PEDOT:PSS has some undesirable characteristics that make it less than ideal for this purpose, including susceptibility to thermal degradation and a very low pH (~1) that makes it corrosive to the ITO electrode [83]. As an alternative, surface modification of ITO can also be achieved through the use of metal

oxides such as MoO_3 [27], V_2O_5 [28], NiO [29], and WO_3 [30]. Metal oxides offer a greater degree of controllability in that they can be used to "tune" the energy band alignment between the organic active layer and the oxide electrode material thereby minimizing charger transfer barriers across the interface [84]. The focus of this section is to briefly highlight the properties and implementation strategies used when including metal oxide semiconductors in OSCs. Several different oxides can be used (e.g., TiO_2, WO_3, MoO_3, V_2O_5, and NiO), but only TiO_x will be specifically addressed here.

Boucle, et al., described two approaches for incorporating TiO_2 in OSCs. In the first case, polymer is incorporated inside a rigid porous oxide structure, and in the second oxide nanoparticles and polymer are mixed together and deposited as a solution to form the active layer. In both scenarios, the basic charge transfer mechanism is as shown in Figure 29.

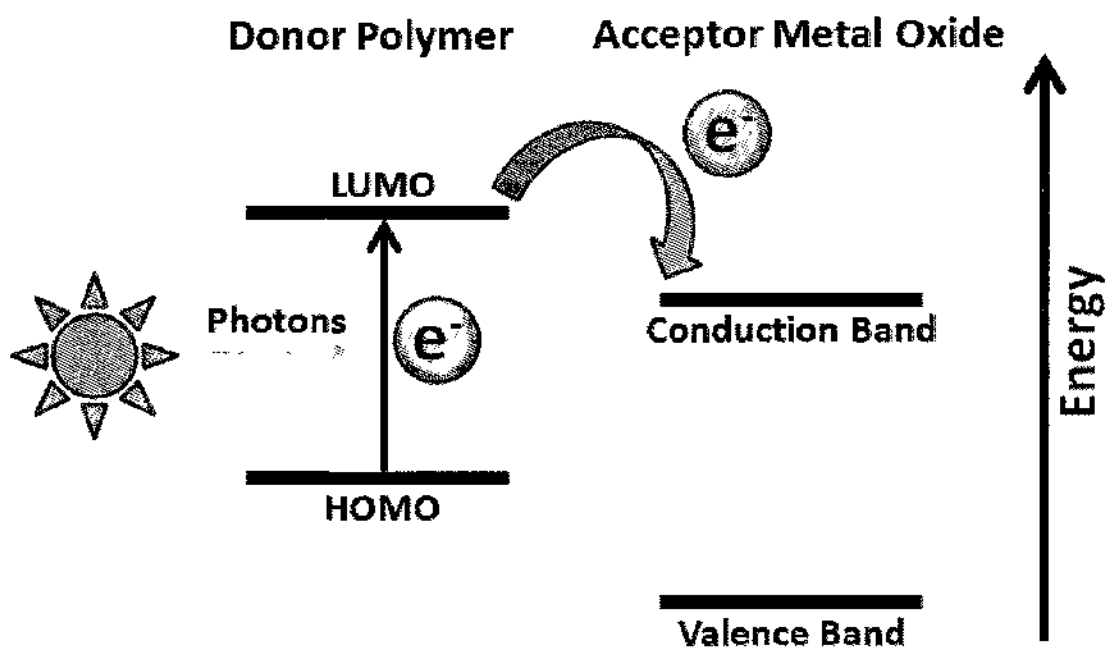

Figure 29. Basic charge transfer mechanism donor polymer to acceptor metal oxide [85].

Energy in the form of photons impinges on the donor polymer and produces excitons that diffuse to the polymer/metal oxide interface and dissociate into charge carriers. The metal oxide serves as an electron acceptor while the polymer transports the holes. Characteristics of the metal oxide acceptor include high electron mobility and affinity as well as mechanical and chemical stability [85]. There are three basic structures normally used in hybrid organic-inorganic cells (bilayer, porous, and blended) and two modes by which charges are transported to the electrodes. In bilayer and porous structures, charges move to the electrodes via diffusion while excitons that dissociate into charge carriers in blends require a difference in the work functions of the electrodes to provide a bias for transport.

Metal oxide semiconductors are of particular interest in these structures because their morphologies can be controlled accurately using wet chemical synthesis [86].

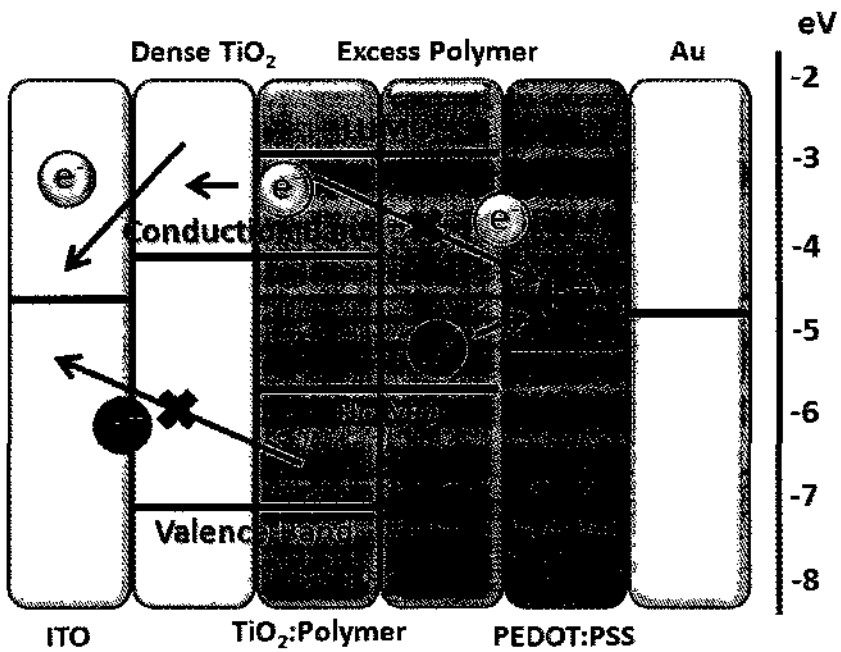

Figure 30. Energy level diagram of TiO_x-incorporated hybrid OSC [85].

This allows the oxides to be fabricated having variable densities. In addition, other desirable characteristics of these materials include the capability for light-trapping, their low cost, and their lack of toxicity. Also, they have been extensively studied, so much is known about their properties. Figure 30 shows the energy level schematic of a hybrid inorganic/organic solar cell with TiO_2 incorporated between the active layer and the ITO electrode. It's important to note that ITO can be used as either a hole-, or electron-collecting layer. This is due to its work function (4.5 to 4.7 eV) being between the HOMO and LUMO values of the organic layer. The dense TiO_2 layer serves as both an electron-acceptor and a *hole-blocking layer*. This is key to improving cell performance since organic donor material that is in direct contact with the ITO will result in leakage current that decreases device fill factor. However, a known issue with nanocrystalline TiO_2 is charge trapping that limits carrier transport. Note also that PEDOT:PSS is used between the polymer donor and the anode electrode. This layer serves as a hole acceptor and an *electron blocking layer*.

A novel use of TiO_x is as an *optical spacer* that increases efficiency in organic solar cells. Figure 31 shows schematic representations of both a conventional cell and a device incorporating an optical spacer.

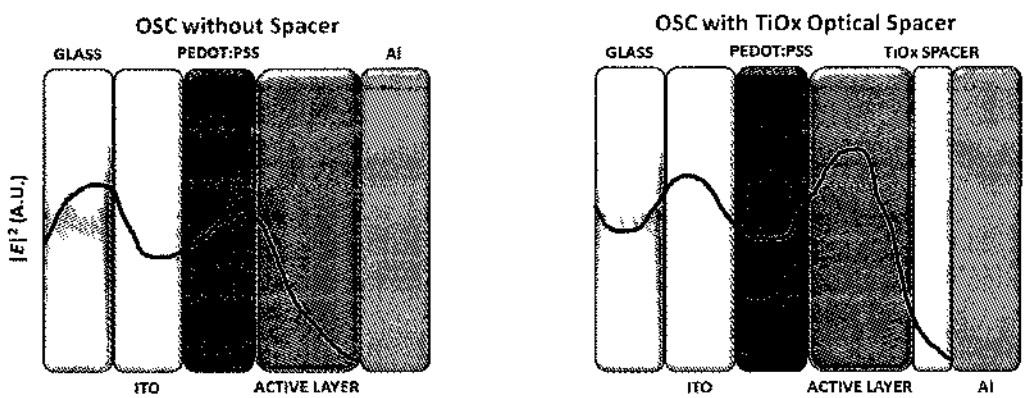

Figure 31. Conventional cell and a device incorporating an optical spacer [87].

Of note is that, in the device with the spacer, the magnitude of the irradiance is greater at every location throughout the entire thickness of the active layer compared to the conventional solar cell. This spatial redistribution of the irradiance will result in increased current density that subsequently improves energy conversion efficiency. The spacer must be optically transparent, a good electron acceptor/transporter with a conduction band edge lower than the LUMO of the acceptor. The LUMO must be above or near the Fermi level of the metal electrode (Al) [87]. Figure 32 shows a schematic representation of the energy levels for the device with the optical spacer.

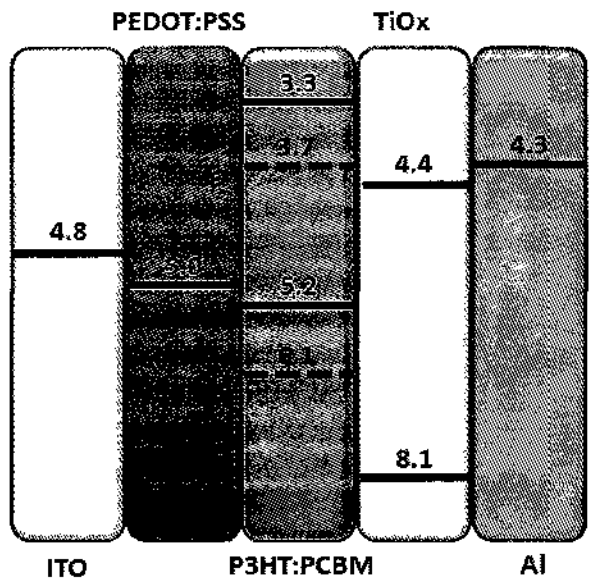

Figure 32. Energy levels for a device with an optical spacer [87].

In contrast, conventional devices show the highest optical field amplitude close to the anode and a considerable portion of the active layer is not used for photogeneration of charges. This condition results in greater exciton generation and dissociation at this depth and leads to excess charge build up.

Incorporating metal oxides in OSC structures improves performance via a number of mechanisms including minimizing charge carrier recombination, preventing excitons from coming into contact with the electrodes, and "tuning" the effective work function of the electrodes. They are also showing promise as optical spacers. These materials show a number of characteristics that make them more attractive than PEDOT:PSS including physical and chemical stability, resistance to thermal degradation, good transport capability, non-toxicity, and ease of processing. Thermal annealing is not necessary during the fabrication process and many of the oxides can be solution-processed. Additionally, metal oxides can serve as protective barriers for the electrodes, increase shunt resistance, and prevent leakage current. While there are still obstacles to facile fabrication of the more complicated nanostructured OSC devices, oxides will likely become a very commonly used material for organic solar cell fabrication in the future.

Critical to making rapid progress in the development of OSC technology will certainly be the use of computer modeling and simulation. It is with the lessons learned about the topics in this chapter that our simulation algorithms were written. The results from those simulations are presented in Chapter 3.

CHAPTER III

COMPUTER SIMULATION AND RESULTS

OVERVIEW OF SIMULATIONS CONDUCTED

Modeling of OSC and LED performance is a very active area of research. While numerous characteristics are the focus of study, perhaps the most often explored include current-voltage properties, electron and hole transport, absorption, ideal active layer thickness, recombination, and energy conversion efficiency. The goal, however, is always the same; to determine how to maximize solar cell performance and efficiency. In this study, a series of simulation experiments were conducted with these goals as the focus.

In the first experiment, P3HT:$PC_{61}BM$ and P3HT:$PC_{71}BM$ planar OSC devices were simulated to determine ideal active layer thicknesses. After varying such factors as active layer thickness, electron and hole mobilities, and the Langevin recombination efficiency, the results indicated that optimizing device efficiency is strongly dependent on the simultaneous control of active layer thickness and charge carrier mobilities.

In the second analysis, device design parameters for planar OSCs made from low-bandgap polymer blends of poly[2,6-(4,4-bis-(2-ethylhexyl)-4H-cyclopenta[2,1-b;3,4-b']dithiophene)-alt-4,7-(2,1,3-benzothiadiazole)]: phenyl-C_{61}/C_{71}-butyric acid methyl ester (PCPDTBT:$PC_{61}BM$ and PCPDTBT:$PC_{71}BM$) were investigated. Interrelationships between absorption, fill factor, energy conversion efficiency, and current density were simulated and again, the results indicated that optimizing device efficiency strongly depends on active layer thickness and carrier mobilities. More specifically, efficiencies

reach peak values when charge carrier transport is balanced. Additionally, PCPDTBT:$PC_{71}BM$ showed higher efficiencies compared to PCPDTBT:$PC_{61}BM$.

The third experiment involved combining knowledge gained from the first two and extending the exploration to the simulation of tandem cells – individual planar cells stacked together and connected in series electrically. Each tandem structure was composed of two subcells of varying combinations of low- and high-bandgap donors and acceptor fullerenes. One subcell containing PCPDTBT was combined with either $PC_{61}BM$ or $PC_{71}BM$. A second subcell was made of P3HT and $PC_{61}BM$ or $PC_{71}BM$ components. The mutual effects of both subcells in tandem were analyzed to determine such parameters as current density, open circuit voltage, fill factor, and power conversion efficiency. Our results indicate that appropriate spatial ordering of the subcells is critical to achieving efficiencies that far exceed those of single planar OSCs.

The fourth study focused on a particular tandem configuration; PCPDTBT:$PC_{61}BM$ as the bottom cell and P3HT:$PC_{71}BM$ as the top. Again, the effects of photon density, absorption, balanced and unbalanced charge carrier transport, and bimolecular recombination in the two subcells were incorporated into the simulations. As observed in previous experiments, maximum energy conversion efficiency is achieved when charge carrier mobilities in both top and bottom cells are balanced. However, the efficiency drops significantly if the carrier mobilities are unbalanced in *either* the top or bottom cell. Adding a further level of complexity, unbalanced carrier mobilities in the top cell require a reduction in the thickness of the bottom cell whereas unbalanced bottom cell mobilities require an increase in the thickness of the bottom cell to compensate for

the reduced current. More in-depth explanation of each of the four experiments follows in the remainder of this chapter.

OPTICAL SIMULATION: OPTIMIZING ACTIVE LAYER THICKNESS

Considerable data in the literature describes the significance of active layer thickness and its impact on the efficiency of bulk-heterojunction organic solar cells [88,89,90,91]. However, some incongruity exists regarding the optimal thickness required to achieve maximum energy conversion efficiency [88,89,90]. For example, Li *et al.*, found that energy conversion efficiency and short circuit current density of P3HT and $PC_{61}BM$ peaked at a layer thickness of 63 nm [88]. However, other researchers have tested similarly constructed devices and found that in some cases efficiency actually showed near-constant efficiencies over a wide thickness range (50 – 400 nm) [89,91]. In addition to the optimal thickness, current research shows promising results with P3HT:$PC_{71}BM$ devices yielding higher absorption and increased power conversion efficiencies compared to P3HT:$PC_{61}BM$-based solar cells [92]. Indeed, P3HT:$PC_{71}BM$ shows greater absorption across a broader range of the visible spectrum due to the asymmetric structure of C_{71} fullerene that improves its optical properties [68,93]. Therefore, device efficiency of $PC_{71}BM$-based organics compared to their $PC_{61}BM$-based counterparts is shown to increase while the comparison of device performance between P3HT:$PC_{61}BM$ and P3HT:$PC_{71}BM$ *solar cells* is not well investigated.

This particular experiment employed a commercially available thin film optical simulation tool (Setfos3) that implements the transfer matrix method (TMM) and organic semiconductor drift-diffusion modules in layered thin-film OPVs [94]. The layer sequence for the devices followed a standard configuration; indium tin oxide (ITO) (120

nm) / poly(3,4-ethylenedioxythiophene):poly(styrene sulfonate) (PEDOT:PSS) (50 nm) / P3HT:PCBM (variable) / aluminum (100 nm). Optical calculations were conducted over a wavelength range from 350 to 1000 nm and the real and imaginary parts of the complex refractive indexes for the P3HT:$PC_{61}BM$ and P3HT:$PC_{71}BM$ blends were obtained from Ref. [35]. Molecular orbital energy levels (HOMO and LUMO) for the P3HT:PCBM layers were set to values reported in the literature [95]. In pristine organic semiconductors, bimolecular free charge carrier recombination occurs and is described by the rate equation, $R = \eta np(\mu_n + \mu_p)q/\varepsilon$, where n and p are electron and hole densities, q is the elementary charge, and ε is the material dielectric constant [96,97]. η is the Langevin recombination coefficient and in this simulation is set to 0.1 to *weight* the rate equation. This is necessary to mimic realistic conditions found with polymer–fullerene blends [96,98].

Figure 33 shows simulated current densities for P3HT:$PC_{61}BM$ as a function of layer thickness along with experimental data from Li [88] and Moule *et al.*, [91] which showed energy conversion efficiencies over 4%. Three combinations of electron/hole mobilities are shown: 1) $\mu_e = \mu_h = 10^{-3}$ cm^2 V^{-1} s^{-1}, 2) $\mu_e = 10\mu_h$, and 3) $\mu_e = 100\mu_h$. At a thickness range of about 80 – 100 nm, the current densities for each are relatively close in value. The oscillations in the current density can be attributed to variations in carrier generation rate inside the active layer where interference occurs by the opaque electrode [88]. However, distinctly different current densities have been observed that depend upon carrier mobilities and increased thickness. For the carrier mobility where $\mu_e = \mu_h = 10^{-3}$ cm^2 V^{-1} s^{-1}, the current densities keep increasing with increased device thickness while the decline of the current densities dominates when the hole mobilities drop by one

or two orders of magnitude compared to that of the electron. Furthermore, the close correlation between simulated and experimental data from Li [88] and Moule *et al.*, [91] indicates the validity of the simulation model.

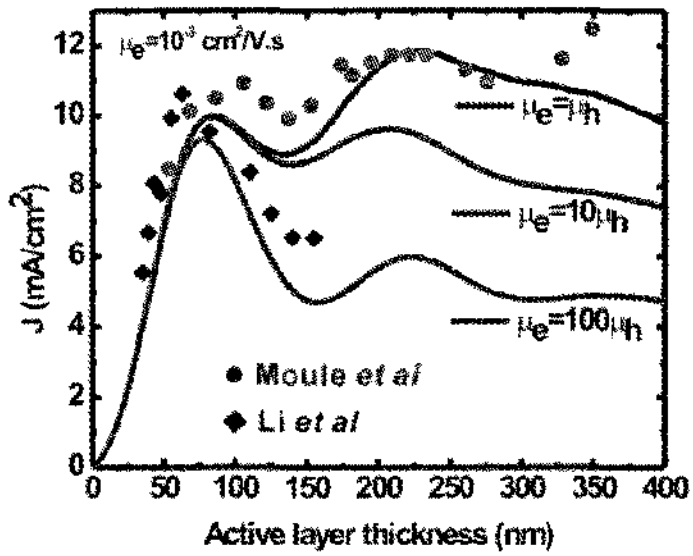

Figure 33. Simulated current densities for P3HT:$PC_{61}BM$ as a function of layer thickness [88,91].

As can be seen in Figure 34, manipulation of the active layer thickness has a marked impact on short circuit current density (J_{SC}) and, to a lesser extent, on open circuit voltage (V_{OC}), and subsequently either increases or decreases the fill factor (FF) and efficiency. When carrier mobilities in P3HT:$PC_{61}BM$ simulations are equal to $\mu_e = \mu_h = 10^{-3}$ cm^2 V^{-1} s^{-1}, V_{OC} remains virtually constant while the fill factor trends almost linearly downward from a maximum of 0.65. This decline in FF is attributable to the increase in device resistance that results from increased layer thickness. Current density declines from the maximum over a short thickness range, but then once again increases

significantly. This increase in current density and corresponding decline in *FF* causes the efficiency to remain essentially constant across the expanse of the active layer.

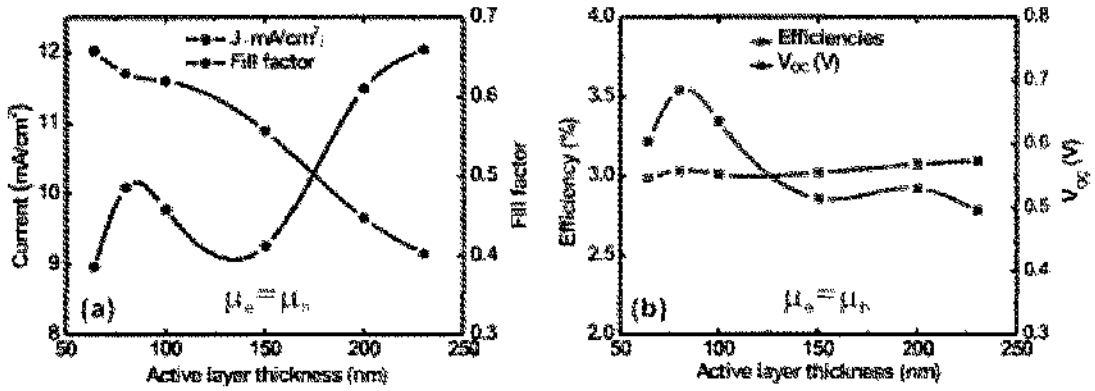

Figure 34. J_{SC}, *FF*, η, and V_{OC} vs. active layer thickness for equal carrier mobilities.

A maximum efficiency of ~3.5% was observed with an active layer thickness between 80 and 100 nm. When the magnitude of the hole mobility is decreased by a factor of 10 ($\mu_e = 10\mu_h = 10^{-3}$ cm^2 V^{-1} s^{-1}), effects on *FF*, efficiency, and current density are pronounced, as shown in Figure 35.

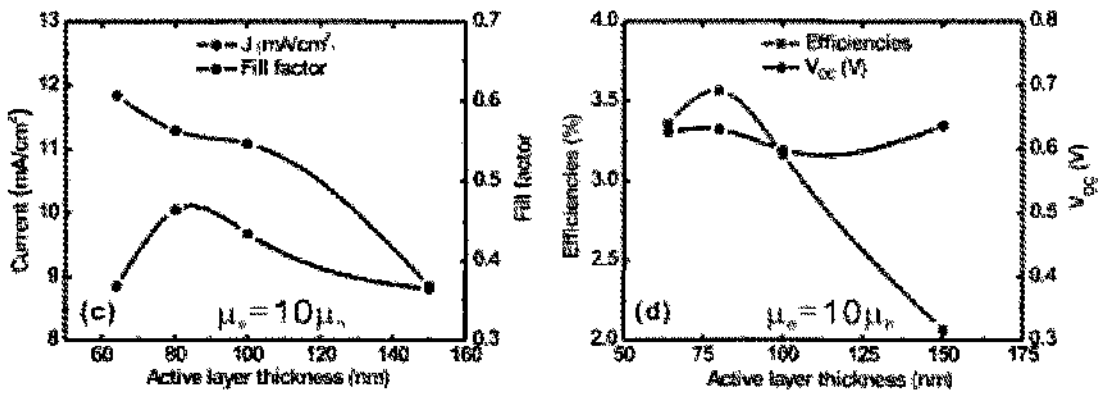

Figure 35. J_{SC}, *FF*, η, and V_{OC} vs. active layer thickness with decreased hole mobility ($\mu_e = 10\mu_h = 10^{-3}$ cm^2 V^{-1} s^{-1}).

The maxima seen with equal mobility combinations remain, but the subsequent declines with increasing thickness are much faster and no secondary increase in current density is observed. Because both *FF* and J_{SC} decrease simultaneously, efficiency no longer remains constant but rather falls off more rapidly.

Figures 36(a) and 36(b) show values for efficiency as a function of active layer thickness for two sets of electron/hole mobility combinations in P3HT:$PC_{61}BM$.

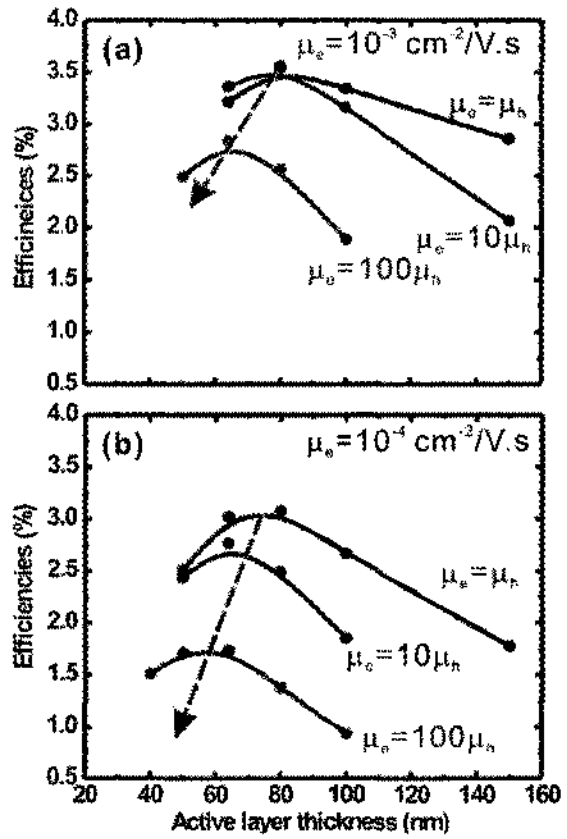

Figure 36. Efficiency as a function of active layer thickness for two electron/hole mobility combinations (a) ($\mu_e = 10\mu_h = 10^{-3}$ cm^2 V^{-1} s^{-1}) and ($\mu_e = 10\mu_h = 10^{-4}$ cm^2 V^{-1} s^{-1}) in P3HT:$PC_{61}BM$.

It is clear that a strong dependence between carrier mobilities, layer thickness, and efficiency exists. The highest efficiencies are found when carrier mobility for both electrons and holes is the same—even if the *magnitude* of the mobilities is different. As the electron/hole mobility ratios change and become greater, there is a corresponding decrease in both efficiency and optimal layer thickness. The effects are most apparent when there is at least a two-orders-of-magnitude difference between the electron and hole mobilities. The optimal active layer thickness shifts from ~80 nm with $\mu_e = \mu_h$ to ~60 nm when $\mu_e = 100\mu_h = 10^{-3}$ cm^2 V^{-1} s^{-1}. In Figure 36 (b), when electron mobility is dropped to 10^{-4} cm^2 V^{-1} s^{-1}, overall efficiency declines below 3% in each case from that observed with $\mu_e = 10^{-3}$ where the maximum efficiencies were ~3.5%. In both figures, the largest decline in efficiency occurs with a two-order-of-magnitude difference in carrier mobilities. This is primarily due to carrier recombination and, at these lower mobilities, to space charge limited current effects (SCLC) [90]. SCLC becomes prominent when hole mobility differs from that of the electrons by two orders of magnitude or more [97] leading to unbalanced distribution of charge carriers across the active layer. Therefore, the effects of SCLC significantly influence fill factor and cause the decline in current density, thereby resulting in a drastic reduction of efficiency.

The simulation model did not include algorithms to account for the various morphologies of organic blends that are known to affect electrical and optical properties. Optimal morphologies of P3HT:PCBM organic blends have been reported in the literature to be achievable with a blend ratio of approximately 1 : 1 which leads to fine intermixing between donor and acceptor constituents [99]. However, research in our lab has shown that other ratios may be better. A ratio of 1:0.8 has proven to be the most

successful ratio for our work, but more importantly, increasing the actual *concentration* of donor/acceptor in a constant volume of solvent can markedly increase PCE. Morphology is strongly tied to blend ratios since it is necessary to avoid large scale sub-domains that lead to inefficient exciton dissociation and diminished charge collection and absorption efficiencies. For example, 1:2 compositions of P3HT:PCBM result in a coarser mixture while 1:4 compositions developed PCBM-rich, sub-micron scale domains [99]. Even though PCBM-rich domains resulting from higher PCBM concentrations improved charge collection efficiencies due to the relatively higher electron mobility of PCBM, it came with a performance cost. Diminished light absorption efficiencies and reduced interfacial surface area between P3HT:PCBM decreased the overall energy conversion efficiencies as compared to organic blends with morphologies developed with a blend ratio of 1:1 [99]. In the case of P3HT-rich morphologies, poor exciton dissociation degrades energy conversion efficiencies [99]. However, it is important to note that the data reported specifically refers to P3HT:PCBM blends. The situation for LBG polymers is quite different where donor:acceptor ratios are typically 1:3 or 1:4.

Figures 37 and 38 show simulated data for P3HT:$PC_{71}BM$ contrasted with P3HT:$PC_{61}BM$. Graphs of current density and efficiency as functions of active layer thickness show the potential for the performance of $PC_{71}BM$ to eclipse $PC_{61}BM$ due to its superior optical and electrical properties. Figure 37 shows the two different blends having equal charge carrier mobilities in each (i.e., $\mu_e = \mu_h = 10^{-3}$ cm^2 V^{-1} s^{-1}). Current densities when internal quantum efficiency (IQE) – a measure of the amount of *absorbed*

photons that are converted to electricity – is 100% are shown for both, with that for $PC_{71}BM$ being approximately 55% greater in the 80 –100 nm thickness range.

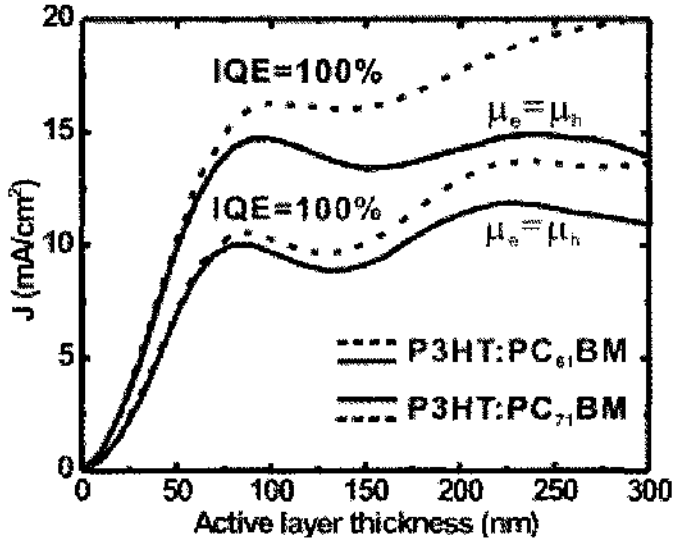

Figure 37. J_{SC} vs active layer for IQE = 100% (dotted lines) and P3HT:$PC_{61}BM$ and P3HT:$PC_{71}BM$ mobilities (solid lines) equal to $\mu_e = \mu_h = 10^{-3}$ cm^2 V^{-1} s^{-1}.

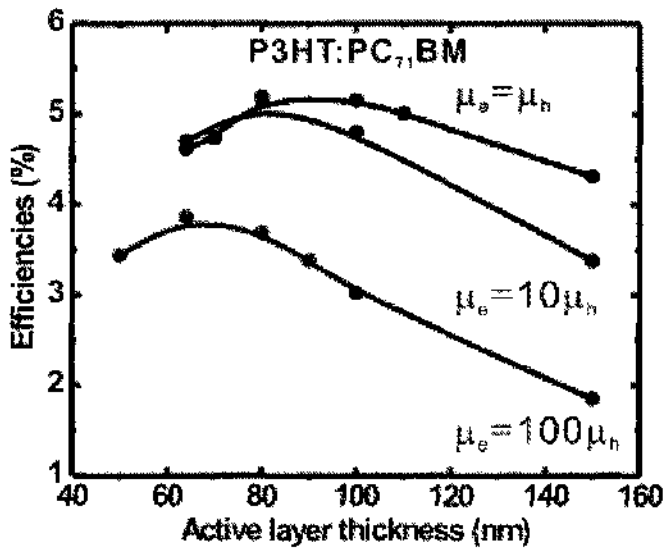

Figure 38. P3HT:$PC_{71}BM$ efficiency vs. active layer thickness for $\mu_e = \mu_h = 10^{-3}$ cm^2 V^{-1} s^{-1}, $\mu_e = 10\mu_h$, and $\mu_e = 100\mu_h$.

For an actual P3HT:$PC_{71}BM$ device produced in our lab, the current density was 35% greater than that for $PC_{61}BM$ [100]. Simulated efficiencies as a function of active layer thickness are much improved in P3HT:$PC_{71}BM$ with PCE showing more than 5% compared to 3.5% for P3HT:$PC_{61}BM$ (Figure 38). With a one-order-of-magnitude (μ_e=10μ_h) change in carrier mobility, efficiencies remain high with a slight downward shift in optimal thickness to about 80 nm. Even with an increase in thickness to 150 nm, efficiency only drops to 3.5% – still close to the efficiency of P3HT:$PC_{61}BM$ at its optimal active layer thickness for the same carrier mobilities (Figure 36(a)). Again, a two-order-of-magnitude difference in electron/hole mobility ratio produces a more significant decline in efficiency and reduction in optimal layer thickness due to recombination and SCLC.

In summary, optical simulation and modeling of P3HT:$PC_{71}BM$ planar cells shows the greatest potential for higher efficiencies at thicknesses around 100 nm compared to P3HT:$PC_{61}BM$ that shows its highest efficiency at approximately 80 nm. Optimum layer thickness is strongly dependent upon the magnitude and ratio of charge carrier mobilities and directly impacts the maximum efficiency that can be achieved.

OPTIMIZING LOW-BANDGAP PCPDTBT:PCBM SOLAR CELLS

Organic photovoltaics continue to be a promising alternative to conventional inorganic solar cells due to their low cost and ease of fabrication [90,101,102,103]. Currently, most research efforts are focused on devices made from P3HT-$PC_{61}BM$ and P3HT-$PC_{71}BM$ organic blends [68,87,93,104,105,106,107]. One of the critical characterization parameters for these devices is the open circuit voltage. The V_{OC}

observed in a conjugated polymer-PCBM-based solar cells is determined by the following relationship:

$$V_{OC} = \frac{1}{q}\left(|E^{Donor}(\mathrm{HOMO})| - |E^{PCBM}(\mathrm{LUMO})|\right) - V_{Loss} \quad (44)$$

where q is the elementary electronic charge, E^{Donor}(HOMO) is the highest occupied molecular orbital of the polymer and E^{PCBM}(LUMO) the lowest unoccupied molecular orbital of PCBM [3]. The empirical voltage loss (V_{Loss}) in P3HT:PCBM organic blends has been found to be about 0.3V [3]. As a result, the V_{OC} observed in actual devices ranges from 0.5 to 1V and must be improved further to increase overall efficiency [3]. The increase in V_{OC} can be achieved by controlling many factors such as the number of defects and traps as well as blend morphologies and the quality of the contact between layers [80,99,108]. Other approaches include the exploration of new conjugated polymers capable of increasing V_{OC}. However, increasing V_{OC} with new material systems requires control of offset energy levels since they can cause decreases in short circuit current density because of the drop in potential at heterojunction interfaces [109]. These drops lead to inefficient dissociation of excitons [109]. Recently, new insights into material parameter interrelationships in organic solar cells such as polymer HOMO/LUMO, PCBM LUMO levels, and the donor bandgap have highlighted potential means of controlling and predicting PCE [3,4]. Results of these studies show that device efficiency is dependent on the LUMO offset between donor and acceptor as well as donor energy bandgap. This indicates that the choice of the donor–acceptor couple is as important as the bandgap of the absorbing material. These studies also suggest that

considerable improvement in efficiency to values as high as 11% for single heterojunction solar cells could be realized with low bandgap (LBG) polymers having an energy gap around 1.5 eV and an ideal LUMO difference of 0.3 eV [3,4]. Such predictions of high efficiencies are based on the assumption that LBG polymer materials can achieve reasonable charge carrier mobilities and thereby produce acceptable *FF*.

As far as candidates for new, LBG, conjugated polymer materials, PCPDTBT is receiving a great deal of attention due to its ideal bandgap, excellent absorption, and charge carrier properties as compared to P3HT:PCBM [68,110,111]. It should be noted that this new organic material having an optical bandgap of Eg~1.5 eV can extend the spectral absorption profile into the infrared region [68,110,111]. In addition, based on a model presented by Scharber *et al.*, the energy conversion efficiencies of PCPDTBT:$PC_{61}BM$ devices could reach 7.7% [3,4]. However, this model does not include a detailed treatment of the effects of several device parameters including photoactive layer thickness, absorption efficiencies, and charge carrier transport. This is significant because varying active layer thickness has a direct bearing on spectral absorption, and its influence on energy conversion efficiency is not so straightforward. Several factors are associated with, and impacted by, changes in active layer thickness including open circuit voltage, short circuit current density, and fill factor – all are key factors determining PCE [88,89,90,91]. While considerable efforts have been devoted to the design of device parameters for P3HT:PCBM and other high-bandgap organic blends, systematic studies on the design of LBG blends of PCPDTBT:PCBM are still relatively few [3,4,112]. In this experiment, the design of PCPDTBT:$PC_{61}BM$ and PCPDTBT:$PC_{71}BM$-based solar cells was investigated. The electron-accepting

components, $PC_{61}BM$ and $PC_{71}BM$, possess chemical and structural differences and their respective impact on device performance was assessed. C_{70} fullerene has an asymmetric structure and improved optical properties compared to those of C_{60} [93], but the potential efficiency limits of PCPDTBT:$PC_{61}BM$ and PCPDTBT:$C7_1BM$ solar cells have yet to be determined. Charge carrier transport in PCPDTBT:PCBM is strongly influenced by the polymer/fullerene composition where the mobility of both charge carriers can be balanced to $10^{-3} - 10^{-4}$ $cm^2 V^{-1} s^{-1}$ with the proper blend ratio [111]. For example, Peet, *et al.*, [68] performed optimization on PCPDTBT:$PC_{71}BM$ devices and found that the highest efficiencies obtained ranged from 5.2 to 5.8% when using polymer/fullerene ratios between 1:2 and 1:3. Other researchers have shown that a 1:3 ratio yielded the highest current densities and the greatest number of long-lived charge carriers [113,114,112]. Therefore, since index values for other blend ratios were either unavailable or incomplete, optical simulations performed in this experiment used complex indices of refraction for both polymer/fullerene blends based on a PCPDTBT:PCBM ratio of 1:3 (by weight). The index values were determined via spectrometric ellipsometry (SE) [35]. However, additional analyses can be readily performed when index values for other blends become available. For the given blend ratio, the impact of charge transport on device function in PCPDTBT:PCBM solar cells was investigated with the goal of identifying an optimal design for maximized performance.

Optical simulations employing TMM were used to assess absorption characteristics [115,116,117] – reflectivity, transmission, absorption, and photonic flux density – and numerical models were applied to assess the electrical properties [118]:

drift, diffusion, mobility and recombination characteristics. The default illumination intensity (*irradiance*), $I_{\mathrm{AM\,1.5}}$, for all simulations performed was 100 mW cm^{-2} referenced to the unpolarized solar spectrum. Absorption in the device is described by the *photon absorption rate profile*, G(z), and is given by:

$$G(z) = \int_{\lambda} \frac{\alpha(\lambda) I_{\mathrm{AM1.5}}(z,\lambda)}{h\nu} \, \mathrm{d}\lambda (\mathrm{m}^{-2}\,\mathrm{nm}^{-1}\,\mathrm{s}^{-1}) \tag{45}$$

The variable z represents the position inside the solar cell when traversing distance perpendicularly through the individual device layers, $\alpha(\lambda)$ is the absorption coefficient as a function of wavelength, and $h\nu$ is the energy of the photons. Furthermore, device performance is simulated based on the standard drift-diffusion equation augmented by the exciton continuity equation, Langevin recombination, Onsager–Braun exciton dissociation, carrier transport, and carrier mobilities [64,119,120]. As before, morphology-dependent distribution and disorder of the energy levels and the effect of donor–acceptor interfaces is not considered in this model. However, detailed studies employing extensive dynamical Monte Carlo modeling of organic solar cells can be found that describe the dependence of charge transport properties on blend morphologies [121].

The device configuration implemented was the standard planar layered structure; ITO(120.0nm) / PEDOT:PSS(50.0nm) / PCPDTBT-PC_{61}/C_{71}BM (variable) / aluminum(100.0nm). To accurately calculate optical interference effects reflecting realistic conditions within the device, complex indices of refraction from Ref. [35] were

used over the wavelength range from 350 to 1000 nm. The indices for ITO, Al, and PEDOT:PSS were determined experimentally using spectrometric ellipsometry.

As explained previously, in pristine organic semiconductors, bimolecular free charge carrier recombination occurs and is described by the Langevin recombination rate equation, $R = \eta np(\mu_n+\mu_p)q/\varepsilon$ [96,97]. This rate is dependent on the sum of the individual carrier mobilities, μ_n and μ_p. The Langevin recombination parameter (η) has a value of one in inorganic semiconductors, but a scaling factor for the rate equation must be included for organic semi-conductors. Charge carriers in polymer-fullerene organic photoactive layers are confined to separate donor/acceptor phases where dissociation and recombination occurs. So, the standard recombination rate equation must be altered to reflect the actual physics by changing the value of η. This effectively *weights* the rate equation in order to mimic realistic conditions found with polymer-fullerene blends. Even though the Langevin recombination parameter for PCPDTBT:PCBM is not known with certainty, a value of 0.1 is used as this is known to be realistic and applicable to actual P3HT:PCBM blends [96,98,106]. The expectation is that the recombination physics for P3HT:PCBM and PCPDTBT:PCBM blends will be similar.

Simulated absorption data for PCPDTBT:PC_{71}BM and PCPDTBT:PC_{61}BM are shown in Figure 39 along with experimentally measured results for the same blends as reported by Muhlbacher, *et al.* [112]. A comparison of PCPDTBT:PC_{61}BM experimental and simulated data shows that they have similar profiles with decreases in absorption in the 500–600 nm range and increases between 650 and 800 nm.

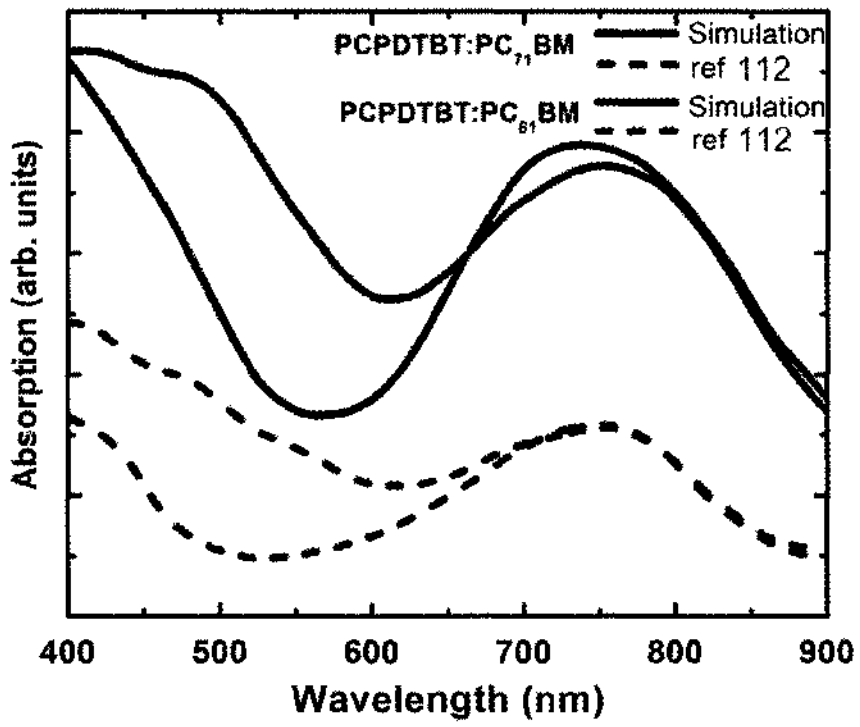

Figure 39. Simulated and experimental absorption data for PCPDTBT:$PC_{71}BM$ and PCPDTBT:$PC_{61}BM$.

The increased spectral absorption at longer wavelengths is due to the PCPDTBT component. Comparable similarities of the absorption profiles for PCPDTBT:$PC_{71}BM$ are also readily apparent with decreased absorption between 550 and 650 nm and broad peaks occurring in the 675–825 nm range. As with PCPDTBT:$PC_{61}BM$, the additional spectral absorption in the PCPDTBT:$PC_{71}BM$ composite results from PCPDTBT. However, the amount of absorption is markedly increased in the 400–650 nm range as compared to PCPDTBT:$PC_{61}BM$. This is attributed to the asymmetric structural feature of $PC_{71}BM$ [68,93] and is clearly demonstrated in both simulated and experimental results. Therefore, the close correlation between simulated and measured data indicates the validity of the model used.

Simulated current density values for PCPDTBT:PC_{71}BM and PCPDTBT:PC_{61}BM as a function of active layer thickness are shown in Figure 40. For both blends, the highest values for current density are obtained when electron and hole mobilities are balanced at $\mu_e = \mu_h = 10^{-3}$ cm^2 V^{-1} s^{-1}. Initial peak values for both composites occur at about 100 and 118 nm for PCPDTBT:PC_{71}BM and PCPDTBT:PC_{61}BM, respectively.

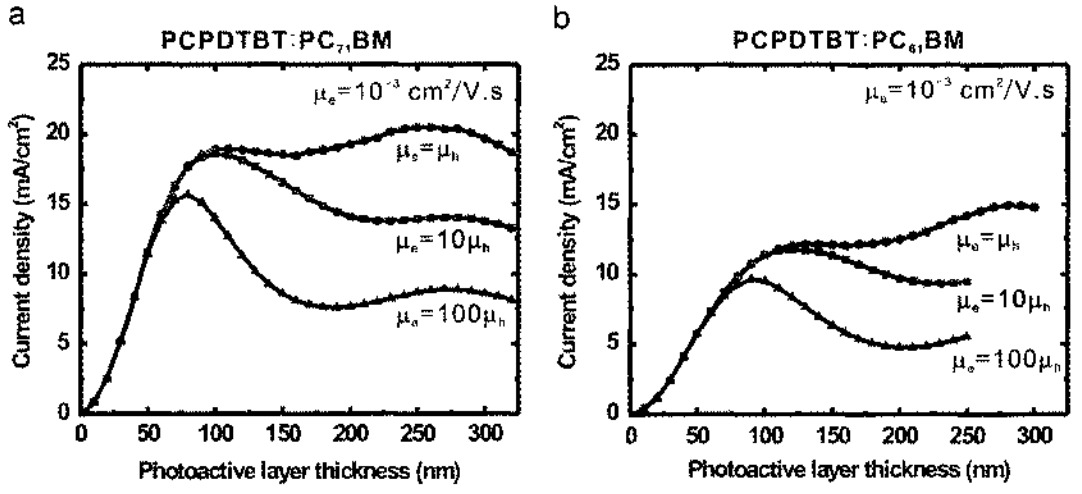

Figure 40. Current density as a function of active layer thickness for three combinations of electron/hole mobilities ($\mu_e = \mu_h = 10^{-3}$ cm^2 V^{-1} s^{-1}, $\mu_e = 10\mu_h$, and $\mu_e = 100\mu_h$) in (a) PCPDTBT:PC_{71}BM and (b) PCPDTBT:PC_{61}BM.

However, with increased thickness, secondary peaks of greater value for PCPDTBT:PC_{71}BM and PCPDTBT-PC_{61}BM occur at 250 and 275 nm. The oscillations in the current density can be attributed to variations in carrier generation rate inside the active layer where interference occurs by the opaque electrode [88]. Distinctly different current density behavior is observed when electron/hole mobility ratios are not balanced. As can be seen in Figure 40, when $\mu_e = 10\mu_h = 10^{-3}$ cm^2 V^{-1} s^{-1}, and $\mu_e = 100\mu_h = 10^{-3}$ cm^2

V^{-1} s-1, peak current densities begin to decline and correspondingly shift to progressively shorter thickness values. This indicates that current density depends upon both carrier mobilities and layer thickness. For the carrier mobility where $\mu_e = \mu_h = 10^{-3}$ cm^2 V^{-1} s^{-1}, the current densities continue increasing with greater device thickness while a decline dominates when the hole mobilities drop by one or two orders of magnitude compared to that of the electron. It is also noted that for all ratios of electron/hole mobility, PCPDTBT:PC_{71}BM devices show higher current densities than those observed with PCPDTBT:PC_{61}BM. The percentage increases in current density for PCPDTBT:PC_{71}BM over PCPDTBT:PC_{61}BM at $\mu_e = \mu_h = 10^{-3}$ cm^2 V^{-1} s^{-1}, $\mu_e = 10\mu_h$, and $\mu_e = 100\mu_h$, are approximately 54%, 56%, and 63%, respectively.

Figure 41 shows that manipulation of the active layer thickness has a marked impact on J_{SC} and, to a lesser extent, on V_{OC} and subsequently either increases or decreases the fill factor and efficiency. In PCPDTBT:PC_{71}BM simulations with hole and electron mobilities set equal to each other (10^{-3} cm^2 V^{-1} s^{-1}), *FF*s are calculated over a range of thicknesses based on V_{OC}, J_{SC}, V_{max}, and I_{max} values. Open circuit voltage remains virtually constant while the fill factor trends almost linearly downward from a maximum of 0.65 as seen in Figure 41 (a and b). This decline in *FF* is attributable to the increase in device resistance that results from increased layer thickness. Current density declines slightly from the maximum at about 100 nm over a short thickness range from 100 to 160 nm, but then once again increases significantly. This increase in current density and corresponding decline in fill factor causes the efficiency to decline across the expanse of the active layer albeit at a relatively slow rate compared to device layers having non-equal charge carrier mobility ratios.

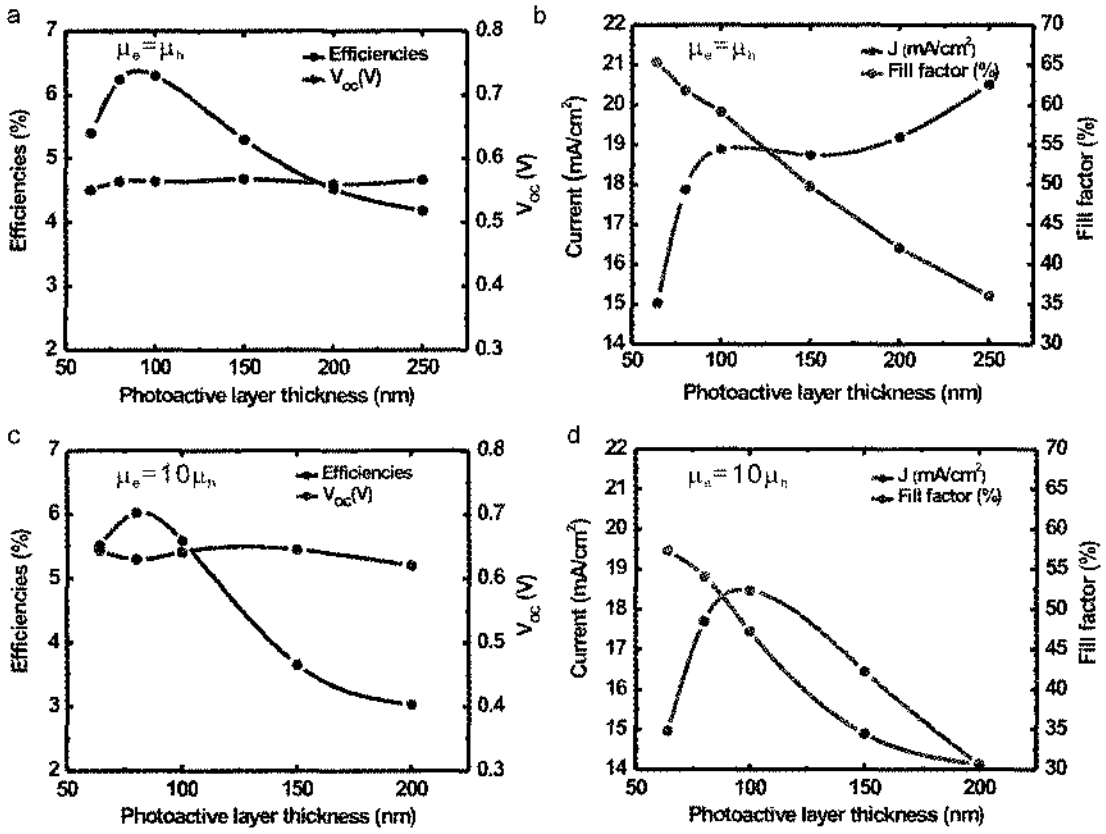

Figure 41. Electrical characteristics for PCPDTBT:$PC_{71}BM$ simulations: (a) efficiency and V_{OC} vs. active layer thickness, (b) J_{SC} and FF vs. active layer thickness for $\mu_e = \mu_h = 10^{-3}$ cm^2 V^{-1} s^{-1}, (c) efficiency and V_{OC} vs. active layer thickness, and (d) J_{SC} and FF vs. active layer thickness for $\mu_e = 10\mu_h = 10^{-3}$ cm^2 V^{-1} s^{-1}.

In this simulation, a maximum efficiency of ~6.5% was observed with an active layer thickness of 90 nm while efficiency slowly deteriorated with increased thickness. When the magnitude of the hole mobility is decreased by a factor of 10 (i.e., μ_e=10μ_h=10^{-3} cm^2 V^{-1} s^{-1}), effects on *FF*, efficiency, and current density are more pronounced as shown in Figure 41 (c and d). The maxima seen with equal mobility combinations diminish slightly, but subsequent declines with increasing thickness are much faster. No

secondary increase in current density is observed. Because both *FF* and current density decrease simultaneously, efficiency no longer remains constant, but rather falls off more rapidly. However, even at device thicknesses approaching 200 nm, efficiency remains at ~3%. It should be noted that open circuit voltage is slightly higher when the mobility is dropped to $\mu_e = 10\mu_h$ as indicated in Figure 41 (a and c). This can be attributed to decreased Langevin recombination where lower mobility decreases the rate.

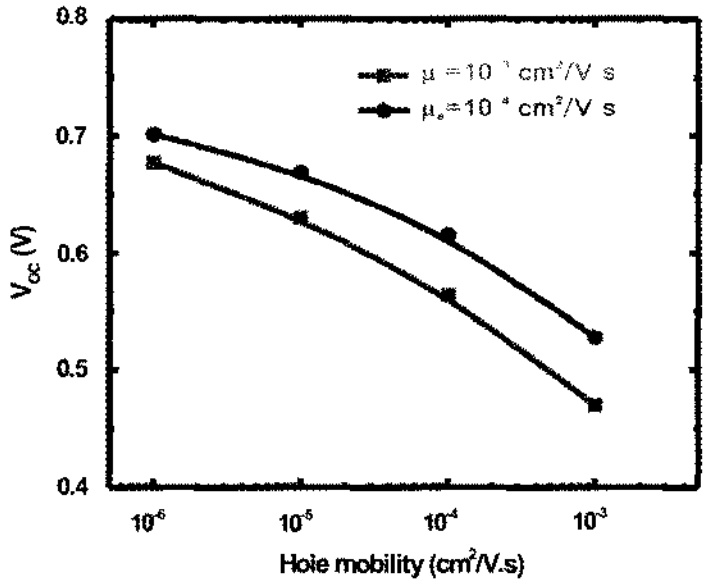

Figure 42. V_{OC} vs. hole mobility in PCPDTBT:$PC_{71}BM$ simulations based on two electron mobilities: $\mu_e = 10^{-3}$ cm^2 V^{-1} s^{-1} and $\mu_e = 10^{-4}$ cm^2 V^{-1} s^{-1}.

Figure 42 shows values for open circuit voltage as a function of hole mobility for two values of electron mobility ($\mu_e = 10^{-3}$ and 10^{-4} cm^2 V^{-1} s^{-1}) in PCPDTBT:$PC_{71}BM$. A one-order-of-magnitude decrease in electron mobility results in an increase in V_{OC}.

Conversely, increases in hole mobility for a constant electron mobility result in a decrease in V_{OC}.

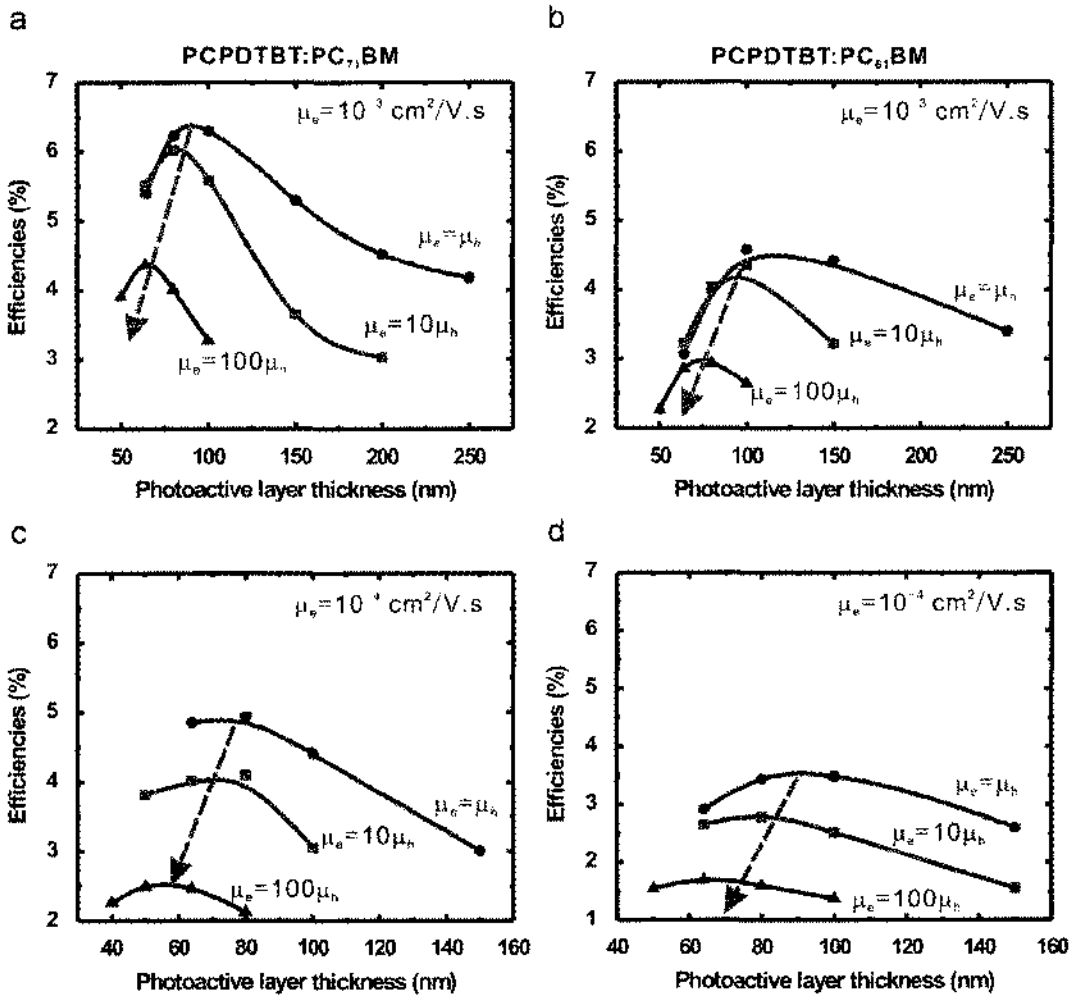

Figure 43. Efficiency as functions of photoactive layer thickness and electron/hole mobility ratios for PCPDTBT:PC_{71}BM and PCPDTBT:PC_{61}BM: (a) and (b) for $\mu_e = \mu_h = 10^{-3}$ cm^2 V^{-1} s^{-1}, $\mu_e = 10\mu_h$, and $\mu_e = 100\mu_h$, (c) and (d) for $\mu_e = \mu_h = 10^{-4}$ cm^2 V^{-1} s^{-1}, $\mu_e = 10\mu_h$, and $\mu_e = 100\mu_h$.

This simulated result clearly indicates that device performance should be balanced by controlling open circuit voltage and photocurrent since they affect the fill factor and subsequently the obtainable efficiency.

To better understand the dependence between carrier mobilities, thickness, and efficiency in PCPDTBT:$PC_{71}BM$ and PCPDTBT:$PC_{61}BM$, device efficiencies were simulated as a function of photoactive layer thickness for the following six carrier mobility ratios: $\mu_e = \mu_h = 10^{-3}$ cm^2 V^{-1} s^{-1}, $\mu_e = 10\mu_h$, and $\mu_e = 100\mu_h$, and $\mu_e = \mu_h = 10^{-4}$ cm^2 V^{-1} s^{-1}, $\mu_e = 10\mu_h$ and $\mu_e = 100\mu_h$. In every instance, PCPDTBT:$PC_{71}BM$ shows the greatest efficiency. With equal mobilities ($\mu_e = \mu_h = 10^{-3}$ cm^2 V^{-1} s^{-1}), a peak efficiency of nearly 6.5% is achievable at a device thickness of 90 nm (Figure 43(a)). As hole mobility decreases by one- and two-orders-of-magnitude, efficiency decreases to 6% and 4.4%, respectively. Also, the optimal device thicknesses required to achieve these values shrink to 80 and 65 nm. Simulation of PCPDTBT:$PC_{61}BM$ having the same mobility ratios (i.e., $\mu_e = \mu_h = 10^{-3}$ cm^2 V^{-1} s^{-1}, $\mu_e = 10\mu_h$, and $\mu_e = 100\mu_h$) shows the peak efficiencies to be 4.5%, 4.2%, and 2.9% at 100, 90, and 70nm (Figure 43(b)). This represents decreases in efficiency of ~31%, 30%, and 35%, respectively, compared to PCPDTBT:$PC_{71}BM$. Again, there is a corresponding decrease in device thickness necessary to obtain these efficiency values that result from the differing electron/hole mobility ratios.

When electron mobility is dropped to 10^{-4} cm^2 V^{-1} s^{-1}, efficiency as a function of photoactive layer thickness changes significantly from that seen at 10^{-3} cm^2 V^{-1} s^{-1}. There is an overall decrease in efficiency for each mobility ratio and the rate of change of efficiency with thickness is considerably faster for each order of magnitude change (i.e.,

$\mu_e = \mu_h = 10^{-4}$ cm^2 V^{-1} s^{-1}, $\mu_e = 10\mu_h$, and $\mu_e = 100\mu_h$). For PCPDTBT:PC_{71}BM, efficiencies are 4.8, 4.0, and 2.5 percent at 73, 70, and 55 nm, respectively (Figure 43(c)). At the same mobility ratios, PCPDTBT:PC_{61}BM shows device thicknesses of 90, 80, and 65 nm to achieve corresponding efficiencies of 3.5, 2.7, and 1.6%. By comparison, PCPDTBT:PC_{61}BM shows relative decreases in efficiency of 27, 33, and 36% at each of the three charge carrier mobility ratios (Figure 43(d)).

In conclusion, spectral absorption, fill factor, efficiency, and current density characteristics were obtained for both donor/acceptor blends and optimal thicknesses determined to attain maximum efficiency. For $\mu_e = \mu_h = 10^{-3}$ cm^2 V^{-1} s^{-1}, PCPDTBT:PC_{71}BM and PCPDTBT:PC_{61}BM each show their highest respective efficiencies at thicknesses around 90–100nm. However, the efficiency of PCPDTBT:PC_{71}BM is about 6.5% while that for PCPDTBT:PC_{61}BM is 4.5%. When electron and hole mobilities are decreased to 10^{-4} cm^2 V^{-1} s^{-1}, the efficiencies of both mixtures declines, though that for PCPDTBT:PC_{71}BM is still greater than PCPDTBT:PC_{61}BM. It should be noted that such efficiencies are based on high values of the Langevin recombination parameter (i.e., 0.1) where higher energy conversion efficiencies can be predicted with *lower* values of η. Further study must be conducted to more completely understand all the factors impacting ultimate device efficiency. However, it remains clear that optimum layer thickness is strongly dependent upon the magnitude and ratio of charge carrier mobilities.

ORGANIC TANDEM CELLS: LOW- & HIGH-BANDGAP DONOR POLYMERS

An interesting fabrication method currently being explored in the academic and industrial communities that shows considerable promise involves the use of flexible

organic photovoltaics and "roll-to-roll" processing whereby large numbers of solar cell devices are produced on large flexible plastic rolls [122,123]. While significant advances have been made, energy conversion efficiencies still remain too low to warrant marketability [3,33,36,95]. The primary efforts focused on improvement have mostly addressed optimizing fabrication methods and the quality of materials used [21,124]. Furthermore, modification of various parameters including active layer thickness and area, organic blend composition and morphology, interfacial contacts, and physical device configuration (e.g., single planar, tandem series/parallel, and blend-infiltrated nanostructures) all have an impact on the most critical device characteristics influencing PCE (η) [21,33,36,125,124]. Of these, the most important factors influencing η are open circuit voltage, current density, and fill factor according to the relationship previously shown in Equation (23)

$$\eta = \frac{J_{SC} \, x \, V_{OC} \, x \, FF}{P_{in}} \tag{23}$$

where P_{in} is the incident power impinging on the surface of the solar cell device. To date, considerable published research details the use of HBG polymers such as P3HT and fullerene-based derivatives as organic blend active layers in solar cells [95,126,127]. Unfortunately, these materials demonstrate less than ideal optical absorption in the visual range [124]. A partial solution to this problem has been to exchange HBG polymers with LBG alternatives in the active layer to collect a broader portion of the solar spectrum that includes longer wavelengths of light [110,111,112]. This technique has shown some improvement in efficiency, but not as much as would be necessary to enable organics to compete with inorganic photovoltaics. The next logical progression has been to combine the best properties of each type of cell into either series or parallel tandem structures so

that the broadest possible spectral content could be captured [128,129]. When designing a tandem structure, particularly of series configuration, the bottom cell ($E_{g,bottom}$) should be designed with high bandgap materials while the top cell ($E_{g,top}$) would consist of low bandgap materials (i.e., $E_{g,bottom} > E_{g,top}$). Therefore, incident photons with energy $h\nu > E_{g,bottom}$ are absorbed in the bottom cell while photons of lower energy ($h\nu < E_{g,bottom}$) are transmitted through the bottom subcell to be absorbed in the top cell. In this way, light harvesting can be optimized using a combination of low- and high-bandgap materials. In a series-connected configuration, the subcell having the lowest current density in the combined structure will determine the total current density achievable for the series tandem structure. Therefore, it is necessary that current densities in each subcell be matched and as high as possible. This is primarily accomplished through control of active layer thickness and proper choice of polymer:fullerene blends possessing different optical bandgaps in each subcell. Recently, Dennler, *et al.*, performed optical simulations of various device configurations using LBG and HBG polymer:fullerene blend combinations composed of the LBG polymer PCPDTBT and $PC_{61/71}BM$ and the HBG polymer P3HT with $PC_{61/71}BM$ [35]. Simulation results from his study indicated that optimal tandem structures comprised an LBG PCPDBTBT:$PC_{61}BM$ bottom cell and an HBG P3HT:$PC_{71}BM$ top cell [35]. However, such a device structure might have non-optimal light harvesting properties due to the placement of the low bandgap material at the bottom and the high bandgap material at the top. In this experiment, the optical simulation previously reported by Dennler, *et al.*, was re-accomplished and further extended to explore alternative tandem structures and predict their PCE by combining different combinations of low- and high-bandgap polymer:fullerene blends. Results

indicated that the highest energy conversion efficiency can be obtained by using the HBG P3HT:$PC_{71}BM$ as the bottom subcell and the LBG PCPDTBT:$PC_{71}BM$ for the top.

Using an optical and electrical simulation tool developed by our research group and tailored for organic tandem solar cell design [130], a number of optical and electrical properties were calculated for series tandem cells. The standard TMM and drift-diffusion electrical model approaches were implemented to calculate the current density (based on light transmission, reflection, and absorption), bimolecular recombination, exciton generation, dissociation probability, and carrier mobility [59,64]. The tandem structures employed top and bottom subcells made of two different blends of polymer:fullerene materials. The two subcells are sized in terms of their thicknesses to achieve matching current densities in both active layers.

The TMM-based optical model [72,115] was used to calculate the time-rate of absorbed photons, N_{ph}, in the two photoactive subcells. Note that N_{ph} depends on optical interactions in *all* the layers of the tandem design described in Figure 44.

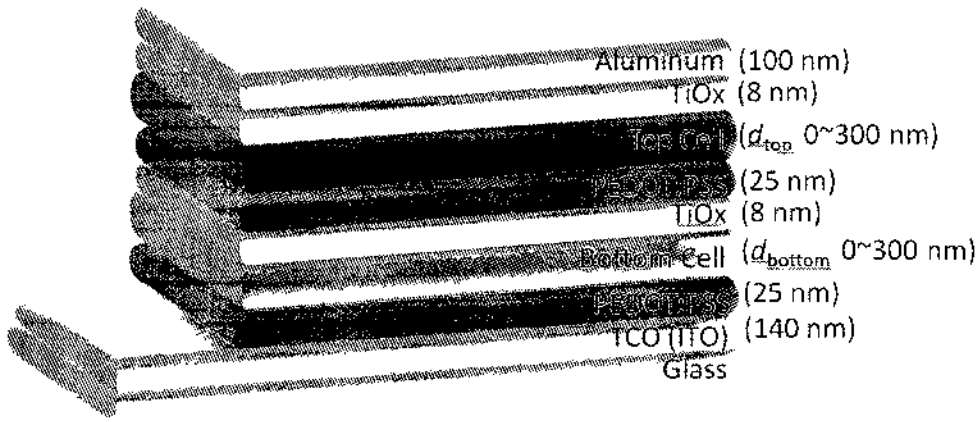

Figure 44. Schematic of the organic tandem structure used in the simulations.

The complex indices of refraction for each of the layered materials were obtained from Ref. [35] where spectroscopic ellipsometry was used to determine the n and k values. N_{ph} values in individual cells were converted into photocurrent densities (J_{ph}) for each of the combined sets of subcell thicknesses under study. The optical analysis was performed over a wavelength range of 350–900 nm based on AM 1.5G, 100 mW/cm^2 irradiance.

The aluminum electrode on the top of the device serves as a cathode and collects the electrons. The titanium oxide layers above the top and bottom cells act as electron transporters, hole blockers, and optical spacers that alter the amplitude of the optical field within the active layers [33]. The PEDOT:PSS layers beneath both top and bottom cells are hole transporters and ITO functions as the hole-collecting anode. A detailed schematic representation of the energy bandgaps of each of the component materials used in both Dennler's and our studies can be found in Ref. [33].

The organic drift-diffusion electrical model calculates the number of dissociated free charge carriers, charge carrier mobility and recombination, drift, diffusion, current density, and efficiency [64,130]. Onsager–Braun theory is used to calculate exciton dissociation while the Langevin equation describes bimolecular recombination [59,64]. Both results are incorporated into a one-dimensional, drift-diffusion model augmented by the exciton continuity equation so that device efficiency and current density can be assessed [64]. The overall current density for the device is the sum of the electron and hole current densities, which are found in terms of the drift-diffusion of charge carriers based on the continuity equations for the electron ($J_n(x)$) and hole current densities ($J_p(x)$) given by

$$J_n(x) = -q\mu_n \left(n(x)\,\frac{\partial\psi(x)}{\partial(x)} - \mathrm{V_t}\,\frac{\partial n(x)}{\partial(x)}\right) \tag{46}$$

$$J_p(x) = -q\mu_p \left(p(x)\frac{\partial\psi(x)}{\partial(x)} - \mathrm{V_t}\frac{\partial p(x)}{\partial(x)}\right) \quad (47)$$

From the Poisson equation, $\psi(x)$ is the potential, μ_n and μ_p are electron and hole mobilities, V_t is the thermal voltage, q is the electric charge, and $n(x)$ and $p(x)$ are the electron and hole densities.

Tandem cell designs are carefully chosen to scrutinize the effect of placing different organic blends in various sequences relative to the incident light entering the device. For example, Tandem I listed in Table 1 is composed of LBG polymer PCPDTBT and acceptor $PC_{61}BM$ in the bottom subcell with HBG polymer P3HT and acceptor $PC_{71}BM$ in the top.

Table 1. Four different combinations of polymer:fullerene structures used in the study.

Structure	Bottom cell	Top cell
Tandem I	PCPDTBT:$PC_{61}BM$	P3HT:$PC_{71}BM$
Tandem II	P3HT:$PC_{71}BM$	PCPDTBT:$PC_{71}BM$
Tandem III	P3HT:$PC_{71}BM$	PCPDTBT:$PC_{61}BM$
Tandem IV	P3HT:$PC_{61}BM$	PCPDTBT:$PC_{71}BM$

Tandem I is the same device structure as the one described in Refs. [33,35] that, upon fabrication, showed an energy conversion efficiency of more than 6% [33]. For Tandems II–IV, the spatial order is reversed; P3HT in the bottom subcell and PCPDTBT in the top. This is referred to as the ''HBG–LBG'' structure. Individual subcells in the three tandem designs use fullerene materials alternating between $PC_{61}BM$ and $PC_{71}BM$ in an attempt to achieve optimal combinations with the two donor polymer materials. The $PC_{61}BM$ fullerene is inferior to $PC_{71}BM$ [93] in terms of its light absorption properties.

Accordingly, a tandem design employing $PC_{61}BM$ for both subcells would result in excessively low efficiency due to low light absorption and was therefore omitted from this study.

Optical analysis of the device structure designated in Ref. [35] as "Case 3" was conducted initially. In our study, this structure is identified as Tandem I. The time-rate of absorbed photons was calculated and converted into photocurrent assuming 100% IQE. Figure 45 shows the intersection of two surfaces whose elevations represent photocurrents generated in the bottom and top cells for varying combinations of active layer thicknesses.

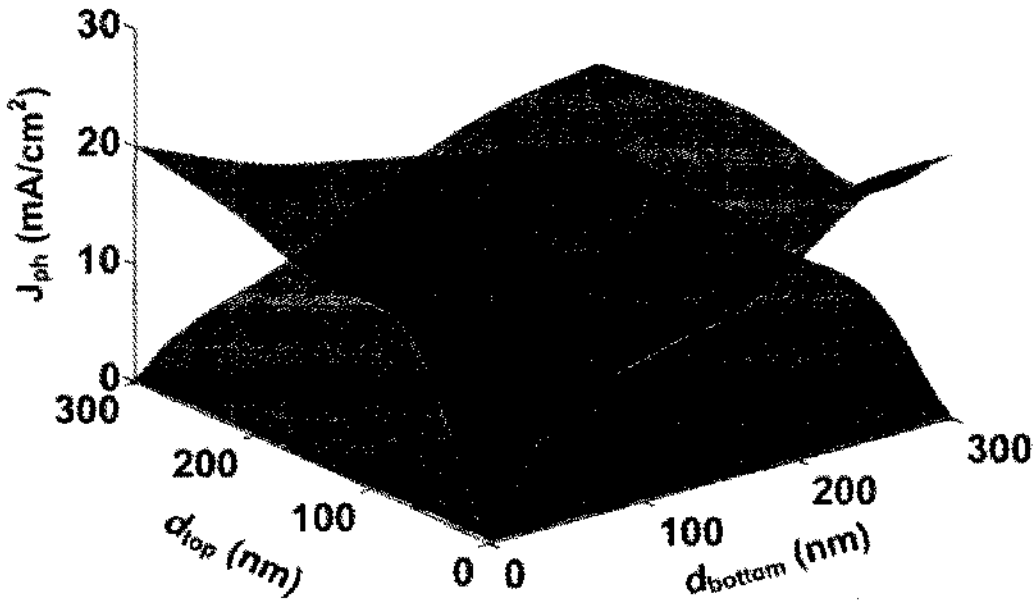

Figure 45. Isoline graph of photocurrent density (J_{ph}) plotted as a function of active layer thickness for both the top P3HT:$PC_{71}BM$ (d_{top}) and bottom PCPDTBT:$PC_{61}BM$ (d_{bottom}) cells. The intersection of the two contours indicates active layer thicknesses when photocurrent density (J_{ph}) is equal in both subcells.

The horizontal axes represent the top (d_{top}) and bottom (d_{bottom}) layer thicknesses, respectively. The two surfaces meet along a curved line (isoline) describing a continuum of d_{top} and d_{bottom} combinations that produce equal photocurrent from both subcells. This curved line is designated as the "Tandem–J_{ph}" curve. The results obtained using our model show excellent agreement with those in Ref. [35].

Figure 46(a) shows four Tandem–J_{ph} curves for combinations I–IV representing isolines matching J_{ph} between bottom and top subcells for each combination (Tandems I–VI) tested. Labels are placed next to each curve and a colormap is used to represent varying current density levels. It should be noted that Tandem III is composed of the same subcells as those in Tandem I, but with the order reversed. Among three of the tandem structures – II, III, and IV – Tandem IV produces the lowest J_{ph} over a wide range of subcell thicknesses. The low J_{ph} is attributed to poor light absorption of the P3HT:PC_{61}BM blend in the bottom cell. In Tandem II, a P3HT:PC_{71}BM blend is used to enhance light absorption in the bottom cell. The photocurrent in this particular structure increases significantly compared to that of Tandem IV. Note that Tandem II and IV use the same blends in the top cell—PCPDTBT:PC_{71}BM. For Tandem III, the PCPDTBT:PC_{61}BM blend is used in the top cell while P3HT:PC_{71}BM blend is used in the bottom cell. The photocurrent level in Tandem III is reduced due to poor light absorption in the top layer compared with that in Tandem II. Therefore, Tandem II produces the highest J_{ph} among the three tandem designs employing PC_{71}BM fullerene HBG–LBG structures. In Figure 46 (b) and (c), Tandem– J_{ph} curves clearly show (from two different viewpoints) that Tandem II produces higher photocurrent than Tandem I. This result suggests that the Tandem II HBG–LBG structure outperforms LBG–HBG

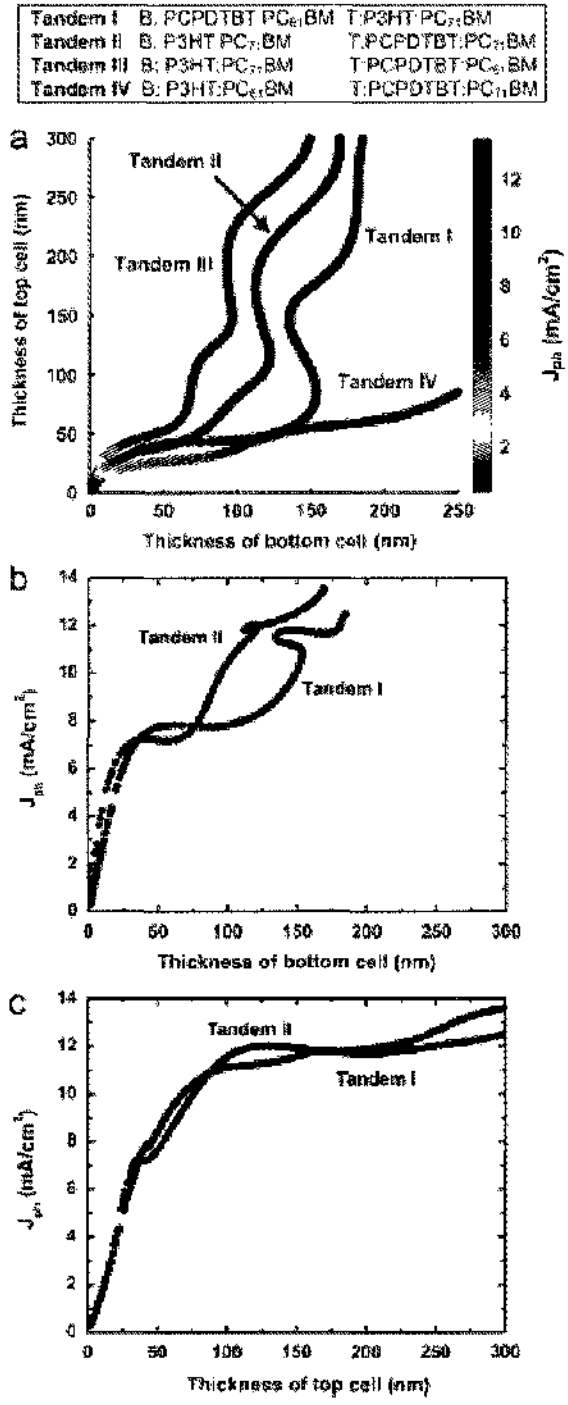

Figure 46. (a) Photocurrent densities (J_{ph}). Magnitude of the photocurrent densities in each isoline is indicated by varying color levels. (b) Tandems I and II–J_{ph} as a function of bottom subcell thickness, (c) Tandems I and II–J_{ph} as a function of top subcell thickness.

structures (e.g., Tandem I) in light absorption efficiency. It should be noted that the thicknesses of the top or bottom subcells are hidden parameters in these 2D plots since showing both thickness values in each case would significantly complicate the figure. To see a comprehensive "3D" representation of the same data where both top and bottom thicknesses are displayed, one may refer to Figure 45. Figures 46 (b) and (c) are similar in format to those seen in Ref. [35] so that comparison between both sets of results can be made more easily. Subsequent figures in this study show data plotted only against the top subcell thickness in order to avoid redundancy and because we believe that the data of interest versus the top subcell's thickness are more appropriate for interpretation.

Using our drift-diffusion electrical model for organic semi-conductors, the device performances of Tandems I and II were investigated by assessing charge carrier transport properties such as bimolecular recombination, exciton generation, dissociation probability, and carrier mobility [130]. The model was used to determine the photovoltaic parameters listed in Table 2 by fitting I-V characteristics of actual cells [68,91,107].

Table 2. Overview of material parameters used in the fit to the experimental data.

		Numerical value		
	Symbol	P3HT:PCBM	PCPDTBT:PCBM	Unit
Effective energy band gap	E_g	1.1	1.0	eV
Dielectric constant	ε	$3.4\varepsilon_0$	$3.4\varepsilon_0$	F/m
Effective density of states	N_{eff}	2.5×10^{19}	2.5×10^{19}	cm^{-3}
e-h pair distance	a	1.12	1.47	nm
Decay rate	k_f	3×10^5	1×10^5	1/s
Electron mobility	μ_e	9×10^{-3}	6×10^{-3}	$cm^2/V\,s$
Hole mobility	μ_h	7×10^{-3}	1×10^{-4}	$cm^2/V\,s$

Detailed processes for extracting the parameters listed in Table 2 are described elsewhere [130]. Although we consider the absolute energy bandgap of all materials when accounting for the light absorption and energy band alignment, a more important parameter determining open circuit voltage is the difference between the HOMO of the conjugated polymer and the LUMO of PCBM [95]. Hence, the effective energy bandgap in Table 2 was calculated based on the difference between the HOMO of the donor polymers (P3HT and PCPDTBT) and the LUMO of PCBM. Since there are large variations in the values reported for HOMO and LUMO of P3HT, PCPDTBT, and PCBM [4, 33,112,131], we fitted experimental IV characteristics to these quantities and used the results in our simulations. In addition, we introduced balanced charge carrier mobilities in the photoactive blends as shown in the table to achieve the highest possible device efficiencies and avoid space charge limited current [90,132,133]. For each structural design, one can determine the d_{top} and d_{bottom} values that produce equal J_{SC} values in the top and bottom cells. This continuum of d_{top} and d_{bottom} combinations is identified as the "Tandem–J_{SC}" curve. Figure 47(a) shows the Tandem–J_{SC} curves juxtaposed with Tandem–J_{ph} curves for Tandems I and II under the assumption of 100% IQE. Based on the colormap in this figure, one can see that the J_{SC} of Tandem II is greater than that of Tandem I for the given cell thicknesses. Figure 47 ((b) and (c)) show alternative views of the Tandem– J_{SC} curves in Figure 47(a). These Tandem–J_{SC} curves clearly show from two different viewpoints that Tandem II produces higher short circuit current density than does Tandem I. This result suggests that an HBG–LBG structure (Tandem II) may outperform an LBG–HBG structure (Tandem I).

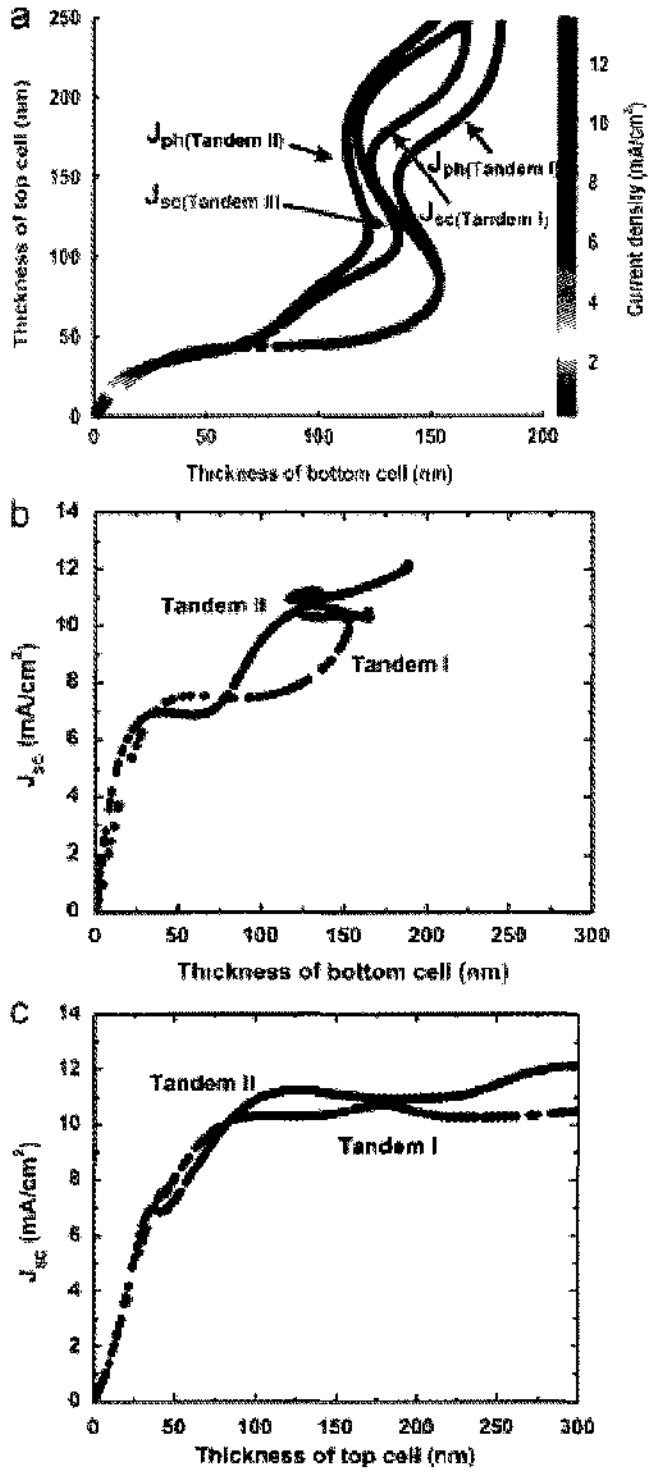

Figure 47. (a) Comparison of J_{ph} and J_{SC} for Tandems I and II as a function of subcell thicknesses. (b) Tandems I-, and II–J_{SC} are shown as a function of bottom subcell thickness. (c) Tandems I-, and II–J_{SC} are shown as a function of top subcell thickness.

The energy conversion efficiencies of Tandems I and II are calculated for selected d_{top} and d_{bottom} combinations. Figure 48 shows device efficiency (η) versus top cell thickness for Tandems I and II.

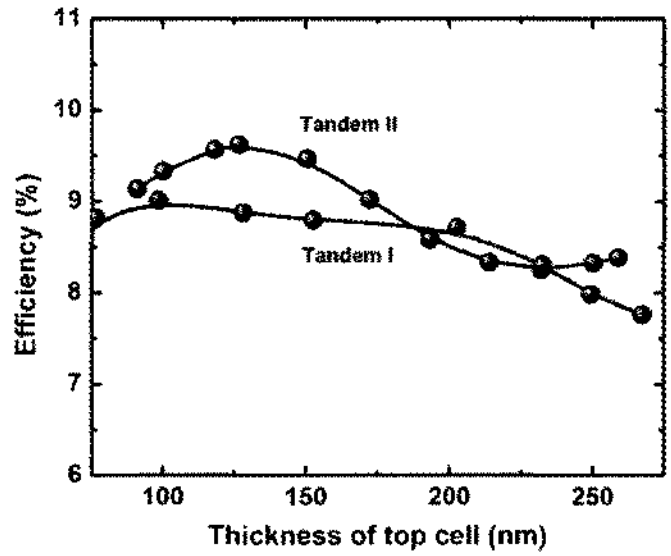

Figure 48. Tandems I and II device power conversion efficiencies as a function of top cell thickness.

For Tandem I, efficiency peaks at a value of 9% when d_{top} is about 106 nm. Tandem II shows its peak efficiency of 9.6% when d_{top} is about 125 nm. More importantly, the efficiency of Tandem II remains higher than that of Tandem I across a d_{top} range of 75 – 180 nm. For both designs, the efficiency decreases from the peak value with increasing thickness.

To further understand the HBG–LBG tandem designs, performance parameters such as J_{SC}, FF, V_{OC}, and η are examined together. Figure 49 shows these four

performance parameters for Tandem II. For a tandem (series) solar cell, V_{OC} is the sum of the voltages in the two subcells ($V_{OC} = V_{top} + V_{bottom}$) while J_{SC} is the lowest value [$J_{SC} = \min(J_{SC\ (\text{Subcell 1})}, J_{SC\ (\text{Subcell 2})})$] from either of the two subcells.

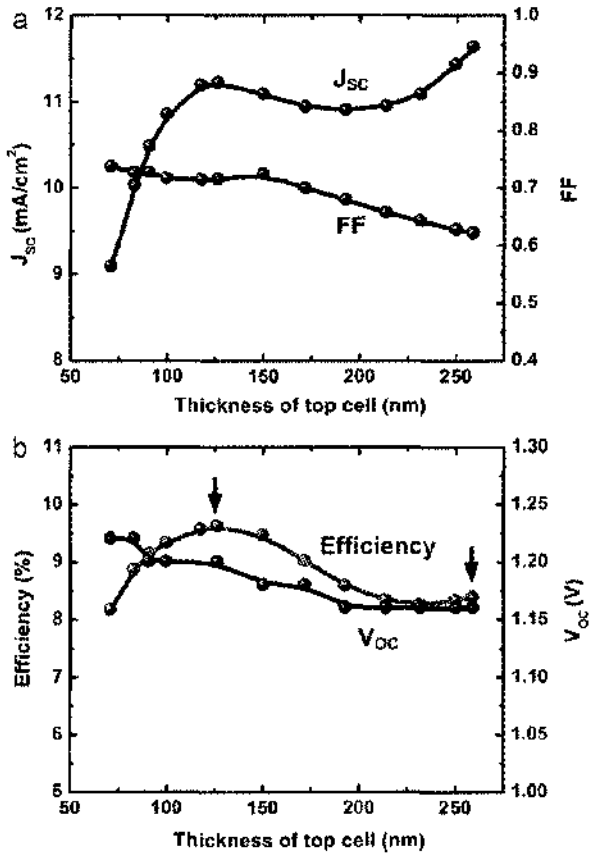

Figure 49. Simulated values for (a) J_{SC} and FF, (b) η and V_{OC} for Tandem II as functions of the thickness of the top subcell.

As shown in Figure 49(a), J_{SC} increases with thickness for 70–125 nm, drops slightly between 125 and 200 nm, and begins to increase again above 200 nm. A similar trend between Tandem–J_{SC} and Tandem–J_{ph} can be observed by comparing those curves in

Figures 46(c) and 47(c) where J_{SC} is lower than J_{ph} due to recombination effects in organic blends. *FF* decreases almost linearly from 0.74 to 0.63 with increasing thickness. Thick cells show reduced *FF* due to increased series resistance of the device. In Figure 49(b), one can confirm that V_{OC} is not as sensitive to the thickness as *FF* and J_{SC}.

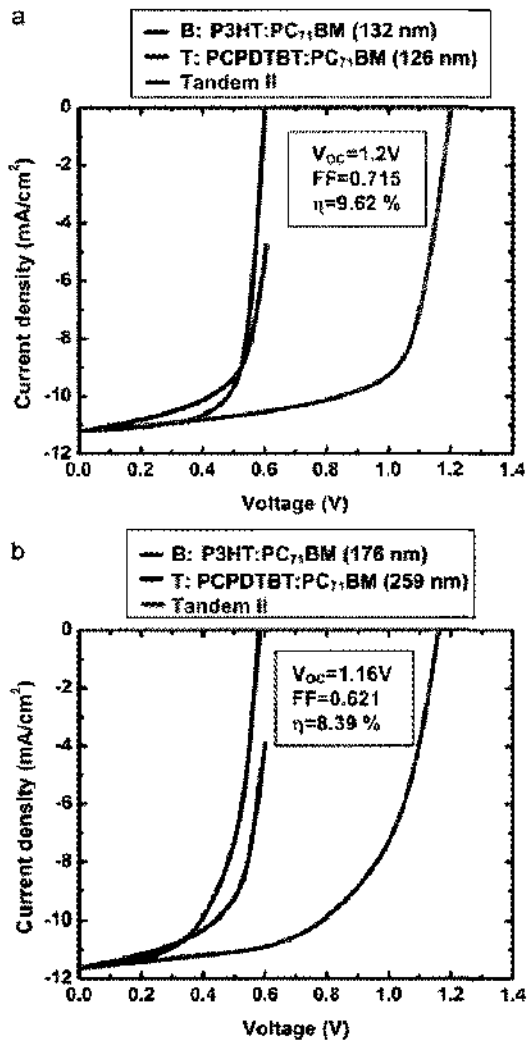

Figure 50. J–V curves for the Tandem II structure for different active layer thicknesses: (a) P3HT:PC_{71}BM (132 nm) / PCPDTBT:PC_{71}BM (126 nm) and (b) P3HT:PC_{71}BM (176 nm) / PCPDTBT:PC_{71}BM (259 nm).

Therefore, it is FF and J_{SC} that are the primary parameters affecting overall device efficiency. In Figure 49(b), the efficiency, η, shows its peak at about 125 nm – not at 250 nm where J_{SC} is even greater. This is because the reduced FF offsets the increase in current and results in lower efficiency at 250 nm.

To understand the interplay between the top and bottom cells of Tandem II and their influence on device efficiency, we chose two sets of d_{top} and d_{bottom} values along the Tandem–J_{SC} curve which have energy conversion efficiencies of 9.62% and 8.39% as indicated by arrows in Figure 49(b). For these two different thickness combinations, IV characteristics for the top cell (PCPDTBT:$PC_{71}BM$) and bottom cell (P3HT:$PC_{71}BM$) are shown in Figure 50. One may note that a tandem structure with η = 8.39% has significantly thicker bottom and top cells than a tandem structure with η = 9.62%. Such thick active layers in a tandem solar cell like the one in Figure 50(b) result in lower FF and open circuit voltage compared to a tandem cell like that shown in Figure 50(a). Interestingly, the poor FF observed in Figure 50(b) is due to the thick PCPDTBT:$PC_{71}BM$ top cell while a P3HT:$PC_{71}BM$ bottom cell has reasonable fill factor. It is noteworthy that the experimental FF values for PCPDTBT:$PC_{71}BM$ are normally found to be about 0.55 [33,112,131] while P3HT:PCBM cells have FF = 0.6 – 0.69 over a wide range of device thicknesses up to 400 nm [33,91,134]. Therefore, even though the tandem structure in Figure 50(b) shows greater short circuit current compared with the tandem cell in Figure 50(a) as a result of absorption being greater with increased thickness in each subcell, fill factor in the PCPDTBT:$PC_{71}BM$ top cell is significantly reduced. This limits overall performance of the cell in Figure 50(b).

Tandem solar cell designs have the potential to significantly improve power conversion efficiencies and raise the performance of conventional planar-style devices to a new level. This work presents some design rules for tandem solar cells where high-efficiency cells can be achieved through control of material properties such as HOMO, LUMO, and energy band gap [4]. Simply reducing polymer bandgap may not result in larger efficiencies since each material parameter affects efficiency in tandem structures [4]. Hence, the way ahead must also include the design of new materials where relative HOMO and LUMO values between donors and acceptors can be effectively controlled. Key factors that must be addressed in the effort to achieve these greater efficiencies include developing better polymer donor materials, accurately controlling relative HOMO and LUMO levels between device layers, and tailoring energy bandgap values to achieve the highest values of V_{OC}, J_{SC}, and FF. Our results indicate that the fullerene, $PC_{71}BM$, has superior optical and electrical characteristics as compared to $PC_{61}BM$. Additionally, energy bandgap considerations play an important role. In series tandem cells, the bottom subcell should consist of high bandgap materials while the top is composed of low bandgap polymer. This ensures that photons having energy lower than the bottom subcell bandgap will be transmitted to the top, low-bandgap subcell, and be absorbed there. In this way, light energy can be harvested more optimally and a greater portion of the visible and UV spectra captured. Optical transfer matrix methods and commonly used organic electrical models are sufficient to accurately describe organic tandem solar cell physics and simulate the structure described in this experiment. Simulation results from this study demonstrate that device efficiencies exceeding 9% can be achieved with series tandem cells composed of P3HT:$PC_{71}BM$ in the bottom subcell

and PCPDTBT:$PC_{71}BM$ in the top. Individual subcells in this alternative design still retain the characteristics of single-cell structures. Remarkable improvements in device efficiency, current density, open circuit voltage, and fill factor may be achievable through the appropriate selection of combinations of low and high bandgap polymers and fullerene acceptors, controlling their unique optical and electrical characteristics, and spatially ordering subcells to capitalize on unique absorption characteristics.

ORGANIC TANDEM CELLS: PCPDTBT:$PC_{61}BM$ & P3HT:$PC_{71}BM$ SUBCELLS

The limited absorption profiles of currently available organic materials prevent the attainment of higher efficiencies [4,135,136]. To overcome this shortcoming, multijunction organic solar cells [4,135,136] continue to be investigated as a potential design modification for achieving high-efficiency photovoltaics. These multijunction tandem solar cells offer a number of advantages including increased open circuit voltage and short circuit current density when connected in series or parallel [135,136], respectively. The most common configuration comprises a series connection of two or three subcells where light absorption is accurately controlled to balance photocurrent. In this experiment, additional work was done to assess the results obtained by Dennler *et al.*, [35] on $PC_{61/71}BM$ and PCPDTBT:$PC_{61/71}BM$ tandem structures. Their simulations assumed balanced photocurrent based on 100% internal quantum efficiency (IQE) where all absorbed photons in the active layers of each subcell ultimately contribute to photocurrent (J_{ph}). In real organic solar cells, several charge transport properties [62,59,63,] such as exciton generation and dissociation, bimolecular recombination, and unbalanced charge transport inside the active layers must be considered when designing optimal tandem structures since those factors cause current density (J_{SC}) to deviate from

J_{ph} obtained when IQE = 100%. Considering all the factors described in Experiment 3 above, we carried out electrical simulations as well as optical analysis using our organic drift-diffusion model and the optical TMM model tailored for design analysis of tandem organic structures.

A schematic of the tandem device simulated is shown in Figure 51. In the bottom cell, multiple material

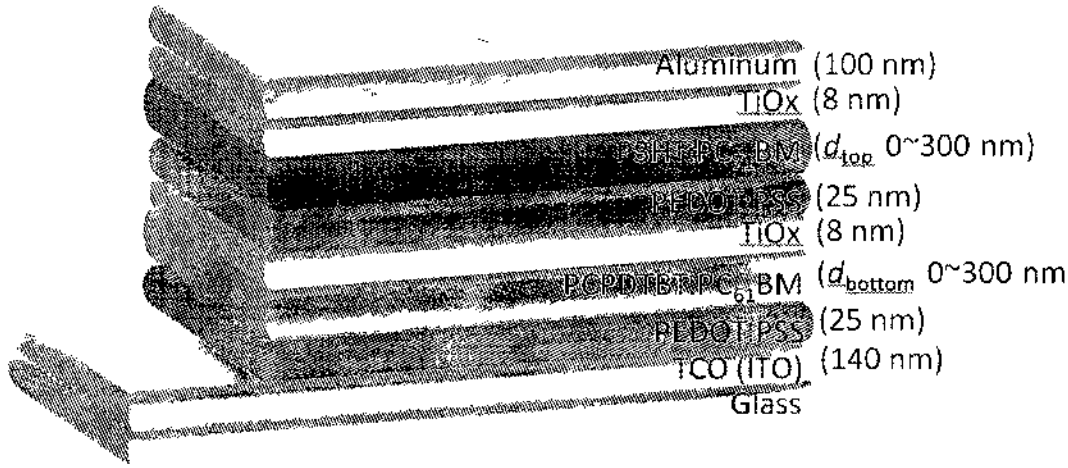

Figure 51. Schematic diagram of tandem P3HT:PCBM / PCPDTBT:PCBM structures. Thicknesses of active layers were varied from 0–300 nm.

layers are stacked in the sequence: ITO (140 nm) / PEDOT:PSS (25 nm) / PCPDTBT:$PC_{61}BM$ (d_{bottom}) / TiO_2 (8 nm). The top cell is formed similarly: PEDOT:PSS (25 nm) / P3HT:$PC_{71}BM$ (d_{top}) / TiO_2 (8 nm) and finally, Al (100 nm) on the top. Note that d_{bottom} and d_{top} are the thicknesses of the active layers allowed to vary up to a maximum of 300 nm. P3HT is known to have an effective absorption range

between UV and 650 nm [35] while the low bandgap polymer, PCPDTBT, has an energy bandgap of approximately 1.5 eV that extends the absorption spectra into the infrared region [68,110,111]. Therefore, the combination of these two polymer materials covers a wide spectral absorption range from UV to infrared. It should be noted that this tandem structure has produced energy conversion efficiencies as high as 6.5% [33].

Table 2 detailing the material parameters used in the fit to the experimental data is reproduced here.

Table 2. Overview of material parameters used in the fit to the experimental data.

		Numerical value		
	Symbol	P3HT:PCBM	PCPDTBT:PCBM	Unit
Effective energy band gap	E_g	1.1	1.0	eV
Dielectric constant	ε	$3.4\varepsilon_0$	$3.4\varepsilon_0$	F/m
Effective density of states	N_{eff}	2.5×10^{19}	2.5×10^{19}	cm^{-3}
e-h pair distance	a	1.12	1.47	nm
Decay rate	k_f	3×10^5	1×10^5	1/s
Electron mobility	μ_e	9×10^{-3}	6×10^{-3}	$cm^2/V\,s$
Hole mobility	μ_h	7×10^{-3}	1×10^{-4}	$cm^2/V\,s$

The parameters for P3HT:PCBM were extracted based on device efficiencies over 4% and an active layer thickness of 175 nm [107]. The reference mobility ratio between electrons and holes ($\mu_e : \mu_h$) is taken close to 1, which is required to achieve higher energy conversion efficiencies in thicker organic blends. Even though the mobilities listed in Table 2 are one order of magnitude higher than the experimentally measured values from Ref. [107], our values have been fitted to other experimental data [91] where the device thickness exceeded 300 nm. Figure 52(a) shows the experimental and fitted data. In contrast, device parameters for PCPDTBT:PCBM are not well investigated

requiring that we use experimental IV characteristics from Ref. [68]. Results are shown in Figure 52(b). The best fit values for the pair separation distance, a = 1.47 nm, and decay rate, $k_f = 10^5\ s^{-1}$, were determined by comparing experimental IV characteristics with fitting data for an active layer thickness of 110 nm.

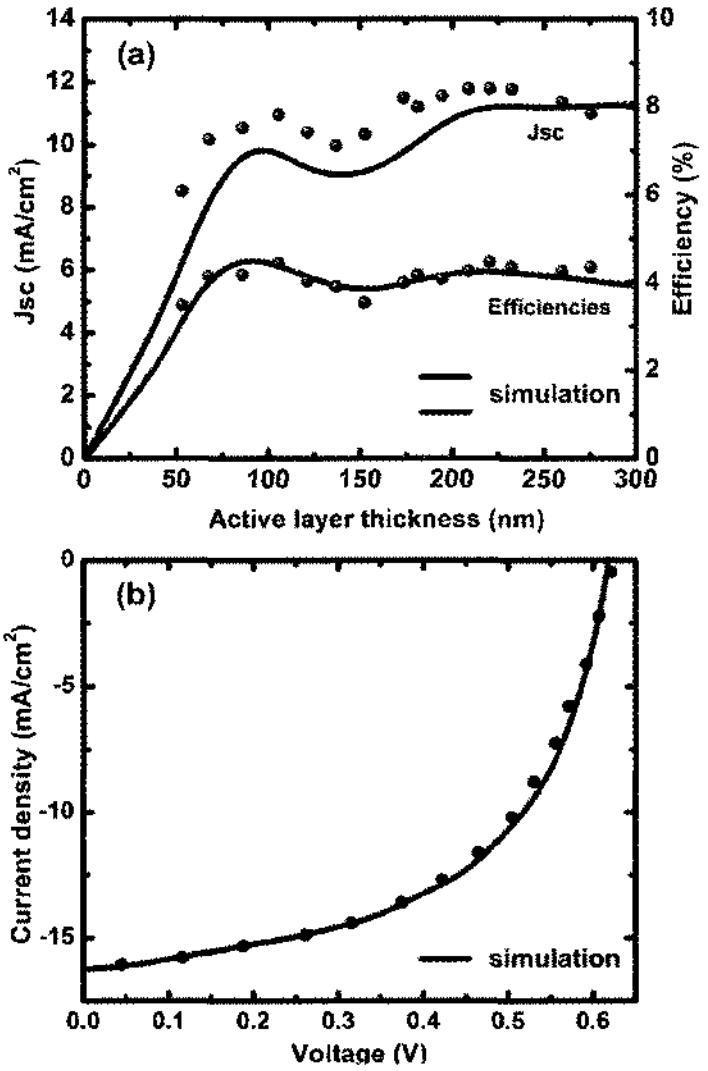

Figure 52. (a) Comparison of current density and efficiencies between experimental data (dots) and simulation (solid lines) of P3HT:PCBM, [91], and (b) comparison of simulated and experimentally-measured IV characteristics of PCPDTBT:PCBM having an active layer thickness of 110 nm [68].

These values differ somewhat compared to previously reported values [137] where a = 2.1 nm and the decay rate k_f = 1.7x10^7 s^{-1}. Such a difference might come from the improvement in optical and electrical performance that results from adding alkane dithiols to PCPDTBT polymer-fullerene blends [68].

Current matching between subcells in series tandem structures is a critical performance requirement where the number of absorbed photons [35], charge carrier transport, and bimolecular recombination [58] must be optimized to balance the photocurrent. Low charge carrier mobilities and unbalanced charge distribution that results from an imbalance of electron/hole mobilities in organic photovoltaics [90,97] are characteristics of organic solar cells that make it complicated to match current densities between subcells.

Table 3. Mobilities of electrons and holes for Cases I, II, and III.

	Numerical value	
	Bottom cell PCPDTBT:$PC_{61}BM$ ($cm^2/V\ s$)	Top cell P3HT:$PC_{71}BM$ ($cm^2/V\ s$)
Case I	$\mu_e = 6\times10^{-3}$	$\mu_e = 9\times10^{-3}$
	$\mu_h = 1\times10^{-3}$	$\mu_h = 7\times10^{-4}$
Case II	$\mu_e = 6\times10^{-3}$	$\mu_e = 9\times10^{-3}$
	$\mu_h = 1\times10^{-3}$	$\mu_h = 7\times10^{-3}$
Case III	$\mu_e = 6\times10^{-3}$	$\mu_e = 9\times10^{-3}$
	$\mu_h = 1\times10^{-4}$	$\mu_h = 7\times10^{-3}$

In this study, three different cases were investigated employing a PCPDTBT:$PC_{61}BM$ bottom subcell and a P3HT:$PC_{71}BM$ top cell: Case I—unbalanced charge carrier mobilities in the P3HT:$PC_{71}BM$ subcell with balanced mobilities in the

PCPDTBT:PC_{61}BM cell, Case II—balanced charge carrier mobilities in both top and bottom subcells, and Case III—unbalanced carrier mobility in PCPDTBT:PC_{61}BM with balanced mobilities in P3HT:PC_{71}BM. Table 3 shows electron and hole mobilities for each subcell in the three cases. The values for the electron and hole mobilities for P3HT:PCBM [134] and PCPDTBT:PCBM [111] are varied based on experimental results reported in the literature. To consider unbalanced charge carrier transport, we set hole mobility one order of magnitude lower than that of the electrons as this is consistent with experimentally observed values for organic blends [111,134].

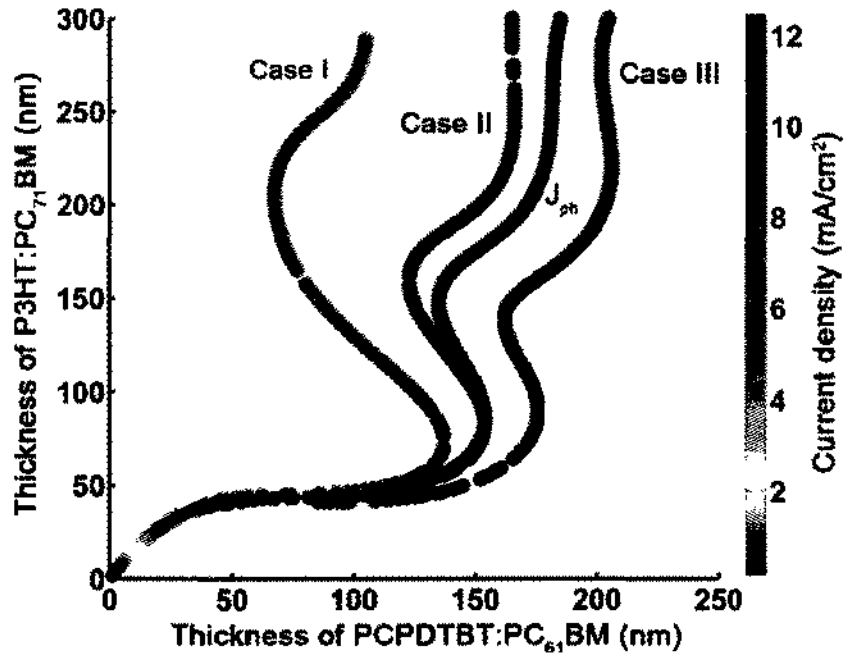

Figure 53. Isolines matching current densities between a PCPDTBT:PC_{61}BM bottom cell and a P3HT:PC_{71}BM top cell for different Cases I, II, and III. As a guide, an isoline of *Jph* was calculated by assuming that the absolute numbers of photons in each subcell are completely converted to photocurrent (*Jph*). Current densities in each isoline are indicated by different levels of color.

Figure 53 shows an isoline graph where the current densities for each case are matched between the top and bottom cells as a function of both cell thicknesses. The J_{SC} values for each case were calculated based on the electrical and optical models described in Chapter 2. We first calculated the isoline as a guideline where the total number of photons, N_{ph}, absorbed in each cell are matched and converted into photocurrent density, J_{ph}, by assuming that IQE was equal to 100%. J_{SC} deviated from the J_{ph} isoline in all three cases. When charge carriers in both cells are balanced (Case II), J_{SC} is very close to J_{ph}. However, when charge carriers are unbalanced as in Cases I and III, the thickness of each subcell will be modified dependent upon the degree of imbalance of the charge carrier mobilities in the bottom or top cell. In Case I where the P3HT:PC_{71}BM top cell has unbalanced carrier mobilities, d_{bottom} (PCPDTBT:PC_{61}BM) should be reduced. In contrast, when Case III has unbalanced charge mobilities, d_{bottom} (PCPDTBT:PC_{61}BM) should be increased.

To investigate the effect of charge carrier mobility on isoline variations, we calculated the J_{SC} for each cell by fixing d_{top} (P3HT:PC_{71}BM) = 100 nm while varying d_{bottom} (PCPDTBT:PC_{61}BM) from 0 to 300 nm as shown in Figure 54. Figure 54(a) shows that J_{ph} for P3HT:PC_{71}BM continuously decreases with increased d_{bottom} while J_{ph} for PCPDTBT:PC_{61}BM steadily increases from 180 to 300 nm thickness though at a slower rate. In this configuration, the J_{ph} in each cell are matched with the active layer thicknesses of d_{bottom} = 150 nm and d_{top} = 100 nm. When hole mobility dropped by one order of magnitude from $\mu_h = 7\text{x}10^{-3}$ to $\mu'_h = 7\text{x}10^{-4}$ cm^2 V^{-1} s^{-1} with a constant electron mobility of $\mu_e = 9\text{x}10^{-3}$ cm^2 V^{-1} s^{-1} in P3HT:PC_{71}BM (Case I), a significant drop in J_{SC} was observed.

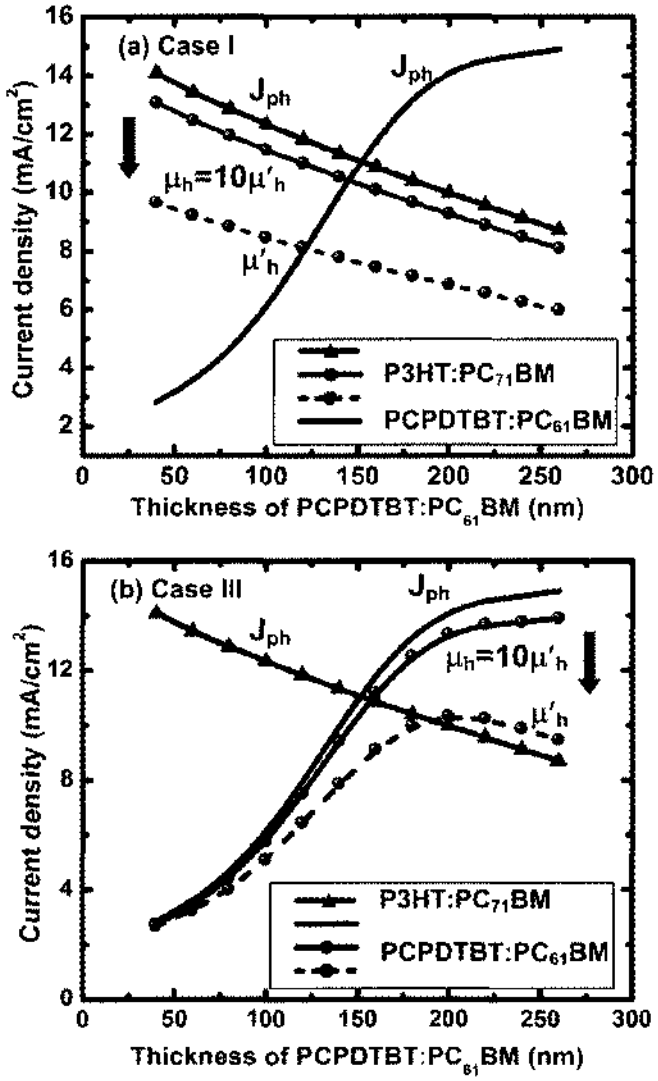

Figure 54. Variation in isolines with different charge carrier mobilities for (a) Case I and (b) Case III as a function of d_{bottom} (PCPDTBT:PC_{61}BM), but with fixed d_{top} = 100 nm (P3HT:PC_{71}BM).

For Case I, current density (solid line with spheres) slightly deviates from J_{ph} with $\mu_h = 7 \times 10^{-3}$ cm^2 V^{-1} s^{-1} and $\mu_e = 9 \times 10^{-3}$ cm^2 V^{-1} s^{-1} in P3HT:PC_{71}BM. With $\mu'_h = 7 \times 10^{-4}$ cm^2 V^{-1} s^{-1} and $\mu_e = 9 \times 10^{-3}$ cm^2 V^{-1} s^{-1}, a significant current drop (dotted line with spheres) was observed. For Case III, when the hole mobility in PCPDTBT:PC_{61}BM was

dropped from $\mu_h = 1 \times 10^{-3}$ cm^2 V^{-1} s^{-1} (blue solid line with spheres) to $\mu'_h = 1 \times 10^{-4}$ cm^2 V^{-1} s^{-1} (blue dotted line with spheres) with constant $\mu_e = 6 \times 10^{-3}$ cm^2 V$_{-1}$ s^{-1}, a significant current drop was observed. Solid lines indicate the photocurrent J_{ph} generated with IQE = 100%. Therefore, d_{bottom} should be modified to have a thinner active layer. The shift toward a thinner d_{bottom} is required to reduce the absorption of N_{ph} in the bottom cell, thereby reducing J_{SC} in PCPDTBT:PC$_{61}$BM and subsequently matching the reduced J_{SC} of the top cell. It should be also noted that increasing d_{top} will lead to increased bimolecular recombination and subsequently more current density drops in the top cell. This in turn will require d_{bottom} to be made thinner. This can be seen in Figure 53 where increased deviation from J_{ph} is observed with increased d_{top} which leads to a decrease in the thickness of the active layer, d_{bottom}, in the bottom cell.

In Case III where the charge carrier mobility of PCPDTBT:PC$_{61}$BM in the bottom cell is unbalanced, the J_{SC} is shifted toward the right, away from J_{ph} in Figure 53 indicating that a thicker active layer in the bottom solar cell is required to match current between the bottom and top cells [Figure 54(b)]. Since the drop in J_{SC} in the bottom cell occurs due to increased bimolecular recombination that results from decreasing hole mobility from $\mu_h = 1 \times 10^{-3}$ to $\mu'_h = 1\times10^{-4}$ cm^2 V^{-1} s^{-1} and holding electron mobility constant at $\mu_e = 6\times10^{-3}$ cm^2 V^{-1} s^{-1}, it is necessary to drop J_{SC} in the top cell. This can be achieved by increasing d_{bottom} which will have the effect of allowing more photons to be absorbed in the bottom cell. Consequently, N_{ph} in the bottom cell is increased, thereby decreasing N_{ph} in the top cell, and subsequently matching the J_{SC} between both.

The simulated results for PCE, J_{SC}, FF, and V_{OC} are shown in Figure 55. As expected, when charge carriers in both the bottom and top cells are balanced for Case II,

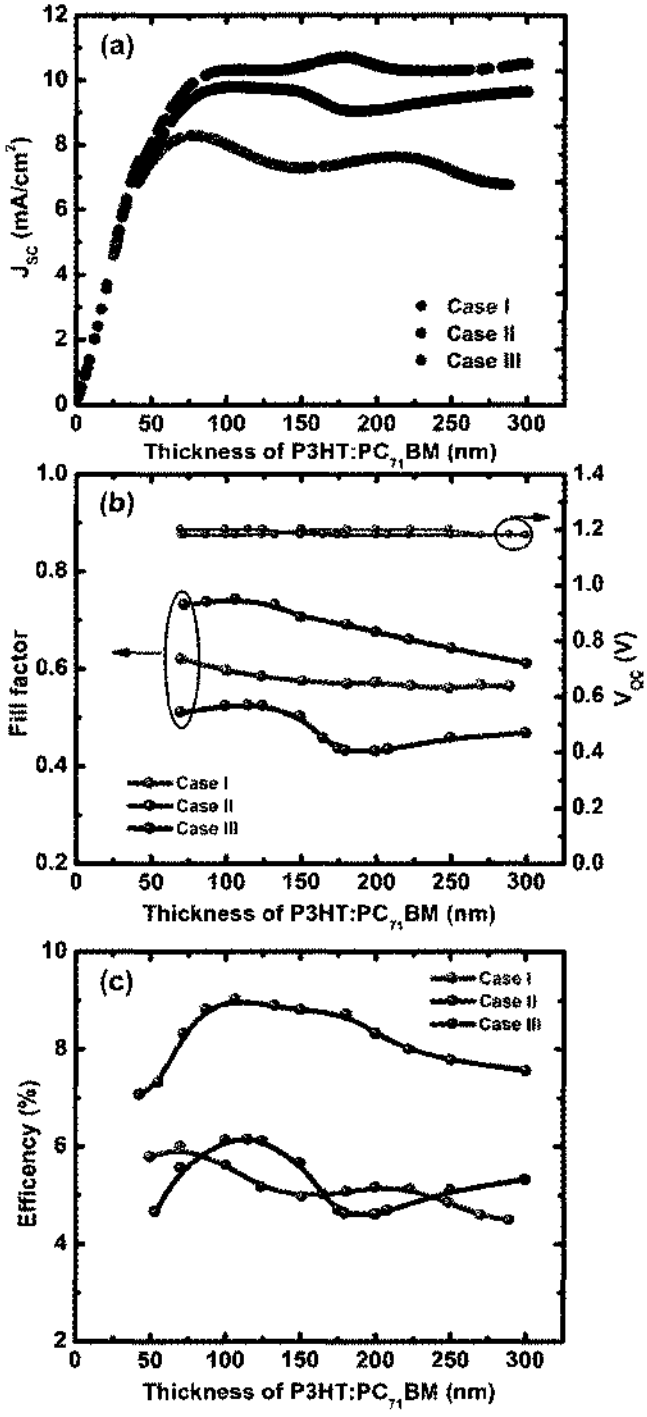

Figure 55. (a) Current density, (b) *FF* and V_{OC}, and (c) efficiency for each of the different Cases I, II, and III as a function of a P3HT:PC$_{71}$BM thickness. The highest efficiency – 9% – in Case II is achieved with active layer thicknesses of d_{bottom} (PCPDTBT:PC$_{61}$BM) = 146 nm and d_{top} (P3HT:PC$_{71}$BM) = 106 nm.

the highest J_{SC}, V_{OC}, and energy conversion efficiency are obtained. The J_{SC} initially increases, but reaches a plateau of ~11 mA cm^{-2} as shown in Figure 55(a). In contrast, *FF* in Figure 55(b) continuously decreases with increased active layer thickness. Therefore, the highest efficiency obtained was about 9% with active layer thicknesses of d_{bottom} (PCPDTBT:PC$_{61}$BM) = 146 nm and d_{top} (P3HT:PC$_{71}$BM) = 106 nm, as shown in Figure 55(c). For a wide range of active layer thicknesses for the bottom and top cells for Case II, an overall energy conversion efficiency of 8%–9% can be achieved. However, it should be noted that in our simulations balanced high mobilities in the subcells led to high *FF* (~0.74) and a corresponding η = 9%. If the experimental *FF* = 0.67 is considered [33], the realistic energy conversion efficiency should reach approximately 8.14%. On the other hand, the energy conversion efficiency for Cases I and III recorded below 6%. For Case I, a rapid drop in current density in Figure 55(a) is observed and is responsible for the lower η.

As shown in Figure 56(a) for the IV characteristics of individual cells in the tandem structure for Case I, the P3HT:PC$_{71}$BM top cell has unbalanced charge carrier mobilities that are attributed to the lower current density of the tandem design. In contrast, higher current density is observed for Case III, but the *FF* is governed by the PCPDTBT:PC$_{61}$BM bottom cell and is much lower than that of Case I as shown in Figure 56(b). The reported *FF* for PCPDTBT:PCBM shows values less than 0.55 [68,,33,112] while P3HT:PCBM produces *FF* = 0.6–0.69 [33,134]. Therefore, in Case III the lower *FF* of the bottom PCPDTBT:PC$_{61}$BM cell restricts the efficiency.

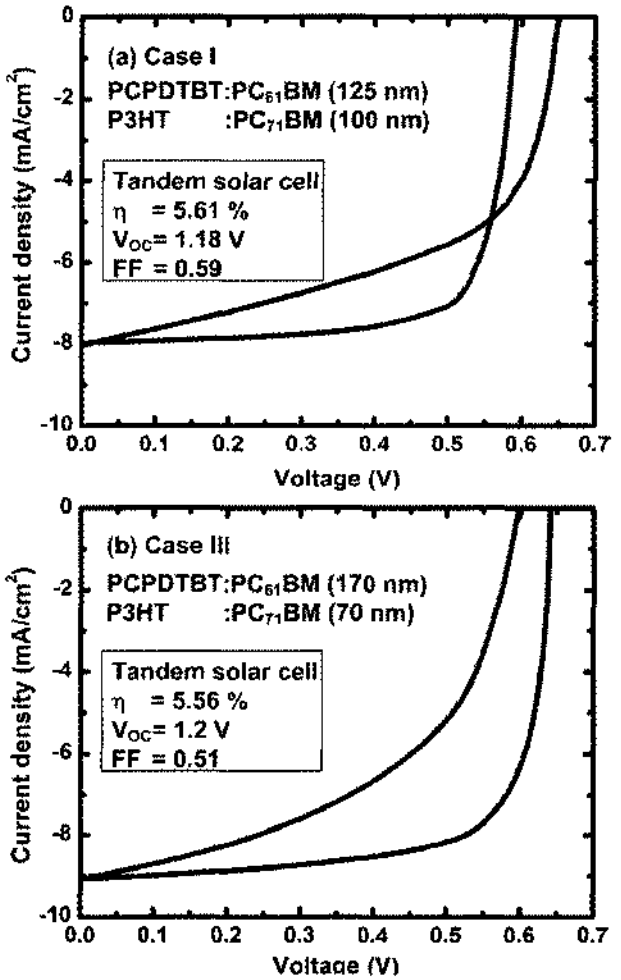

Figure 56. IV characteristics of each subcell in the tandem structures for (a) Case I and (b) Case III with different active layer thicknesses.

Using PCPDTBT:$PC_{61}BM$ for the bottom subcell and P3HT:$PC_{71}BM$ for the top, energy conversion efficiency for this device structure can be as high as 9%. However, if charge carriers are unbalanced in either subcell, energy conversion efficiencies can drop to 4% ~ 6% as a result of either lower current density or lower *FF* in the subcell. Charge carrier mobilities must be balanced in each subcell to achieve the highest energy conversion efficiencies in tandem structures.

Results from the four experiments described suggest that modeling and simulation are critical steps that must be accomplished to further improve organic solar cell efficiency. In doing so, much time and many valuable resources can be conserved while fabricating actual devices. At the same time, performance enhancements can be realized more expeditiously.

CHAPTER IV

FABRICATION METHODS AND CHARACTERIZATION

FABRICATION FACTORS – LAYER-BY-LAYER

A multitude of factors must be taken into account when fabricating organic solar cells. None of these aspects is independent of the others, but rather they are inextricably linked together and high-efficiency device performance is dependent on their successful management. Even a single planar organic BHJ solar cell presents a structure that belies its level of complexity. Figure 57 shows a single planar cell and the many parameters that impact, or must be controlled, throughout the manufacturing process. Note, the *interface* layers are shown to have thicknesses comparable to functional layers. In fact, interfaces are actually very thin (nanoscale) where adjacent layers touch.

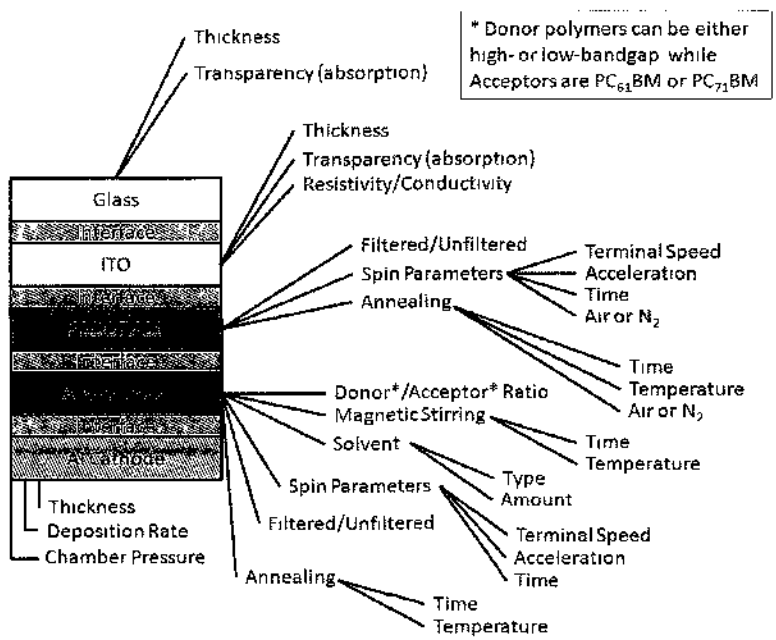

Figure 57. Fabrication parameters impacting device efficiency.

For glass substrates that form the foundation for the other layers in the cell structure, thicknesses can be in the millimeter range. The glass (or, in some cases, quartz) must be of high purity and optically transparent. Some glass substrates are coated with anti-reflecting material to more closely match the indices of refraction with the ambient environment (i.e., air). This has the effect of reducing surface reflection and more efficiently channeling photon energy into the cell structure where it is absorbed in the active layer. However, discussion of such coatings is beyond the scope of this dissertation and will not be addressed in detail.

A highly-conductive electrode is deposited on the glass and it too, must be as optically transparent as possible and of sufficient purity to ensure sheet resistance in the range (typically) of about 5 – 10 ohm/square. The transparent conductive oxide (TCO) most commonly used is indium tin oxide (ITO). ITO is an n-type semi-conductor of low resistivity and high work function that easily transmits light in the visible portion of the spectrum [138]. The resistivity/conductivity and transparency, which impacts absorption, are dependent on the thickness of the ITO layer. It is often sputtered (although other methods are also used) onto the glass surface in a highly-controlled manner. The glass/ITO combination is then annealed to obtain ideal optical, electrical, and morphological properties. Importantly, ITO has a work function in the range 4.5~4.7 eV and can be used as either a cathode or as an anode depending on the solar cell configuration (e.g., conventional or inverted).

PEDOT:PSS is spin-cast on top of the ITO electrode to serve a number of purposes including as a protective buffer between the active layer and the ITO electrode, as a hole-transporter, and to increase V_{OC} [139,140]. Prior to deposition, PEDOT:PSS

may be passed through a 0.45 micron filter to remove any aggregations that could result in the formation of recombination sites. Another consideration to be addressed during spin-casting is whether or not to perform this step in ambient air where O_2 and H_2O levels are high, or in a nitrogen environment where O_2 and H_2O levels are maintained below 0.1 ppm. Normally, it isn't a problem to spin PEDOT in air since it is already solvated in water. However, it is important to optimize the thickness of this layer by controlling acceleration, terminal spin speed, and the length of time for the spin. The thickness is basically determined in the first 5~6 seconds of the spin and the remaining time allows the PEDOT layer to dry. This is important since, being solvated in water, the thin film will contract from the edges of the substrate toward the center resulting in highly variable thickness and non-contiguous coverage over the regions where the device active areas will be formed. Once spin-casting is of the PEDOT is complete, the structure must be annealed. PEDOT:PSS comprises donor (PEDOT) and acceptor (PSS) components much like those in the active layer. Therefore, annealing is used to transform this layer to a more crystalline molecular arrangement. Time, temperature, and the environment (N_2 or O_2) influence the electrical, optical, and morphological properties of the PEDOT layer. A properly prepared PEDOT:PSS layer will ensure a good interface between the ITO electrode and the active layer which is composed of the donor polymer and acceptor fullerene and are combined in a suitable solvent medium. There should be no pinholes or discontinuities in the PEDOT layer as this can lead to leakage current and shorting.

The active layer is subsequently spun on top of the PEDOT taking into account all of the same factors previously identified, but with some additional concerns. Once the choice of which donor/acceptor couple to use is made (e.g., LBG or HBG donors and

C_{60}- or C_{70}-based functionalized fullerenes), the selection of *type* and *amount* of solvent is important. Common solvents used in the fabrication of OSCs include chlorobenzene, dichlorobenzene, chloroform, toluene, and others. Each has different properties affecting their interaction with organic polymers including molecular structure, density, boiling point, solubility, and viscosity. After the active layer materials are mixed in, matters become even more complicated. Depending on the *ratio* of donor-to-acceptor polymers and their *concentration* in the solvent in which they are dissolved, viscosity will change. Standard procedure is to magnetically stir the active layer blend on a hot plate for at least 24 hours. The stirring time and temperature setting are parameters that will determine the homogeneity of the mixture to be spin-cast on top of the PEDOT:PSS. Again, filtering the active layer blend can remove agglomerations that might lead to charge carrier traps, shorting, and decreased current density. Spin-casting active layers is similar to the method used for PEDOT, but with some critical differences. Active layer blends must be spun in an inert environment (e.g., N_2- or Ar-filled glove box) to ensure O_2 and H_2O are not incorporated within the thin film. Otherwise, these "contaminants" form recombination sites that adversely impact device performance and PCE. The spin parameters – acceleration/terminal speed and spin time – must also be tailored to the specific donor/acceptor/solvent combination. These tend to be slower and shorter, respectively, due to the blend viscosity and higher evaporation rates of organic solvents compared to the water-based PEDOT:PSS.

As before, annealing is a necessary step required to improve the crystallinity of the active layer – at least in HBG polymers like P3HT. Such is not necessarily the case for some LBG polymers where annealing can actually collapse J_{SC} and FF. So, tradeoffs

are required when fabricating tandem solar cells comprised of both LBG and HGB polymers. When annealing of a polymer blend that will be in direct contact with the electrode is called for, it's important that this step take place *after* the metallic cathode material is applied. This has to do with interfacial characteristics between the polymer and the metal. The surface of the polymer presents a certain level of roughness that effectively *increases* with annealing. This is relevant when one considers that the back electrode (normally an aluminum cathode), serves not only as a collector of electrons, but also as an internal light reflector. Light that traverses the entire depth of the OSC device to the cathode is bounced back into the active layer at the multi-faceted active layer/cathode interface where there is a possibility of increased exciton generation and current production. If the active layer is annealed prior to cathode deposition, the polymer morphs to a more crystalline structure with a rougher surface, but it is more difficult to deposit the Al cathode uniformly over all the contours. It is better to deposit the Al and then *post-anneal* the structure so that the cathode/active layer interface morphs simultaneously and maintains the greatest amount of contact between the two surface areas. When the mutual interfacial area is effectively smaller, there will be less electron collection and transport out of the device, less internal reflection, and ultimately decreased PCE.

The details just described apply both to single planar cells and also to tandem structures composed of two or more subcells. However, tandem configurations require additional layers that function as optical spacers, electron transporters, energy-state intermediates, and structural supports for the subcell components. Several different metal oxide species are used to perform these functions. For the purposes of this dissertation,

titanium oxide (TiOx), is analyzed in the simulations and incorporated in the fabrication of experimental cells. TiOx is produced via the sol-gel process and spin-cast on subcell components in tandem configurations. Figure 58 shows a schematic representation of the energy levels associated with the various component layers in a series tandem organic solar cell employing TiOx layers.

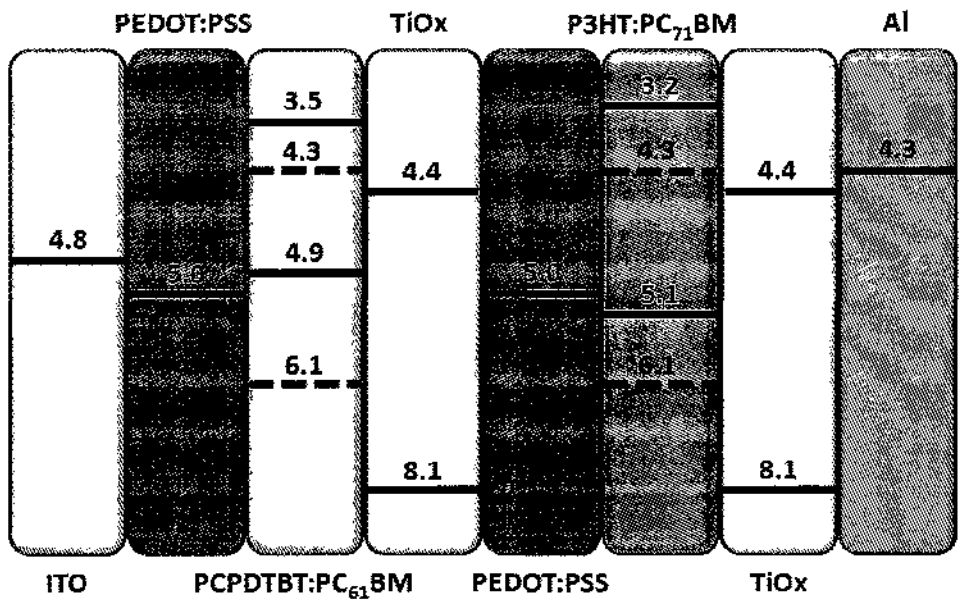

Figure 58. Tandem OSC energy level diagram for PCPDTBT:PC_{71}BM and P3HT:PC_{71}BM subcells. Energies are in eV. (based on [87]).

These nanoscale layers are also subject to the influences and constraints of fabrication steps such as concentration, spin parameters, and annealing. Perhaps the most difficult process step to manage is annealing. In a multi-junction configuration, the solar cell is built up layer by layer and each requires annealing at specific temperatures and for particular amounts of time. This means that several layers will be annealed more than

once and that can be problematic. Annealing for too long, or at too high a temperature can adversely impact FF and JSC characteristics. Requiring a series-tandem structure to undergo "serial-annealing" dictates that some known optimum parameters for individual layers be compromised. This is necessary in order to achieve an acceptable performance level for the OSC as a whole. The following section details the significance of thermal annealing and how it affects structural and optical properties in P3HT:$PC_{61}/_{71}$BM solar cells produced in our lab.

INFLUENCE OF ANNEALING ON POLYMER BLEND PROPERTIES

Atomic force microscopy and using a source meter to measure IV characteristics of organic solar cells gives excellent insight into the evolution of surface roughness and morphology as well as device electrical properties that result from thermal annealing. Following thermal treatment, AFM results show that P3HT:PC_{71}BM nanocomposites produce a more homogeneous mixture of finer grain size than that seen in P3HT:PC_{61}BM. Furthermore, stronger optical absorption in the visible region is observed in P3HT:PC_{71}BM compared to P3HT:PC_{61}BM. Since optical absorption is closely related to film crystallinity, it is inferred that P3HT:PC_{71}BM composites undergo more extensive crystallization upon annealing. Photoluminescence (PL) spectra of both active layer blends (each dissolved in chlorobenzene) show that each has excellent quenching effects and IV characterization shows that P3HT:PC_{71}BM registers higher current density under AM 1.5 illumination than does P3HT:PC_{61}BM. For the solar cells described in this particular experiment where device active areas measured ~12 mm^2, PCE was found to be approximately 33% better for C_{71}-based devices than for those made using C_{61} fullerene.

P3HT exhibits very strong optical absorption in the visible range [141], but $PC_{61}BM$ is notably poor in this region of the spectrum [93]. The low absorption of $PC_{61}BM$ can be attributed to the high degree of symmetry of C_{61} fullerene [68,93,142]. This suggests that the less symmetrical fullerene – $PC_{71}BM$ – enhances optical absorption in the visible region and correspondingly increases current densities in PV devices [93,142]. $PC_{71}BM$ has been used with other conjugated polymers and produced higher power conversion efficiencies than its more symmetrical counterpart [68,93,142]. However, there were no comparative studies on the effects of thermal annealing on structural and optical properties of P3HT:$PC_{61}BM$ and P3HT:$PC_{71}BM$ composites. As previously described, P3HT:PCBM blends are usually thermally treated to effect modification of structural and optical properties. In this experiment, P3HT:$PC_{61}BM$ and P3HT:$PC_{71}BM$ mixtures were annealed at 150 °C and their structural and electrical characteristics examined.

Films made from both blends were prepared inside a nitrogen glove box with O2 and H_2O levels maintained at less than 1 ppm. P3HT and PCBM were mixed in a 1:1 ratio, dissolved in chlorobenzene, and stirred overnight in the glove box at 40 °C. No sonication or filtering was used. Glass substrates were cleaned with acetone and isopropanol in an ultrasonic bath (10 min in each agent) and the thin films were prepared by spin-casting samples at 2000 rpm/500 rpm/s for 1 minute. Immediately after spin-casting, a subset of the prepared samples was annealed on a digital hotplate at 150 °C for 10 min inside the glove box. The thickness of annealed and non-annealed films was measured using a Dektak© Surface Profiler and found to be ~100 nm. These measurements were subsequently verified with AFM step height measurements.

Absorption spectra were measured using a Lambda© 2 S UV-Vis spectrophotometer with all films measured on absorption-corrected glass substrates.

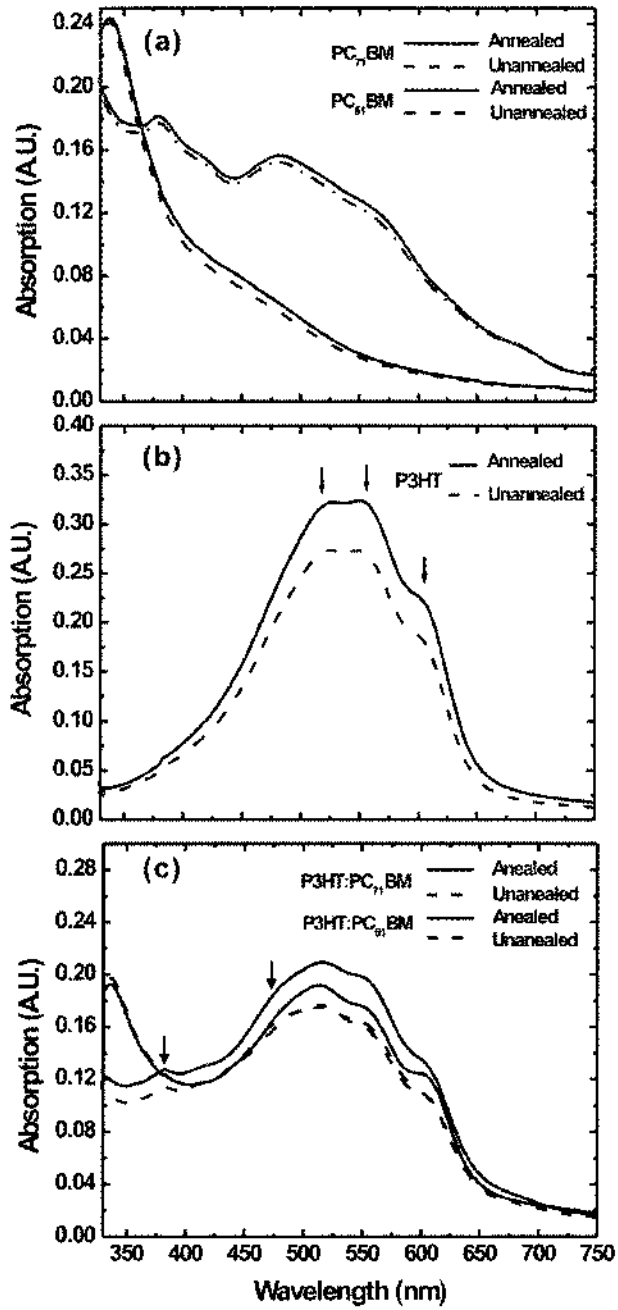

Figure 59. UV-Vis spectra of $PC_{61}BM$ and $PC_{71}BM$ before and after thermal annealing.

Surface morphologies were measured via AFM operated in tapping mode. All devices were structured identically: glass /ITO / PEDOT:PSS / P3HT:PC61BM or P3HT:PC71BM / Al. Following the post-annealing process, IV characterization was performed.

As previously discussed, the structure of C_{71} in $PC_{71}BM$ is less symmetrical than that of C_{61} in $PC_{61}BM$. So, to investigate the optical absorption properties of the composite blends, a UV-Vis spectrum was taken and compared to baseline data for $PC_{61}BM$, $PC_{71}BM$ and P3HT: $PC_{61}BM$ and P3HT: $PC_{71}BM$ samples. Figure 59 (a) shows the UV-Vis spectra of $PC_{61}BM$ and $PC_{71}BM$ before and after thermal treatment at 150 °C for 10 minutes in the glove box. Absorption for $PC_{61}BM$ is mostly located in the UV region with a maximum absorption peak at 349 nm while absorption in the visible region is much weaker. In contrast, $PC_{71}BM$ shows strong absorption in the visible portion of the spectrum where several shoulder peaks are observed and attributed to the less symmetrical structure of C_{71} [93]. $PC_{61}BM$ and $PC_{71}BM$ showed no significant change in absorption intensity before or after thermal annealing and this can also be seen in the Figure.

Figure 59 (b) and (c) show UV-Vis for P3HT, P3HT:$PC_{61}BM$ and P3HT:$PC_{71}BM$ before and after thermal annealing at 150 °C. For the P3HT films, the dominant absorption is located between 450 and 650 nm. Three distinct absorption peaks were observed at 520, 552, and 600 nm as indicated by the arrows in Figure 59 (b). After thermal annealing, a significant increase in the absorption bands was observed and is attributed to the increased crystalline ordering of the P3HT domains [143].

The absorption spectrum of P3HT:$PC_{61}BM$ films has two broad peaks; one ranges from 450 to 650 nm and originates from P3HT, and the second is located at 349 nm and is produced by $PC_{61}BM$. In comparison, P3HT:$PC_{71}BM$ films also show broad spectral absorption ranging from 450 to 650 nm, but have two additional peaks at 380 and 482 nm that originate from $PC_{71}BM$ as can be seen in Figure 59 (c). Before thermal treatment, P3HT:$PC_{61}BM$ and P3HT:$PC_{71}BM$ show almost the same intensity in the spectral range from 450 to 650 nm. As the spectral signature in this range originates from P3HT and the intensity of the shoulder peak at 600 nm is correlated to its degree of crystallinity as indicated by XRD data [143,144], it can be inferred that P3HT:$PC_{61}BM$ and P3HT:$PC_{71}BM$ films have almost the same degree of crystallinity before thermal treatment. However, after annealing only a slight increase in the intensity of the absorption band between 450 and 650 nm was observed for P3HT: $PC_{61}BM$ while much stronger enhancement is observed in the distinct vibronic absorption shoulders of P3HT:$PC_{71}BM$. The absorption peak at 600 nm in P3HT has a red-shift to 606 nm in P3HT:$PC_{61}BM$ and P3HT:$PC_{71}BM$ films. Since this absorption band represents the characteristic peak due to the π–π^* transition in the P3HT backbone [54] an increase in the absorption after thermal treatment indicates an enhanced ordering of P3HT chains [143,144]. Moreover, the enhanced intensity of the absorption spectra at 600 nm upon thermal annealing indicates a higher degree of crystallization or increased ordering of intra-chain interactions in P3HT materials [145]. Therefore, compared to P3HT:$PC_{61}BM$, annealed P3HT:$PC_{71}BM$ films present with an enhanced conjugated length and a more ordered P3HT crystalline structure.

The surface morphology of P3HT:PCBM films before and after thermal treatment was evaluated using AFM and is shown in Figure 60. The AFM images clearly show differing surface morphologies. The as-deposited, non-annealed films appear featureless with atomically flat surfaces; P3HT:$PC_{61}BM$ has surface roughness (root mean square (RMS)) of 0.33 nm and the value for P3HT:$PC_{71}BM$ is 0.45 nm (Figure 60 (a) and (d)). Upon annealing at 150 °C, film crystallinity increases [143,144,146]. The surface morphology of P3HT:$PC_{61}BM$ (Figure 60 (b)) shows increased roughness (RMS = 0.75 nm) compared to that of P3HT:$PC_{71}BM$ (RMS = 0.54 nm) as shown in Figure 60 (e).

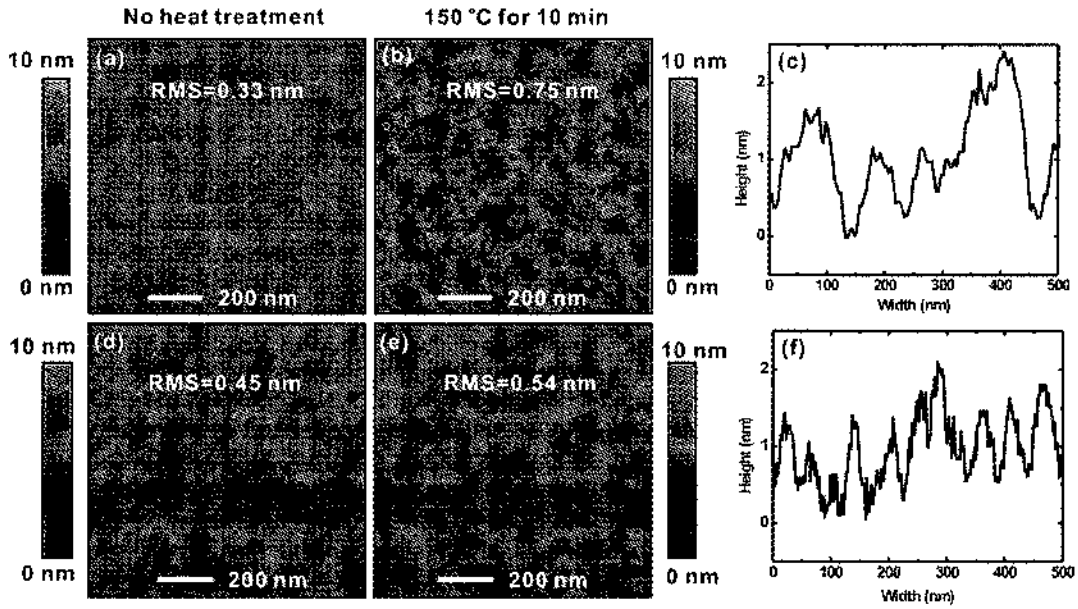

Figure 60. Surface morphologies of P3HT:$PC_{61/71}BM$ before and after thermal annealing.

Figure 60 (c) and (f) shows the comparison of grains of P3HT:$PC_{61}BM$ and P3HT:$PC_{71}BM$ where P3HT:$PC_{71}BM$ has more uniform mixing of constituents.

Thermal treatment of P3HT:PCBM composite films induces polymer reorganization and aggregation of PCBM that makes the thin-film structure more ordered [143,144,147]. However, a negative result of these morphological changes is that large grain features in P3HT:$PC_{61}BM$ can lead to a reduced charge collection rate at the electrodes. This is due to excessively long conduction path lengths compared to typical exciton diffusion lengths of ~10 nm [142]. Since clustering of P3HT:PCBM molecules with large grain features creates an inefficient conduction path from the conjugated polymer chains to the contact electrodes, charge carrier mobilities in conjugated polymers will be diminished and result in smaller photocurrent available necessary for efficient device operation. It's important to note that Wobkenberg *et al.*, have already shown that C_{71} and C_{61} fullerenes combined with regioregular polymers can have comparable electron mobilities [148]. Therefore, small grain features with enhanced crystallinity in P3HT:$PC_{71}BM$ films might offer better energy conversion efficiency.

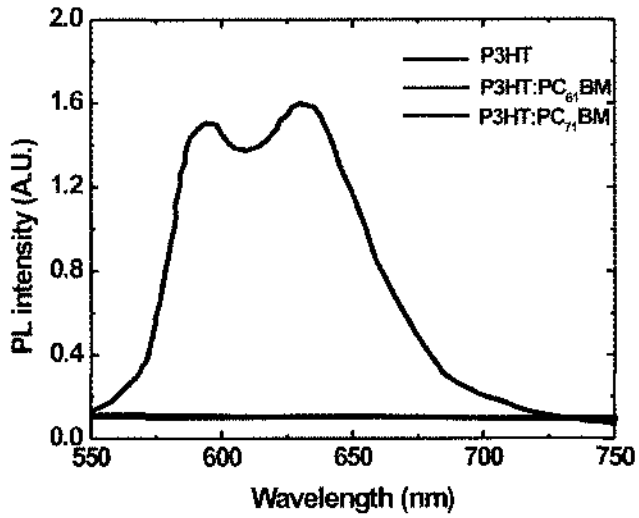

Figure 61. Photoluminescence spectra from P3HT, P3HT:$PC_{61}BM$, and P3HT:$PC_{71}BM$.

Photoluminescence spectra of chlorobenzene solutions of P3HT, P3HT:$PC_{61}BM$, and P3HT:$PC_{71}BM$ blends measured with 350 nm excitation are shown in Figure 61. The PL intensity of the P3HT solution drastically decreases in mixtures containing $PC_{61}BM$ and $PC_{71}BM$ thereby indicating strong quenching effects in complex solutions. Quenching in P3HT:PCBM complexes can be attributed to ultra-fast, photo-induced, donor–acceptor transfer interactions between excited polymers and the fullerene constituents in PCBM [149]. Therefore, both $PC_{61}BM$ and $PC_{71}BM$ are very efficient in transferring charge carriers.

To compare the relative efficiencies between P3HT:$PC_{61}BM$ and P3HT:$PC_{71}BM$, OPVs were fabricated and their IV characteristics measured under white light illumination using an Oriel© 100W solar illuminator equipped with an AM 1.5 filter. Our results indicate that short-circuit current (I_{SC}) shows much improvement in P3HT:$PC_{71}BM$ while the open circuit voltage is approximately the same for both at a value of 0.53 V. These results are consistent with those of other researchers as regards improved current densities up to 50% with $PC_{71}BM$-based polymer photovoltaic devices [93,142]. This improved photocurrent can be attributed to ultrafast carrier transfer, enhanced absorption across a wider range of the solar spectrum, and better crystallinity in P3HT:$PC_{71}BM$ nanocomposites following thermal annealing. Our experimental results indicate more than a 33% improvement in PCE with P3HT:$PC_{71}BM$ compared with P3HT:$PC_{61}BM$ as shown in Figure 62.

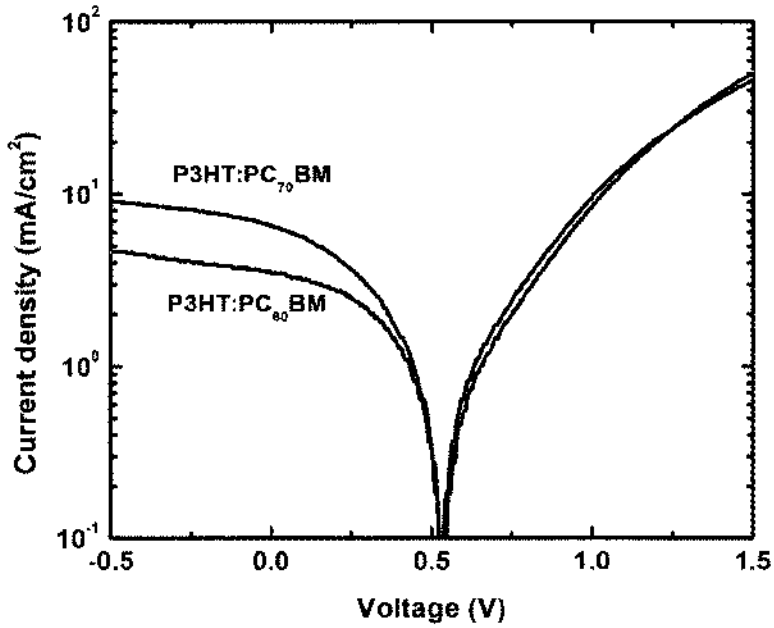

Figure 62. IV characteristics of the OSCs measured at 100 mW cm^2.

Efficiencies for the C_{61}-based and C_{71}-based cells were 0.6% and 0.8%, respectively. Short circuit currents measured 3.5 mA cm^{-2} for P3HT:PC_{61}BM and 6.4 mA cm^{-2} for P3HT:PC_{71}BM. For both devices generally, efficiencies were somewhat lower than expected because fabrication and characterization were not conducted in an oxygen-free environment.

These results show clearly the importance of thermal annealing. Highly-ordered P3HT polymer chains lead to better optical absorption in the visible region of the spectrum and this, in turn, helps to improve PCE. Uniform mixing of P3HT and $PC_{61/71}$BM and optimizing annealing protocols will certainly improve OSC performance, but the entire fabrication process is considerably more complicated. Some other aspects of the multi-step process include proper substrate preparation and cleaning, spin-casting techniques, and electrode deposition methods. These procedures are described in detail

in the appendices. Here, the procedures for fabricating single planar and tandem cells with incorporated TiOx layers are described.

FABRICATION OF P3HT:$PC_{61/71}$BM PLANAR SOLAR CELLS

Before cell production can begin, active layer material must be is prepared. P3HT (30 mg) and PC_{71}BM (21 mg) – a ratio of 1:0.7 – is mixed in 4 mL of chloroform and stirred in a sealed vial on a hot plate for 24 hours at 50°C. The stir speed is 200 RPM. After patterning and cleaning a substrate slide (see appendices for procedures), PEDOT:PSS is spin-cast at a terminal speed of 3000 RPM, acceleration of 500 RPM/s, and for a total time of three minutes. This length of time ensures the thin film layer will dry completely and not contract back on itself. Spinning takes place in atmosphere, but after removing the PEDOT from the anode portion of the slide it is placed inside a nitrogen glove box to anneal at 120°C for 10 minutes. It is then removed from the hot plate and allowed to cool to room temperature. Next, the active layer is spin cast on the slide inside the glove box; terminal speed is 1500 RPM, acceleration is 200 RPM/s, and the time is one minute. The slide is then removed from the glove box, the anode is again cleaned of polymer material, and the substrate is placed on the spinner (in atmosphere) ready for application of the TiOx layer. The solution-based metal oxide is spin-cast at 3000 RPM for 40 seconds. Again, the acceleration is 500 RPM/s. Immediately afterward, the anode is cleaned and the slide is placed on a hot plate in air and annealed for 10 minutes at 80°C. This step must be done in air so that the TiOx precursor can hydrolyze and form the amorphous oxide layer. The last deposition step is to place the solar cell in the electron beam evaporator (ebeam) and apply 80 nm of Al. After allowing the device to cool down under vacuum in the ebeam for 30 minutes, it is removed and

immediately placed inside the glove box for the final annealing step; 160°C for five minutes. Figure 63 shows a schematic of the completed device.

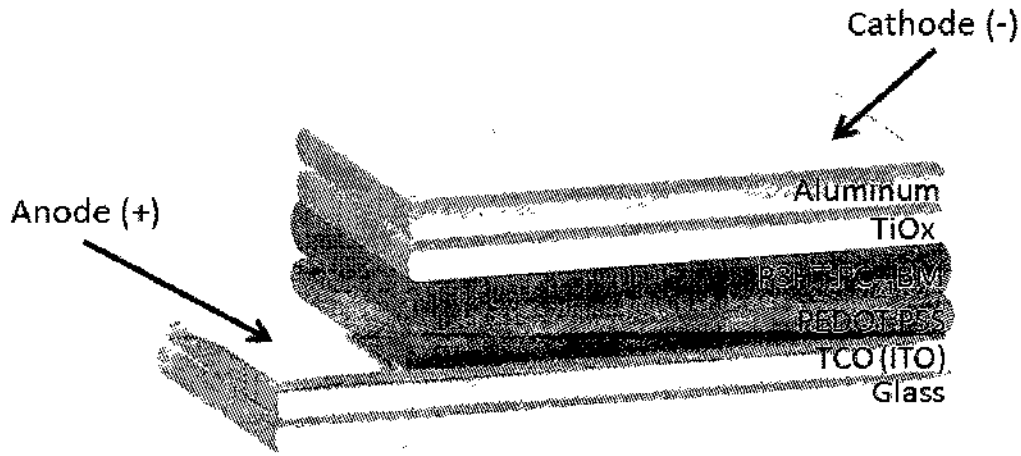

Figure 63. Schematic of P3HT:PC_{71}BM planar cell with TiOx optical spacer.

Figure 64 shows the IV curve for the P3HT:PC71BM solar cell with a TiOx optical spacer between the active layer and the Al cathode.

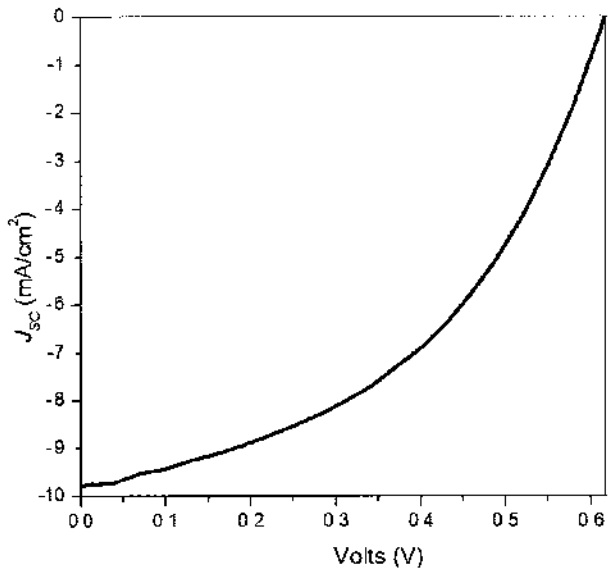

Figure 64. IV curve for P3HT:PC_{71}BM cell with TiOx layer.

The fill factor for this particular device is ~0.46 and the PCE is about 2.5%. With further optimization of the quality and thickness of the TiOx layer, efficiencies for this type of device will exceed that of its planar counterparts that lack this optical spacer.

FABRICATION OF PCPDTBT: $PC_{61/71}BM$ PLANAR SOLAR CELLS

Planar cells using the LBG polymer, PCPDTBT, can be made using very similar procedures to the ones described for P3HT: $PC_{61/71}BM$ in the previous section. First, the polymer blend is produced by mixing PCPDTBT (10 mg) and $PC_{61}BM$ (36 mg) in 2.5 mL of chlorobenzene. Note that this is in the ratio of 1:3.6. It is typical for successful LBG-based OSCs to require donor:acceptor polymer ratios to be between 1:3 and 1:4. The solution is stirred in a sealed vial on a hot plate for 24 hours at 50°C with a stir speed of 200 RPM. PEDOT:PSS is spin-cast on a clean/patterned substrate for three minutes after accelerating at 500 RPM/s to a terminal speed of 3000 RPM. Spinning again takes place in atmosphere, the PEDOT is removed from the anode, and the slide is placed inside a nitrogen glove box to anneal at 120°C for 10 minutes. After cooling to room temperature, the PCPDTBT:PCBM active layer is spin cast inside the glove box. This time, the terminal speed is 2000 RPM while the acceleration and time remain at 200 RPM/s and one minute, respectively. The reason for the increased speed is due to the higher molecular weight of the PCPDTBT molecules and smaller volume of solvent that combine to increase the viscosity of the blend. If the substrate is spun too slowly, the active layer will be too thick and excessive absorption will result in decreased J_{SC} and η. Following in order, the slide is removed from the glove box, the anode is cleaned, and the substrate is placed on the spinner for the TiOx layer to be applied in air. Spin parameters for TiOx are the same as for HBG polymers: terminal speed = 3000 RPM, acceleration =

500 RPM/s, and time = 40 seconds. Once completed, the anode is cleaned again and the slide placed on a hot plate in air to anneal for 10 minutes at 80°C. It is the H_2O in the ambient air that allows hydrolysis to take place and form the linkages between Ti and O that result in an amorphous, semi-crystalline TiOx matrix. This step cannot be done in an inert environment such as that found in an Ar or N_2 glove box. The penultimate step is the deposition of the 80 nm Al cathode via ebeam evaporation and a 30-minute cool down under vacuum to ensure there is no separation at the blend/electrode interface due to differing coefficients of thermal expansion. The final step is to place the completed cell in the glove box and perform the post-annealing step: 160°C for five minutes on a hot plate and then cooling to room temperature for subsequent characterization. The completed device is nearly identical to the one shown in Figure 63 with the exception of the LBG-based active layer.

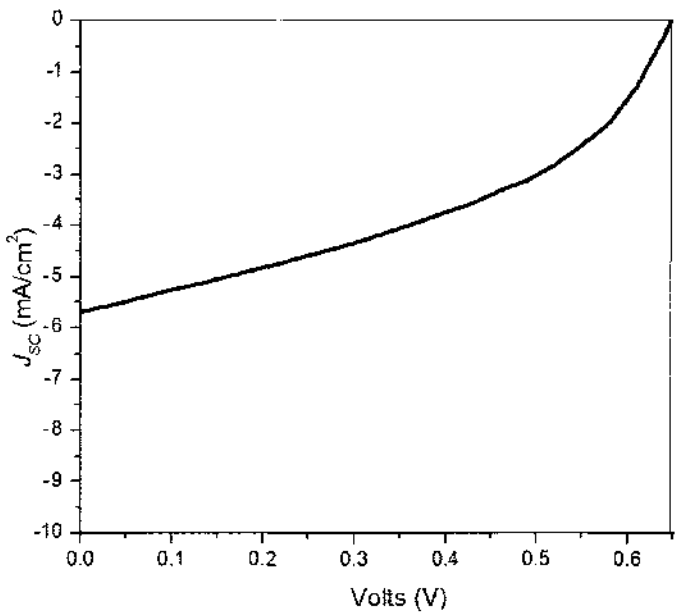

Figure 65. IV curve for PCPDTBT:$PC_{61}BM$ cell with TiOx layer.

Figure 65 shows the IV curve for the PCPDTBT:$PC_{61}BM$ solar cell with a TiOx optical spacer included. The fill factor is ~0.41 and the PCE is approximately 1.4%. The lower PCE and current density are not unusual for LBG polymers, and they do not rule out their use in OSCs – especially in tandem OSCs where they can be used in a complementary fashion with HGB subcells to harvest a wider portion of the visible spectrum.

Both LBG and HBG donor materials can be used in tandem solar cell structures, but the level of fabrication complexity goes up considerably. With an increasing number of device layers comes additional series and shunt resistance, greater absorption, and charge transport issues at the multiple interfaces. As can be seen in Figure 44 (Page 95), at least nine interface surfaces must be traversed by the light in a tandem cell configuration. However, if the technological obstacles can be overcome, tandem cells will achieve efficiencies in the 10% range and beyond.

FABRICATION OF P3HT:$PC_{61/71}BM$ & PCPDTBT: $PC_{61/71}BM$ TANDEM CELLS

The methods implemented in fabricating tandem solar cells are similar to those used for single planar cells, but additional device layers are required to function as supports between subcells and as charge carrier transport media. Merely combining subcells according to the procedures described in the previous two sections will not produce a series tandem cell with greater efficiency than either of those subcells. The entire fabrication process must be modified because of interactions between processing steps associated with individual cells that are not mutually exclusive when forming a tandem structure. For instance, the choice of solvents used to prepare the active layers must be considered. It's not possible to lay subcells made from the same solvent on top of each other. Dissimilar solvents must be used for adjacent subcells so that underlying

layers are not dissolved. More importantly, a "buffer" layer is required – and metal oxide layers show the most promise. Still, it's not possible to form a perfectly pristine metal oxide support/transport layer between subcells. Discontinuities will invariably exist that allow subsequent layers – in their liquid form – to filter through and attack underlying polymer blends. This will disrupt the integrity of the discrete layer system necessary to maintain carrier transport order between the spatially-dependent energy levels of each thin-film in the device. Despite this, sufficiently intact oxide layers can be deposited that fulfill the optical and electrical requirements necessary to be effective and still remain autonomous structurally – provided critical deposition and annealing steps are optimized. A series tandem cell was made with a PCPDTBT:$PC_{61}BM$ bottom subcell and P3HT:$PC_{71}BM$ in the top according to the following procedures:

- PEDOT:PSS – terminal speed = 3000 RPM, acceleration = 500 RPM/s, time = 3 minutes (first layer of the bottom subcell)
- Anneal for 10 minutes in air at 140°C for 10 minutes
- Spin-cast active layer in the glove box – terminal speed = 2000 RPM, acceleration = 500 RPM/s, time = 1 minute
- Spin-cast TiOx in air – 3000 RPM, 500 RPM/s, 40 seconds
- Anneal in air – 80°C, 10 minutes
- PEDOT:PSS – terminal speed = 3000 RPM, acceleration = 500 RPM/s, time = 3 minutes (this is the first layer of the top subcell)
- Place substrate on the hot plate in the glove box – 120°C for 10 minutes
- Spin-cast active layer in the glove box – terminal speed = 1500 RPM, acceleration = 200 RPM/s, time = 1 minute

- Spin-cast TiOx in air – 3000 RPM, 500 RPM/s, 40 seconds
- Anneal in air – 80°C, 10 minutes
- Deposit 80 nm of Al in ebeam and cool under vacuum for 30 minutes
- Post-anneal in the glove box – 160°C for 10 minutes

The final structure is represented in Figure 44 and the IV characteristic curve is shown in Figure 66. The V_{OC} is approximately 0.9 V – higher than either of the subcells when they are made as single planar cells. However, note the collapsed fill factor and diminished J_{SC}. This indicates problems with morphology that will certainly be due, at least in part, to the effects of *serial annealing*. The tandem fabrication process calls for five separate annealing steps which means that the PEDOT:PSS layer in the first subcell will be annealed five times, the PCPDTBT:$PC_{61}BM$ four times, the first TiOx layer three times, and so on. Successive heat treatments will have an adverse impact on the device parameters, so modifications to the fabrication process must be made. The V_{OC} is not the sum of the two subcells as it should be, but this is also due to the morphology problems that reduced FF and J_{SC}.

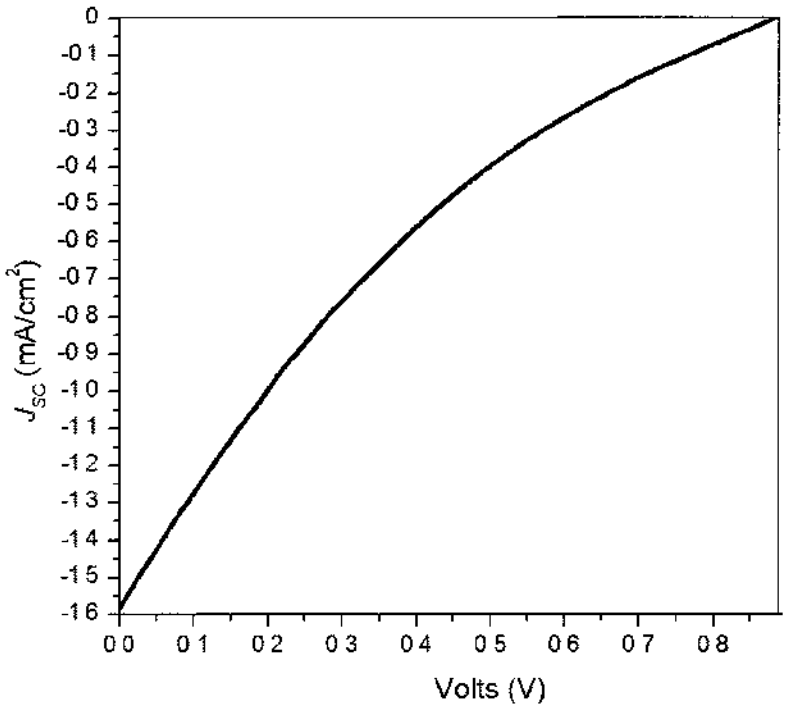

Figure 66. IV Curve: PCPDTBT: $PC_{61}BM$ (bottom) and P3HT:$PC_{71}BM$ (top) tandem solar cell.

As discussed, thermal annealing changes the morphology of active layer blends from an almost completely amorphous, two-phase arrangement to something that is semi-crystalline. Figure 60 (Page 133) showed the effects of annealing on P3HT:$PC_{61/71}BM$ composites where increased roughness and crystallinity were the result of heat treatment at 150°C. Figures 67, 68, and 69 show AFM images of annealed thin films composed of P3HT:$PC_{71}BM$, PCPDTBT:$PC_{71}BM$, and PCPDTBT:$PC_{61}BM$, respectively. In Figure 67, the surface is fairly smooth with an RMS roughness of 1.024 nm.

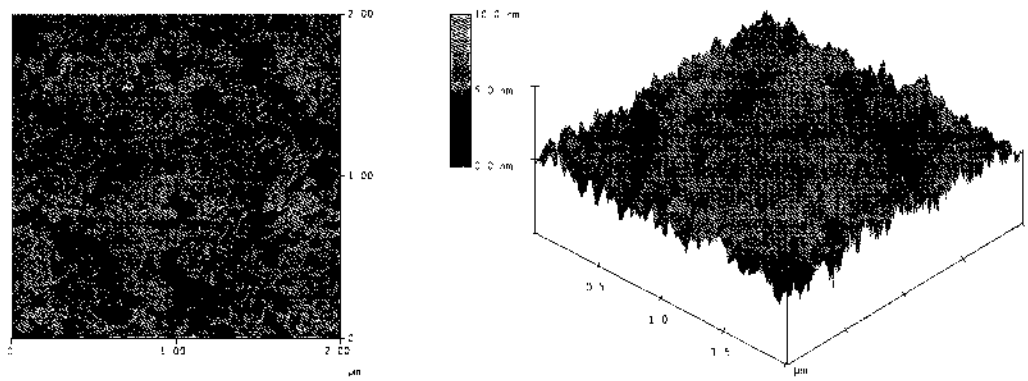

Figure 67. P3HT:$PC_{71}BM$ thin film after annealing for 10 minutes at 80°C.

In Figure 68, after a 10-minute thermal treatment at 80°C the RMS roughness is 1.447 nm – considerably larger than that for P3HT:$PC_{71}BM$. This may be due to steric hindrance between PCPDTBT and $PC_{71}BM$ because of PCPDTBT's larger size compared to P3HT and its interaction with $PC_{71}BM$. Raised areas are seen on the surface of the film. These result from $PC_{71}BM$ agglomeration. The PCPDTBT:$PC_{71}BM$ ratio is 1:3.6 compared to 1:0.7 used for the P3HT:$PC_{71}BM$ mixture seen in Figure 67.

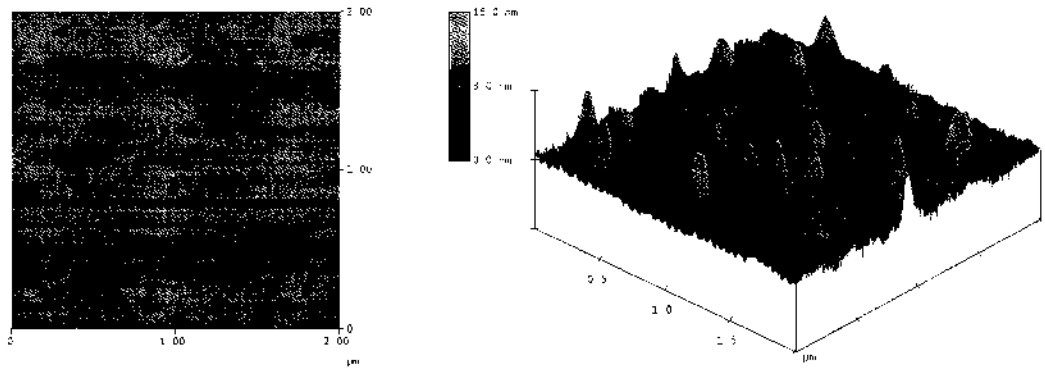

Figure 68. PCPDTBT:$PC_{71}BM$ thin film after annealing for 10 minutes at 80°C.

A PCPDTBT:$PC_{61}BM$ thin film is shown in Figure 69. RMS roughness is ~1.0 nm and again, there are raised areas covering the surface where $PC_{61}BM$ has formed clusters due to the annealing process.

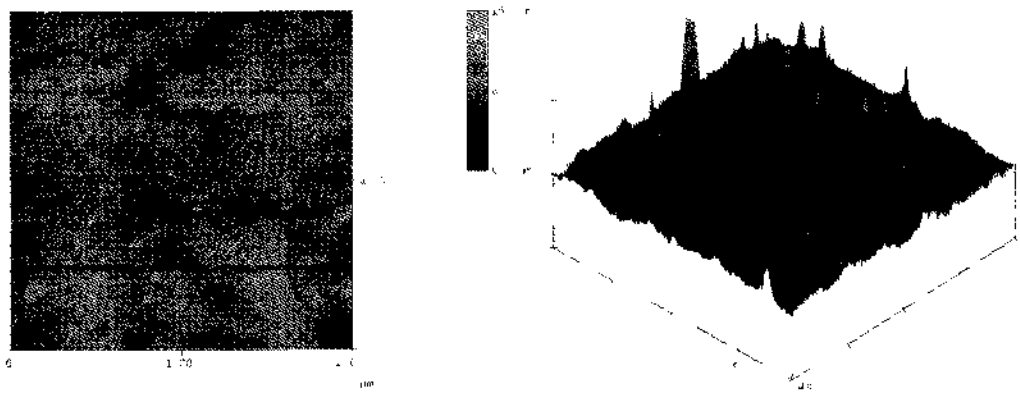

Figure 69. PCPDTBT:$PC_{61}BM$ thin film after annealing for 10 minutes at 80°C.

Note that the roughness is comparable to that observed with P3HT:$PC_{71}BM$. This may be due to the fact the $PC_{61}BM$ clusters are smaller than those found in the PCPDTBT:$PC_{71}BM$ thin films and therefore don't have as dramatic an impact on overall surface roughness. Still, these coagulation points are problematic as they form unwanted charge carrier recombination centers. Since annealing is such a critical step in OSC fabrication, forming multijunction, tandem cells becomes considerably more challenging. Also, it's clear concentration effects and donor:acceptor ratios have an impact on layer morphology and therefore, device performance. Increased concentrations have the effect of darkening the active layers thereby decreasing absorption. Higher donor:acceptor concentrations for a given amount of solvent increase the individual layer opacity and this can be tremendously deleterious in tandem configurations. A representative sample

of OSCs fabricated using varied concentrations of HBG and LBG polymers is shown in Figure 70.

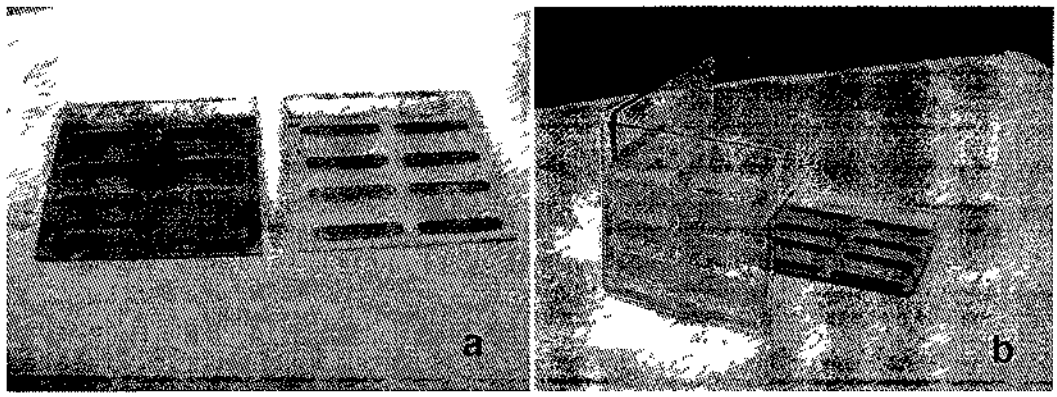

Figure 70. Varied coloration of donor:acceptor blends impacts absorption: (a) HBG P3HT:$PC_{61}BM$ (left), and LBG PCPDTBT:$PC_{61}BM$ (right), and (b) P3HT:PCBM-based cells in different volumes of solvent.

Much more experimentation must be accomplished to find the best methods for correcting the aforementioned problems as they apply to tandem solar cell production. Some possible remedies include lowering annealing temperatures, annealing fewer times, room temperature cooling of layers under ultrasonic stimulation, and optimization (which may be different from that for single planar solar cells) of donor:acceptor concentrations to avoid excessive absorption resulting from opacity. Other techniques may be to deposit the metal oxide spacers via thermal or ebeam evaporation rather than using a solution-based approach. Finally, the development of new polymers that are not sensitive to the effects of thermal treatments could greatly simplify the entire OSC production process.

CHAPTER V

CONCLUSION AND FUTURE WORK

CONCLUSION

As the world's demand for energy continues to increase, more effort and resources must be expended to advance the state-of-the-art in renewable energy technologies. Solar-based technologies will undoubtedly play a large part in replacing fossil fuel-based sources, but only after significant improvements are made in performance and efficiency. A primary focus of research is organic photovoltaics and significant progress is being made – especially in the area of hybrid inorganic/organic tandem solar cells. These devices have the potential to achieve power conversion efficiencies in the 10% range which would make large scale production practical, cost effective, and commercially viable. Eventually, organic photovoltaics will be ubiquitous. This dissertation describes the feasibility of improving an already promising photovoltaic application – hybrid tandem cells. Simulations of several tandem combinations were conducted that show higher efficiencies are possible when the appropriate HBG/LBG donors are combined with energetically-comparable acceptor fullerene derivatives. Further enhancements are possible when subcell components are placed in the proper sequence to achieve the greatest absorption. Verification of these results is currently being pursued in the lab. Fabrication of such cells remains technologically challenging, and more research must be done to overcome obstacles associated with concatenating multi-layer subcell components while maintaining their individual performance capabilities. Additional structural modifications as well as the introduction of new

polymer materials capable of harvesting more of the solar spectrum may provide the answers to these issues. Research efforts continue both in industry and in academia to address the current limitations impeding greater and more rapid increases in OSC efficiency.

FUTURE WORK

With a view toward making OPV device improvements via structural changes, an active area of research strives to significantly improve energy conversion efficiencies through the exploration and manipulation of novel device physical structures. With knowledge gleaned from the fabrication of standard planar and hybrid inorganic/organic tandem solar cells, our group has developed a technique for furthering the concepts behind multi-junction solar cells by creating nanoscale nested structures capable of accommodating organic photoactive material that will serve as a light-absorbing layer in OSCs. The fabrication methodology for these nanostructures calls for the formation of alternating sacrificial spacers in a nested nanotube configuration. The technique employs highly-ordered macroporous silicon templates that are used as the supporting structure and bottom contact for concentrically-nested metal oxide cylinders.

Atomic Layer Deposition (ALD) provides the means for precision control of layer parameters within the Si template. This deposition method provides excellent uniform coverage deep within the template pores and is a highly-precise and repeatable process. The effective area of the nanoelectrodes is tailored to allow for maximum incorporation of organic materials within the structures. In particular, the thickness, spacing, and height of the nanostructures are controlled non-lithographically to a very high degree of precision [150]. The current state of our technology allows the Si substrate to be recessed

in such a way that the nested nanotubes protrude above the surface by a few micrometers. These structures are anchored by either TiO_2 or HfO_2 spines for stability. Subsequently, organic material (i.e., BHJ RR-P3HT and $PC_{61}BM/PC_{71}BM$ organic blends) are incorporated into the concentrically-nested nanotube voids created by the sacrificial spacer layers. Incorporation of organic material within the nanotube voids can be challenging, but we have demonstrated the feasibility as can be seen in the SEM cross-section of Figure 71. This particular step will likely become more difficult as void size decreases.

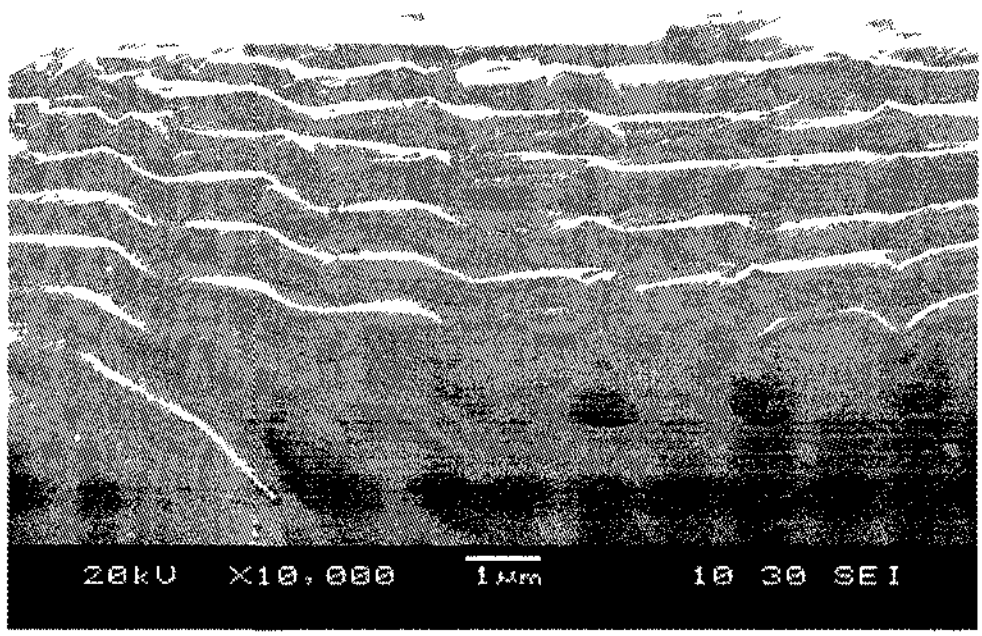

Figure 71. SEM micrograph revealing infiltration of photoactive organic blends of P3HT:PCBM into 1.0 μm (diameter) pores of an Si template. Infiltration is to a depth of ~5 μm.

The final step in the process involves applying a transparent conducting electrode to the top of the device and various methods are currently being explored.

With further development, these hybrid organic/inorganic structures could be used to develop more advanced multi-junction solar cells with enhanced performance characteristics. The technological obstacles will be many, but the rewards great if leaps in OSC efficiency are realized.

REFERENCES

[1] "Renewable Energy Technology Resource Maps for the United States," in *Renewable Energy Atlas*, published by National Renewable Energy Laboratory (NREL), August, 2009.

[2] "BP Statistical Review of World Energy June 2011," in *Statistical Review of World Energy*, published by British Petroleum (BP), June, 2011.

[3] M.C. Scharber, D. Muhlbacher, M. Koppe, P. Denk, C. Waldauf, A.J. Heeger, and C.J. Brabec, "Design rules for donors in bulk-heterojunction solar cells – towards 10% energy conversion efficiency," *Advanced Materials*, vol.18, (2006), pp. 789–794.

[4] G. Dennler, M.C. Scharber, T. Ameri, P. Denk, K. Forberich, C. Waldauf, and C.J. Brabec, "Design rules for donors in bulk-heterojunction tandem solar cells – towards 15% energy-conversion efficiency," *Advanced Materials*, vol. 20, (2008), pp. 579–583.

[5] "Geothermal Technologies," in *Energy Efficiency and Renewable Energy*, published by United States Department of Energy (USDOE), August, 2011.

[6] "Ocean Energy Technologies," in *Energy Efficiency and Renewable Energy*, published by United States Department of Energy (USDOE), August, 2011.

[7] "Wind Energy," in *Research and Technology*, published by Renewable Energy World, August, 2011.

[8] "Biomass Technologies," in *Energy Efficiency and Renewable Energy*, published by United States Department of Energy (USDOE), August, 2011.

[9] "Hydropower," in *Research and Technology*, published by Renewable Energy World, August, 2011.

[10] "Hydrogen Technologies," in *Energy Efficiency and Renewable Energy*; published by United States Department of Energy (USDOE), September, 2011.

[11] "Hydrogen Energy," in *Research and Technology*, published by Renewable Energy World, August, 2011.

[12] "Types of Renewable Energy," in *Research and Technology*, published by Renewable Energy World, August, 2011.

[13] "Types of Solar Energy," in *Research and Technology*, published by Renewable Energy World, September, 2011.

[14] F. C. Krebs, Ed., "Introduction," in *Polymer Photovoltaics: A Practical Approach*, Bellingham, WA: SPIE, 2008, pp. 2-3.Bellingham, WA: SPIE, 2008, pp. 2-3.

[15] "Renewables 2011, Global Status Report," in *Global Status Report*, published by Renewable Energy Policy Network for the 21st Century, September, 2011.

[16] R. Williams, "Becquerel Photovoltaic Effect in Binary Compounds," *Journal of Chemical Physics*, vol. 32, (1960), pp. 1505-1514.

[17] "Photovoltaic (solar cell) Systems," in *Research and Technology*, published by Renewable Energy World, September, 2011.

[18] Standard solar spectra for space and terrestrial use based on solar irradiance data published by National Renewable Energy Laboratory (NREL), September, 2011.

[19] "Solar Radiation Research," in *Science and Technology*, published by National Renewable Energy Laboratory (NREL), March 2009.

[20] F. C. Krebs, Ed., "Characterization of Organic Solar Cells," in *Polymer Photovoltaics: A Practical Approach*, Bellingham, WA: SPIE, 2008, pp. 92-93.

[21] R. Po, M. Maggini, and N. Camaioni, "Polymer solar cells: recent approaches and achievements," *Journal of Physical Chemistry C*, vol. 114, (2010), pp. 695–706.

[22] H. Akamatu, H. Inokuchi, and Y. Matsunaga, "Electrical Conductivity of the Perylene–Bromine Complex," *Nature*, vol. 173, (1954), pp. 168-169.

[23] C. Diebel and V. Dyakonov, "Polymer-fullerene bulk heterojunction solar cells," *Reports on Progress in Physics*, vol. 73, (2010), pp. 1-39.

[24] chemBlink Inc. (2011). *Methyl [6,6]-phenyl-C61-butyrate* [Online]. November 2011. Available from: http://www.chemblink.com/products/160848-22-6.htm. [Accessed: 14th November].

[25] chemBlink Inc. (2011). *[6,6]-Phenyl C71 butyric acid methyl ester* [Online]. November 2011. Available from: http://www.chemblink.com/products/609771-63-3.htm. [Accessed: 14th November 2011].

[26] F. C. Krebs, Ed., "Processing and Production of Large Modules," in *Polymer Photovoltaics: A Practical Approach*, Bellingham, WA: SPIE, 2008, pp. 266-267.

[27] V. Shrotriya, G. Li, Y, Yao, C.W. Chu, and Y. Yang, "Transition metal oxides as the buffer layer for polymer photovoltaic cells," *Applied Physics Letters*, vol. 88, (2006), pp. 073508-1-3.

[28] J.S. Huang, et al., "Solution-processed vanadium oxide as an anode interlayer for inverted polymer solar cells hybridized with ZnO nanorods," *Organic Electronics*, vol. 10, (2009), pp. 1060-1065.

[29] M.D. Irwin, D.B. Buchholz, A.W. Hains, R.P.H. Chang, and T.J. Marks, "p-type semiconducting nickel oxide as an efficiency-enhancing anode interfacial layer in polymer bulk-heterojunction solar cells," *Proceedings of the National Academy of Sciences of the United States of America*, vol. 105, no. 8, (2008), pp. 2783-2787.

[30] S. Han, et al., "Improving performance of organic solar cells using amorphous tungsten oxides as an interfacial buffer layer on transparent anodes," *Organic Electronics*, vol. 10, (2009), pp. 791-797.

[31] M.K. Siddiki, J. Li, D. Galipeau, and Q. Qiao, "A review of polymer multijunction solar cells," *Energy and Environmental Science*, vol. 3, (2010), pp. 867-883.

[32] Personal Communication with Prof. Lawrence L. Kazmerski, Executive Director, Science and Technology Partnerships, National Renewable Energy Laboratory (NREL), Golden, Colorado, September 16, 2011.

[33] J.Y. Kim, K. Lee, N.E. Coates, D. Moses, T.Q. Nguyen, M. Dante, and A.J. Heeger, "Efficient tandem polymer solar cells fabricated by all-solution processing", *Science*, vol. 317, (2007), pp. 222-225.

[34] B.V. Andersson, N.K. Persson, and O. Inganas, "Comparative study of organic thin film tandem solar cells in alternative geometries," *Journal of Applied Physics*, vol. 104, (2008), pp. 124508-1-6.

[35] G. Dennler, K. Forberich, T. Ameri, C. Waldauf, P. Denk, C.J. Brabec, K. Hingerl, and A.J. Heeger, "Design of efficient organic tandem cells: on the interplay between molecular absorption and layer sequence," *Journal of Applied Physics*, vol. 102, (2007), pp. 123109-1-6.

[36] X. Guo, et al., "Efficient tandem polymer photovoltaic cells with two subcells in parallel connection," *Organic Electronics*, vol. 10, (2009), pp. 1174-1177.

[37] X.W. Sun, et al., "Inverted tandem organic solar cells with a MoO3/Ag/Al/Ca intermediate layer," *Applied Physics Letters*, vol. 97, (2010), pp. 053303-1-3.

[38] S. S. Sun and N. S. Sariciftci, "Natural Organic Photosynthetic Solar Energy Transduction," in *Organic Photovoltaics: Mechanisms, Materials, and Devices*, Boca Raton, Taylor & Francis, 2005, ch. 3, sec. 3.2, pp. 38-43.

[39] S. S. Sun and N. S. Sariciftci, "Photovoltaic Cells Based on Nanoporous Titania Films," in *Organic Photovoltaics: Mechanisms, Materials, and Devices,* Boca Raton, Taylor & Francis, 2005, ch. 12, sec. 12.4, p. 309.

[40] Y. Kim, et al., Multilayer organic solar cells with wet-processed polymeric bulk heterojunction film and dry-processed small molecule films," *Applied Physics Letters*, vol. 92, (2008), pp. 093306-1-3.

[41] H.Y. Chen, et al., Polymer solar cells with enhanced open-circuit voltage and efficiency," *Nature Photonics*, vol. 3, iss. 11, (2009), pp. 649-653.

[42] F. C. Krebs, Ed., "The Polymer Solar Cell," in *Polymer Photovoltaics: A Practical Approach*, Bellingham, WA: SPIE, 2008, p. 20.

[43] E. Hecht, *Optics, Fourth Edition*, Addison-Wesley, 2002, p. 50.

[44] P. Wurfel, "Photovoltaic principles and organic solar cells," *Chimia*, vol. 61, no. 12, (2007), pp. 770-774.

[45] S. Gunes, H. Neugebauer, and N.S. Sariciftci, "Conjugated polymer-based organic solar cells," *Chemical Reviews*, vol. 107, (2007), pp. 1324-1338.

[46] S. M. Sze, "Carrier Transport Phenomena," in *Semiconductor Devices: Physics and Technology,* New York: Wiley & Sons, 1985, ch. 1, sec. 2.1, pp. 33–34.

[47] R. Coehoorn, W.F. Pasveer, P.A. Bobbert, and M.A.J. Michels, "Charge carrier concentration dependence of the hopping mobility in organic materials with Gaussian disorder," *Physical Review B: Condensed Matter*, vol. 72, (2005), pp. 155206-1-20.

[48] R. Schmechel, "Gaussian disorder model for high carrier densities: theoretical aspects and application to experiments," *Physical Review B: Condensed Matter*, vol. 66, (2005), pp. 235206-1-6.

[49] W.F. Pasveer, et al., "Unified description of charge-carrier mobilities in disordered semiconducting polymers," *Physical Review Letters*, vol. 94, (2005), pp. 206601-1-4.

[50] S.V. Novikov, D.H. Dunlap, V.M. Kenkre, P.E. Parris, and A.V. Vannikov, "Essential role of correlations in governing charge transport in disordered organic materials," *Physical Review Letters*, vol. 81, (2005), pp. 4472-4475.

[51] A. Pivrikas, H. Neugebauer, and N. S. Sariciftci, "Charge carrier lifetime and recombination in bulk heterojunction solar cells," *IEEE Journal of Selected Topics in Quantum Electronics*, vol. 16, no. 6, (2010), pp. 1746-1758.

[52] L. Gui-Jun, et al., "The study of a new n/p tunnel recombination junction and its application in a-Si:H/μc-Si:H tandem solar cells," *Chinese Physics B*, vol. 18, iss. 4, (2009), pp. 1674-1678.

[53] F. C. Krebs, Ed., "The Polymer Solar Cell," in *Polymer Photovoltaics: A Practical Approach*, Bellingham, WA: SPIE, 2008, p. 19.

[54] H. Sirringhaus, et al., " Two-dimensional charge transport in self-organized, high-mobility conjugated polymers," *Nature*, vol. 401, (1999), pp. 685-688.

[55] S. Hugger, "Semicrystalline morphology in thin films of poly 3(-hexylthiophene)," *Colloidal Polymer Science*, vol. 282, (2004), pp. 932-938.

[56] R. Haberkorn and M.E. Michel-Beyerle, "Onsager's ion recombination model in one dimension," *Chemical Physics Letters*, vol. 23, no. 1, (1973), pp. 128-130.

[57] A. Pivrikas, et al., "Langevin recombination and space-charge-perturbed current transients in regiorandom poly(3-hexylthiophene)," *Physical Review B*, vol. 71, (2005), pp. 125205-1-9.

[58] A. Pivrikas, et al., "A review of charge transport and recombination in polymer/fullerene organic solar cells," *Progress in Photovoltaics: Research and Applications* , vol. 15, (2007), pp. 677-696.

[59] C.L. Braun, "Electric field assisted dissociation of charge transfer states as a mechanism of photocarrier production," *Journal of Chemical Physics*, vol. 80, (1984), pp. 4157-4161.

[60] P. Boland, et al., "Fiber Bragg grating multichemical sensor," *Proceedings: The International Society for Optical Engineering (SPIE)*, vol. 6371, (2006), pp. 637109 – 637109 – 11.

[61] M. Bennett, "TICs, TIMs, and Terrorists," in *Today's Chemist at Work*, published by American Chemical Society, April, 2003, pp. 21-25.

[62] L. Onsager, "Initial recombination of ions," *Physical Review*, vol. 54, (1938), pp. 554-557.

[63] P. Langevin, "Recherches sure les gaz ionisés," *Annales de Chimie et de Physique*, vol. 28, (1903), p. 433.

[64] L.J.A. Koster, E.C.P. Smits, V.D. Mihailetchi, and P.W.M. Blom, "Device model for the operation of polymer/fullerene bulk heterojunction solar cells," *Physical Review B: Condensed Matter*, vol. 72, (2005), pp. 085205-1–085205-9.

[65] G. Yu and A.J. Heeger, "Charge separation and photovoltaic conversion in polymer composites with internal donor/acceptor heterojunctions," *Journal of Applied Physics*, vol. 78, (1995), pp. 4510-4515.

[66] G. Yu, J. Gao, J.C. Hummelen, F. Wudl, and A.J. Heeger, "Polymer photovoltaic cells: enhanced efficiencies via a network of internal donor-acceptor heterojunctions," *Science*, vol. 270, (1995), pp. 1789-1791.

[67] J.J.M. Halls, C.A. Walsh, N.C. Greenham, E.A. Marseglia, R.H. Friend, S.C. Moratti, and A.B. Holmes, "Efficient photodiodes from interpenetrating polymer networks," *Nature*, vol. 376, (1995), pp. 498-500.

[68] J. Peet, J.Y. Kim, N.E. Coates, W.L. Ma, D. Moses, A.J. Heeger, and G. C. Bazan, "Efficiency enhancement in low-bandgap polymer solar cells by processing with alkane dithiols," *Nature Materials*, Vol. 6, (2007), pp. 497-500.

[69] R.N. Marks, J.J.M. Halls, D.D.C. Bradley, R.H. Friend, and A.B. Holmes, "The photovoltaic response in poly (p-phenylene vinylene) thin-film devices," *Journal of Applied Physics,* vol. 6, (1994), pp. 1379-1394.

[70] S. Barth and H. Bassler, "Intrinsic photoconduction in PPV-type conjugated polymers," *Physical Review Letters*, vol. 79, (1997), pp. 4445-4448.

[71] T. Stubinger, and W. Brutting, "Exciton diffusion and optical interference in organic donor-acceptor photovoltaic cells," *Journal of Applied Physics*, vol. 90, (2001), pp. 3632-3641.

[72] L.A. Pettersson, L.S. Roman, and O. Ingabas, "Modeling photocurrent action spectra of photovoltaic devices based on organic thin films," *Journal of Applied Physics*, vol. 86, (1999), pp. 487-496.

[73] H. Hoppe and N.S. Sariciftci, "Polymer solar cells," *Advanced Polymer Science*, vol. 214, (2008), pp. 1-86.

[74] T. Kietzke, "Recent advances in organic solar cells," *Advances in OptoElectronics*, vol. 2007, Article ID 40285, (2007), 15 pages.

[75] A.C. Mayer, S.R. Scully, B.E. Hardin, M.W. Rowell, and M.D. McGehee, "Polymer based solar cells," *Materials Today*, vol. 10, (2007), pp. 28-33.

[76] A. Moliton and J.M. Nunzi, "How to model the behaviour of organic photovoltaic cells," *Polymer International*, vol. 55, (2006), pp. 583-600.

[77] I.G. Valls and M.L. Cantu, "Vertically aligned nanostructures of ZnO for excitonic solar cells: a review," *Energy & Environmental Science*, vol. 2, (2009), pp. 19-34.

[78] B. Kraabel, J.C. Hummelen, D. Vacar, D. Moses, N.S. Sariciftci, A.J. Heeger, and F. Wudl, "Subpicosecond photoinduced electron transfer from conjugated polymers to functionalized fullerenes," *Journal of Chemical Physics*, vol. 104, (1996), pp. 4267-4273.

[79] K.M. Coakley, B.S. Srinivasan, J.M. Ziebarth, C. Goh, Y. Lie, and M.D. McGehee, "Enhanced hole mobility in regioregular polythiophene infiltrated in straight nanopores," *Advanced Functional Materials*, vol. 15, (2005), pp 1927-1932.

[80] M.S. Kim, B.G. Kim, and J. Kim, "Effective variables to control the fill factor of organic photovoltaic cells," *ACS Applied Material Interfaces*, vol. 1, no. 6, (2009), pp. 1264-1269.

[81] E. Vitoratos, et al., "Thermal degradation mechanisms of PEDOT:PSS," *Organic Electronics*, vol. 10, (2009), pp. 61-68.

[82] L. Cattin, et al., "MoO3 surface passivation of the transparent anode in organic solar cells using ultrathin films," *Journal of Applied Physics*, vol. 105, (2009), pp. 034507-1-7.

[83] F. Liu, S. Shao, X. Guo, Y. Zhao, and Z. Xie, "Efficient polymer photovoltaic cells using solution-processed MoO3 as anode buffer layer," *Solar Energy Materials and Solar Cells*, Article in Press, (2010).

[84] M. Batzill, K. Katsiev, and U. Diebold, "Tuning the oxide/organic interface: benzene on SnO2 (101)," *Applied Physics Letters*, vol. 85, no. 23, (2004), pp. 5766-5768.

[85] J. Boucle, P. Ravirajan, and J. Nelson, "Hybrid polymer-metal oxide thin films for photovoltaic applications," *Journal of Material Chemistry*, vol. 17, (2007), pp. 3141-3153.

[86] A. Duta, et al., "Nanostructured TiO2 for solar energy conversion", Semiconductor Conference, 2005. CAS 2005 Proceedings. 2005 International. vol. 2, (2005), pp. 267-270.

[87] J. Kim, et al., "New architecture for high-efficiency polymer photovoltaic cells using solution-based titanium oxide as an optical spacer," *Advanced Materials*, vol. 18, (2006), pp. 572-576.

[88] G. Li, V. Shrotriya, Y. Yao, and Y. Yang, "Investigation of annealing effects and film thickness dependence of polymer solar cells based on poly(3-hexylthiophene)," *Journal of Applied Physics*, vol. 98, (2005), pp. 043704-1 – 043704-5.

[89] A.J. Moule, J.B. Bonekamp, and K. Meerholz, "The effect of active layer thickness and composition on the performance of bulk-heterojunction solar cells," *Journal of Applied Physics*, vol. 100, (2006), pp. 094503-1 – 094503-7.

[90] M. Lenes, L.J.A. Koster, V.D. Mihailetchi, P.W.M. Blom, "Thickness dependence of the efficiency of polymer:fullerene bulk heterojunction solar cells," *Applied Physics Letters*, vol. 88, (2006), pp. 243502-1–243502-3.

[91] A.J. Moule and K. Meerholz, "Intensity-dependent photocurrent generation at the anode in bulk-heterojunction solar cells," *Applied Physics B*, vol. 92, (2008), pp. 209–218.

[92] T. Yamanari, T. Taima, J. Sakai, and K. Saito, "Highly efficient organic thin-film solar cells based on poly(3-hexylthiophene) and soluble C70 fullerene derivative," *Japanese Journal of Applied Physics*, vol. 47, (2008), pp. 1230-1233.

[93] M.M. Wienk, J.M. Kroon, W.J.H. Verhees, J. Knol, J.C. Hummelen, P.A. van Hall, and R.A.J. Janssen, "Efficient methano[70]fullerene/MDMO-PPV bulk heterojunction photovoltaic cells," *Angewandte Chemie International Edition*, vol. 42, (2003), pp. 3371-3375.

[94] Semiconducting Thin Film Optics Simulation Software (Fluxim AG, 2006).

[95] G. Dennler, M.C. Scharber, and C.J. Brabec, "Polymer-fullerene bulk-heterojunction solar cells," *Advanced Materials*, vol. 21, (2009), pp. 1323-1338.

[96] C. Deibel, A. Baumann, and V. Dyakonov, "Polaron recombination in pristine and annealed bulk heterojunction solar cells," *Applied Physics Letters*, vol. 93, (2008), 163303-1 – 163303-3.

[97] L.J.A. Koster, V.D. Mihailetchi, and P.W.M. Blom, "Bimolecular recombination in polymer/fullerene bulk heterojunction solar cells," *Applied Physics Letters*, vol. 88, (2006), pp. 052104-1 – 052104-3.

[98] C. Deibel, A. Baumann, A. Wagenpfahl, and V. Dyakonov, "Polaron recombination in pristine and annealed bulk heterojunction solar cells," *Synthetic Metals*, vol. 159, (2009), pp. 2345-2347.

[99] Y. Kim, S.A. Choulis, J. Nelson, D.D.C. Bradley, S. Cook, and J.R. Durrant, "Composition and annealing effects in polythiophene/fullerene solar cells," *Journal of Materials Science*, vol. 40, (2005), pp. 1371-1376.

[100] P. Boland, S.S. Sunkavalli, S. Chennuri, K. Foe, T. Abdel-Fattah, and G. Namkoong, "Investigation of structural, optical, and electrical properties of regioregular poly(3-hexylthiophene)/fullerene blend nanocomposites for organic solar cells," *Thin Solid Films*, vol. 518, (2010), pp. 1728-1731.

[101] A. Baumann, J. Lorrmann, C. Deibel, and V. Dyakonov, "Bipolar charge transport in poly(3-hexylthiophene)/methanofullerene blends: a ratio-dependent study," *Applied Physics Letters*, vol. 93, (2008), pp. 252104-1–252104-3.

[102] F.C. Krebs, "Fabrication and processing of polymer solar cells: a review of printing and coating techniques," *Solar Energy Materials and Solar Cells*, vol. 93, (2009), pp. 394–412.

[103] T. Kuwabara, J. Sugiyama, T. Yamaguchi, and K. Takahashi, "Inverted type bulk-heterojunction organic solar cell using electrodeposited titanium oxide thin films as electron collector electrode," *Thin Solid Films*. vol. 517, (2009), pp. 3766–3769.

[104] W. Ma, C. Yang, X. Gong, K. Lee, and A.J. Heeger, "Thermally stable, efficient polymer solar cells with nanoscale control of the interpenetrating network morphology," *Advanced Functional Materials*, vol. 15, (2005), pp. 1617–1622.

[105] F. Padinger, R. Rittberger, and N.S. Sariciftci, "Effects of post-production treatment on plastic solar cells," *Advanced Functional Materials*, vol. 13, (2003) pp. 85–88.

[106] G. Li, V. Shrotriya, J. Huang, Y. Yao, T. Moriarty, K. Emery, and Y. Yang, "High-efficiency solution processable polymer photovoltaic cells by self-organization of polymer blends, *Nature Materials*, vol. 4, (2005), pp. 864–868.

[107] Y. Kim, S. Cook, S.M. Tuladhar, S.A. Choulis, J.Nelson, J.R. Durrant, D.D.C. Bradley, M. Giles, I. Mcculloch, C.S. Ha, and M. Ree, "A strong regioregularity effect in self-organizing conjugated polymer films and high-efficiency polythiophene:fullerene solar cells," *Nature Materials*, vol. 5, (2006) pp. 197–203.

[108] T. Yamanari, T. Taima, J. Sakai, and K. Saito, "Origin of the open-circuit voltage of organic thin-film solar cells based on conjugated polymers," *Solar Energy Materials and Solar Cells*, vol. 93, (2009), pp. 759–761.

[109] B.P. Rand, D.P. Burk, and S.R. Forrest, "Offset energies at organic semiconductor heterojunctions and their influence on the open-circuit voltage of thin-film solar cells," *Physical Review B: Condensed Matter*, vol. 75, (2007), pp. 115327-1–115327-11.

[110] C. Soci, I.W. Hwang, D. Moses, Z. Zhu, D. Waller, R. Gaudiana, C.J. Brabec, and A.J. Heeger, "Photoconductivity of a low-bandgap conjugated polymer," *Advanced Functional Materials*, vol. 17, (2007), pp. 632–636.

[111] M. Morana, M. Wegscheider, A. Bonanni, N. Kopidakis, S. Shaheen, M. Scharber, Z. Zhu, D. Waller, R. Gaudiana, and C. Brabec, "Bipolar charge transport in PCPDTBT-PCBM bulk-heterojunctions for photovoltaic applications," *Advanced Functional Materials*, vol.18, (2008), pp. 1757–1766.

[112] D. Muhlbacher, M. Scharber, M. Morana, Z. Zhu, D. Waller, R. Gaudiana, and C. Brabec, "High Photovoltaic performance of a low-bandgap polymer," *Advanced Materials*, vol. 18, (2006), pp. 2884–2889.

[113] J. Valenzuela, and S. Mil'shtein, "Quantum well model of a conjugated polymer heterostructure solar cell," *Microelectronics Journal*, vol. 40, (2009), pp. 424–426.

[114] I.W. Hwang, C. Soci, D. Moses, Z. Zhu, D. Waller, R. Gaudiana, C.J. Brabec, and A.J. Heeger, "Ultrafast electron transfer and decay dynamics in a small bandgap bulk heterojunction material," *Advanced Materials*, vol.19, (2007), pp. 2307–2312.

[115] O.S. Heavens, in: Optical Properties of Thin Solid Films, Dover Publications, New York, (1991), pp.69–80.

[116] G.R. Fowles, in: Introduction to Modern Optics, Dover Publications, New York, (1989), pp. 96–102.

[117] A. Gerrard and J.M. Burch, in: Introduction to Matrix Methods in Optics, Dover Publications, New York, (1994), pp.35–39.

[118] A.G. FLUXiM, in: Semiconducting Thin Film Optics Simulation Software, FLUXiM AG, Zurich, (2006), pp.43–54.

[119] M.M. Mandoc, L.J.A. Koster, and P.W.M. Blom, "Optimum charge carrier mobility in organic solar cells," *Applied Physics Letters*, vol.90, (2007), pp. 133504-1–133504-3.

[120] G.A. Buxton and N. Clarke, "Computer simulation of polymer solar cells," *Modelling and Simulation in Materials Science and Engineering*, vol. 15, (2007), pp. 13–26.

[121] P.K. Watkins, A.B. Walker, and G.L.B. Verschoor, "Dynamical Monte Carlo modeling of organic solar cells: the dependence of internal quantum efficiency on morphology," *Nano Letters*, vol. 5, (2005), pp. 1814–1818.

[122] F.C. Krebs, et al., "A round robin study of flexible large-area roll-to-roll

processed polymer solar cell modules," *Solar Energy Materials and Solar Cells*, vol. 93, (2009), pp. 1968–1977.

[123] F.C. Krebs, T.D. Nielsen, J. Fyenbo, M. Wadstrom, and M.S. Pedersen, "Manufacture, integration, and demonstration of polymer solar cells in a lamp for the ''Lighting Africa'' initiative," *Energy & Environmental Science*, vol. 3, (2010), pp. 512–525.

[124] H. Hoppe and N.S. Sariciftci, "Organic solar cells: an overview," *Journal of Materials Research*, vol. 19, (2004), pp.1924 –1945.

[125] D.W. Sievers, V. Shrotriya, and Y. Yang, "Modeling optical effects and thickness dependent current in polymer bulk-heterojunction solar cells," *Journal of Applied Physics*, vol. 100, (2006), pp. 114509-1 – 114509-7.

[126] C.M. Martin, V.M. Burlakov, and H.E. Assender, "Modeling charge transport in composite solar cells," *Solar Energy Materials and Solar Cells*, vol. 90, (2006), pp. 900-915.

[127] F. Monestier, J.J. Simon, P. Torchio, L. Escoubas, F. Flory, S. Bailly, R. de Bettignies, S. Guillerez, and C. Defranoux, "Modeling the short-circuit current density of polymer solar cells based on P3HT:PCBM blend," *Solar Energy Materials and Solar Cells*, vol. 91, (2007), pp. 405–410.

[128] T. Ameri, G. Dennler, C. Lungenschmied, and C.J. Brabec, "Organic tandem solar cells: a review," *Energy & Environmental Science*, vol. 2, (2009), pp. 347–363.

[129] M. Helgesen, R. Sondergaard, and F.C. Krebs, "Advanced materials and processes for polymer solar cell devices," *Journal of Materials Chemistry*, vol. 20, (2010), pp. 36–60.

[130] G. Namkoong, P. Boland, K. Lee, and J. Dean, "Design of organic tandem solar cells using PCPDTBT:$PC_{61}BM$ and P3HT:$PC_{71}BM$," *Journal of Applied Physics*, vol. 107, (2010), 124515-1 – 124515-6.

[131] J.J. Benson-Smith, L. Goris, K. Vandewal, K. Haenen, J.V. Manca, D. Vanderzande, D.D.C. Bradley, and J. Nelson, "Formation of a ground-state charge-transfer complex in polyfluorene/[6,6]-phenyl-C61 butyric acid methyl ester (PCBM) blend films and its role in the function of polymer/PCBM solar cells," *Advanced Functional Materials*, vol. 17, (2007), pp. 451–457.

[132] P. Boland, K. Lee, and G. Namkoong, "Device optimization in PCPDTBT:PCBM plastic solar cells," *Solar Energy Materials and Solar Cells*, vol. 94, (2010), pp. 915–920.

[133] P. Boland and G. Namkoong, "Optimization of active layer thickness in planar organic solar cells via optical simulation methods," *Japanese Journal of Applied Physics*, vol. 49, (2010), pp. 030205-1 – 030205-3.

[134] V.D. Mihailetchi, H. Xie, B. de Boer, L.J.A. Koster, and P.W.M. Blom, "Charge transport and photocurrent generation in poly(3-hexylthiophene):methanofullerene bulk-heterojunction solar cells," *Advanced Functional Materials*, vol. 16, (2006), pp. 699–708.

[135] A. Hadipour, B. de Boer, and P.W.M. Blom, "Organic tandem and multi-junction solar cells," *Advanced Functional Materials*, vol. 18, (2008), pp. 169-181.

[136] A. Hadipour, B. de Boer, and P.W.M. Blom, "Device operation of organic tandem solar cells," *Organic Electronics*, vol. 9, (2008), pp. 617-624.

[137] M. Lenes, M. Morana, C.J. Barbec, and P.W.M. Blom, "Recombination-limited photocurrents in low bandgap polymer/fullerene solar cells," *Advanced Functional Materials*, vol. 19, (2009), pp. 1106-1111.

[138] S. S. Sun and N. S. Sariciftci, "The Influence of the Electrode Choice on the Performance of Organic Solar Cells," in *Organic Photovoltaics: Mechanisms, Materials, and Devices,* Boca Raton, Taylor & Francis, 2005, ch. 20, sec. 20.3.1, pp. 459-467.

[139] P. Peumans, A. Yakimov, and S.R. Forrest, "Small molecular weight organic thin-film photodetectors and solar cells," *Journal of Applied Physics*, vol. 93, (2003), pp. 3693-3723.

[140] J.C. Hummelen, J. Knol, and L. Sanchez, "Stability issues of conjugated polymer/fullernce solar cells from a chemical viewpoint," *Procedures of the SPIE*, vol. 4108, "Organic Photovoltaics," edited by Z. Kafafi, SPIE, Bellingham, WA, 2001, pp. 76-84.

[141] G. Janssen, A. Aguirre, E. Goovaerts, P. Vanlaeke, J. Poortmans, and J. Manca, "Optimization of morphology of P3HT/PCBM films for organic solar cells: effects of thermal treatments and spin coating solvents," *European Physical Journal Applied Physics*," vol. 37, (2007), pp. 287-290.

[142] Y. Yao, C. Shi, G. Li, V. Shrotriya, Q. Pai, and Y. Yang, "Effects of C70 derivative in low band gap polymer photovoltaic devices: spectral complementation and morphology optimization," *Applied Physics Letters*, vol. 89, (2006) pp. 153507-1 – 153507-3.

[143] T. Erb, U. Zhokhavets, H. Hoppe, G. Gobsch, M. Al-Ibrahim, and O. Ambacher, "Absorption and crystallinity of poly(3-hexylthiophene)/fullerene blends in

dependence on annealing temperature," *Thin Solid Films*, vols. 511–512, (2006), pp.483-485.

[144] U. Zhokhavets, T. Erb, G. Gobsch, M. Al-Ibrahim, and O. Ambacher, "Relation between absorption and crystallinity of poly(3-hexylthiophene)/fullerene films for plastic solar cells," *Chemical Physics Letters*, vol. 418, (2006), pp. 347-350.

[145] X. Jiang, R. Osterbacka, O. Korovyanko, C.P. An, B. Horowitz, R.A.J. Janssen, and Z.V. Vardeny, "Spectroscopic studies of photoexcitations in regioregular and regiorandom polythiophene films," *Advanced Functional Materials*, vol. 12, (2002), pp. 587-597.

[146] M.Campoy-Qiles, T. Ferenczi, T. Agostinelli, P.G. Etchegoin, Y. Kim, T.D. Anthopoulos, P.N. Stavrinou, D.D.C. Bradley, and J. Nelson, "Morphology evolution via self-organization and lateral and vertical diffusion in polymer:fullerene solar cell blends," *Nature Materials*, vol. 7, (2008), pp. 158-164.

[147] S.E. Shaheen, C.J. Brabec, N.S. Sariciftci, F. Padinger, T. Fromherz, and J.C. Hummelen, "2.5% efficient organic plastic solar cells," *Applied Physics Letters*, vol. 78, (2001), pp. 841-843.

[148] P.H. Wöbkenberg, D.D.C. Bradley, D. Kronholm, J.C. Hummelen, D.M. de Leeuw, M. Cölle, and T.D. Anthopoulos, "High mobility n-channel organic field-effect transistors based on soluble C60 and C70 fullerene derivatives," *Synthetic Metals*, vol. 158, (2008), pp. 468-472.

[149] M.A. Ibrahim, H.K. Roth, U. Zhokhavets, G. Gobsch, and S. Sensfuss, "Flexible large area polymer solar cells based on poly(3-hexylthiophene)/fullerene," *Solar Energy Materials and Solar Cells*, vol. 85, (2005), pp. 13-20.

[150] D. Gu, H. Baumgart, and G. Namkoong. "New template based nanoelectrode arrays for organic/inorganic photovoltaic applications," *Physica Status Solidi Rapid Research Letters*, vol. 5, no. 3, (2011), pp. 104–106.

APPENDICES

SOL-GEL TiO_X SYNTHESIS VIA ROTARY EVAPORATOR

Using a rotary evaporator eliminates the need for magnetic stirring and provides for better temperature control since the flask is uniformly heated over its entire surface. *The following setup procedures should be completed before making TiOx using the sol-gel process.*

1) Ensure cooling water is flowing through the condenser column from the building water system (middle two supply/return handles, water is supplied at 65°F)
2) Ensure N_2 is flowing from the generator to the filter/regulator, and then through the flasks/condenser column
3) Place N_2 exhaust tube in water-filled beaker next to silicone oil bath to monitor flow
4) Connect 120VAC to the evaporator and bath (two connections)

WARNING

Silicone oil baths can be extremely dangerous. Even at high temperatures (well above 212°F (100°C) where H_2O boils) silicone oil does not bubble or give any indication that it is very hot. Use caution and always assume the oil is hot even if the machine is turned off.

TiOx precursor sol-gel synthesis procedures ...

1) Clean the rotary and condensation flasks using the standard method (TCE, acetone, methanol, and ethanol with a DIW rinse between each solvent), blow dry with N_2, and place in the oven to dry for one hour.

2) Remove rotary and condensation flasks from the oven and install on the condenser column (see Figure 72).

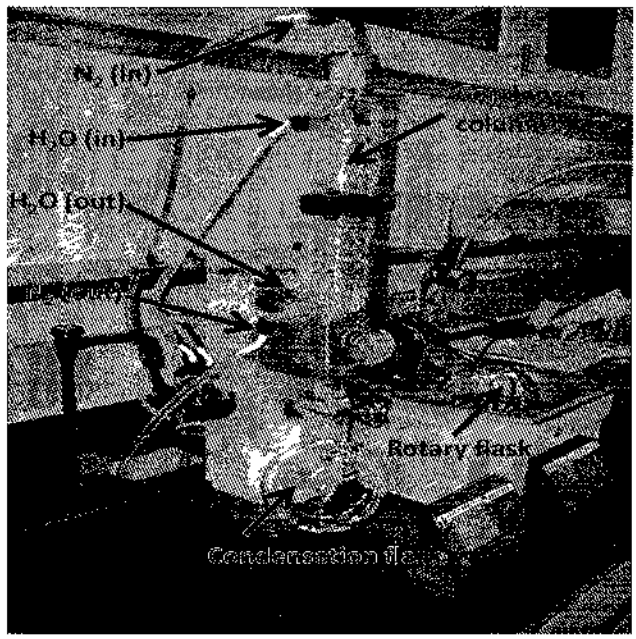

Figure 72. IKA Rotary Evaporator setup.

3) Turn on power to the rotary evaporator and silicone oil bath (each has its own switch).

4) Open cooling water supply/return valves on the wall (open the "return" FIRST to avoid an over-pressure condition on the condenser column and associated tubing).

5) Open the N_2 valve next to the filter/regulator (water in the beaker will start to bubble).

6) Lower empty rotary flask into the silicone oil bath (Figure 73).

7) Start flask rotation at 50 RPM.

8) Gradually bring temperature up to 120°C (If you get an "E26" error on the bath, switch it off, turn it back on, and start increasing the temperature again).

Figure 73. Rotary flask lowered into silicone oil bath.

9) Allow empty flask to rotate at 50 RPM and 120°C under N_2 for 1 hour to ensure all water is removed from the system.

10) At the end of one hour, **TURN TEMP DOWN TO 80°C**, stop rotation, and raise the rotary flask above the oil and allow it to cool to room temperature (about 20 minutes) – the oil will take longer to go down to 80°C – **Leave the N_2 flowing**

11) Once the rotary flask is at room temperature, remove the tape from the injection port and inject the TiOx precursors into the flask **IN THE FOLLOWING ORDER**:

    1) Titanium (IV) isopropoxide ($Ti[OCH(CH_3)_2]_4$) – **5mL**
    2) 2-methoxyethanol ($CH_3OCH_2CH_2OH$) – **20mL**
    3) Ethanolamine ($H_2NCH_2CH_2OH$) – **2mL**

12) Place tape over the injection port to stop the introduction of air into the system.

13) With the rotary flask still raised above the oil bath, start rotation at 100 RPM.

14) Allow precursors to rotate above the oil bath for 1 hour at room temperature.

15) Lower rotary flask into the 80°C silicone oil bath and allow it to rotate for 1 hour. Figure 74 below shows what the mixture will look like after the hour:

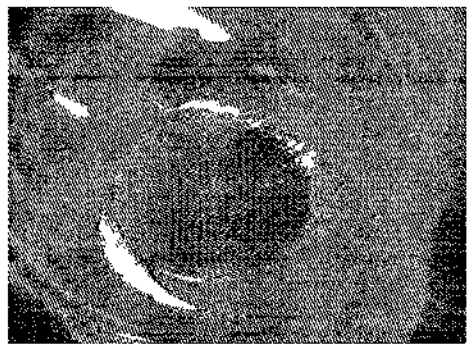

Figure 74. Mixture appears pink after 1 hour at 80°C.

16) Raise the temperature to 120°C – Do not raise the flask from the oil, increase the temperature by 5 degrees/minute from 80°C to 120°C, and rotate for one hour.

17) After one hour, the solution will be a darker red color as seen in Figure 75.

Figure 75. Mixture appears dark red after 1 hour at 120°C.

18) Raise the rotary flask from the oil bath, turn the temperature down to 80°C, and leave the mixture rotating under N_2 until the bath cools down to 80°C.

19) Lower the flask into the 80°C oil bath and allow to rotate for 1 hour.

20) Raise the temperature to 120°C – Do not raise the flask from the oil, increase the temperature by 5 degrees/minute from 80°C to 120°C, and rotate for one hour.

21) Raise the flask from the oil bath and allow to cool to room temperature (turn temperature down to 25°C).

22) After the flask reaches room temperature, open the injection port and inject 10mL of ethanol, methanol, or isopropanol – your choice of solvent will depend on which one you plan to use later as the dilution media prior to spin casting. If you are going to dilute with ethanol, then use 10mL of ethanol in this step. If you plan to use methanol, then use 10mL of methanol, etc.

23) Use a long syringe to extract the TiOx precursor from the rotary flask and store in clean 6mL vials as seen in Figure 76.

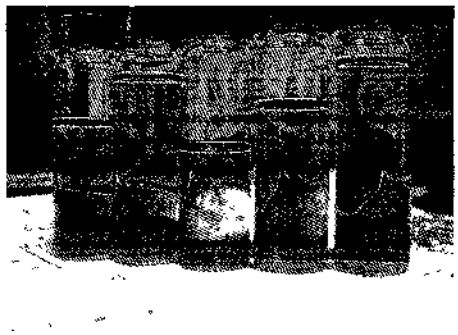

Figure 76. Sol-gel-produced TiOx material ready for dilution in ethanol, methanol, or isopropanol and subsequent spin-casting on solar cell active layers.

SUBSTRATE PREPARATION & CLEANING PROCEDURES

The following steps describe the process for preparation of useable substrates ready for OSC fabrication:

1) Use an ohmmeter to measure electrical conductivity of a 1" x 3" ITO/glass slide to determine which side is coated.
2) Using a diamond scribe, score the uncoated side and break into three 1" x 1" substrates.

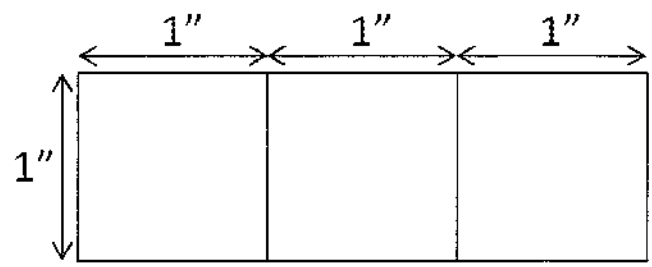

Figure 77. Scored 1" x 3" ITO/glass slide.

3) On the backs of each substrate, use the diamond scribe to mark the letter "B"; make this annotation in the middle and near an edge of the substrate.

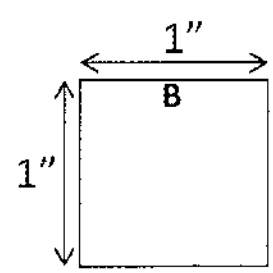

Figure 78. 1" x 1" substrate with backside marked.

4) To avoid a short-circuit condition in the fabricated device, it is necessary to remove the ITO in the area where the back electrode (an evaporated aluminum cathode) connection is made.

   a. Place silicone tape (0.5" x 0.25") over the ITO that is to be retained – ensure that it overlaps the edge of the slide tightly and wraps completely around.

   b. Carefully and firmly rub the tape to ensure that it adheres securely to the ITO and the back of the slide.

   c. Ensure the tape is pressed down sufficiently such that the acidic etchant cannot enter any cavities at the tape/glass interface and cause undesired etching of the protected ITO.

   d. Etch the exposed portion of ITO in an acid solution (20% w/v HCl, 5% w/v HNO_3) at 70°C.

   e. Fully submerge the slide into the heated acid solution for 5 minutes.

   f. Remove the substrate and place in a beaker containing deionized water (DIW).

   g. Check conductivity with an ohmmeter (the reading should show infinite resistance) and re-etch if necessary.

   h. When etching is complete, rinse the entire substrate with DIW and then remove the tape.

   i. Place substrate into a beaker containing ethanol and clean in an ultrasonic bath for five minutes.

   j. Remove substrate from beaker, rinse with DIW, and dry with N_2.

5) To prepare the substrate for OSC fabrication, follow the wet-cleaning process as detailed below.

   a. Use ultrasonic cleaning in DIW with a common glass-detergent (3% Mucasol) for 10 minutes at 60 °C.

   b. Rinse thoroughly with DIW.

   c. Sonicate in DIW for 10 minutes at 60 °C.

   d. Rinse thoroughly with DIW.

   e. Sonicate in ethanol for 5 minutes.

   f. Rinse thoroughly with DIW.

   g. Sonicate in acetone for 5 minutes at 40°C

   h. Rinse thoroughly with DIW.

The above cleaning steps should be repeated at least once. After the final DIW rinse, dry the substrate with N_2 and place in the oven to dry for at least one hour.

SPIN-CASTING OF POLYMERS AND SOLUTION-BASED OXIDE LAYERS

The outcome of spin-casting is dependent upon such factors as ambient humidity and temperature in the spin apparatus, temperature and concentration of the materials being spun, the solvent used, spin acceleration, terminal spin speed, and the time of spin. Air velocity is also as factor, so whether or not the lid of the spinner is open or not can have an impact. With so many variables involved, it's very difficult to control spin results. In fact, spinners made by different manufacturers that are set to the same spin parameters can actually produce different results.

PEDOT:PSS layer…

1) Using silicone tape, attach substrates to square holding slides and place on vacuum chuck on spinner in the fume hood.
2) Using a syringe, cover the substrate with PEDOT:PSS and spin at 3000 RPM for three minutes using ramp speed of 500 RPM/s (for a planar solar cell).
3) Remove the substrate from the spinner, remove the holding slide, and clean the anode area of the solar cell with a cotton bud dipped in acetone. It is not absolutely necessary to remove the PEDOT:PSS from the anode area because it has a high sheet resistance, but it is good practice to do so.
4) After cleaning the anode, place on the hot plate in the glove box, and anneal at 100°C for 5 minutes.
5) Remove substrate from hot plate and allow to cool to room temperature.

Active layer…

1) Prior to depositing the active layer, the PEDOT:PSS must be annealed in the glove box on the hot plate as per procedures in the previous section.
2) Using silicone tape, attach substrates to square holding slides and place on vacuum chuck on spinner in the glove box.
3) Using a syringe, cover the substrate with active layer and spin according to the parameters determined for the particular blend (e.g., HBG:$PC_{61}BM$, LBG:$PC_{71}BM$, etc.).
4) After spin coating, remove the substrate from the spinner, wet a cotton bud in acetone, and clean the active layer from the anode location.

TiOx layer…

1) Using silicone tape, attach substrates to square holding slides and place on vacuum chuck on spinner in the fume hood.
2) Using a syringe, cover the substrate with active layer and spin at 4000 RPM, 500 RPM/s acceleration, and 40 seconds.
3) After spin coating, remove the substrate from the spinner, wet a cotton bud in acetone, and clean the TiOx precursor from the anode location.
4) Place substrate on the hot plate at 80°C for 10 minutes in air.
5) Return to the glove box immediately after annealing until ready for further processing.

ELECTRON BEAM EVAPORATION OF ELECTRODE MATERIALS

The solar cell structure is placed on the substrate holder shown in Figure 80. There are nine masks on the substrate holder and each has the same configuration as the schematic on the right in the figure.

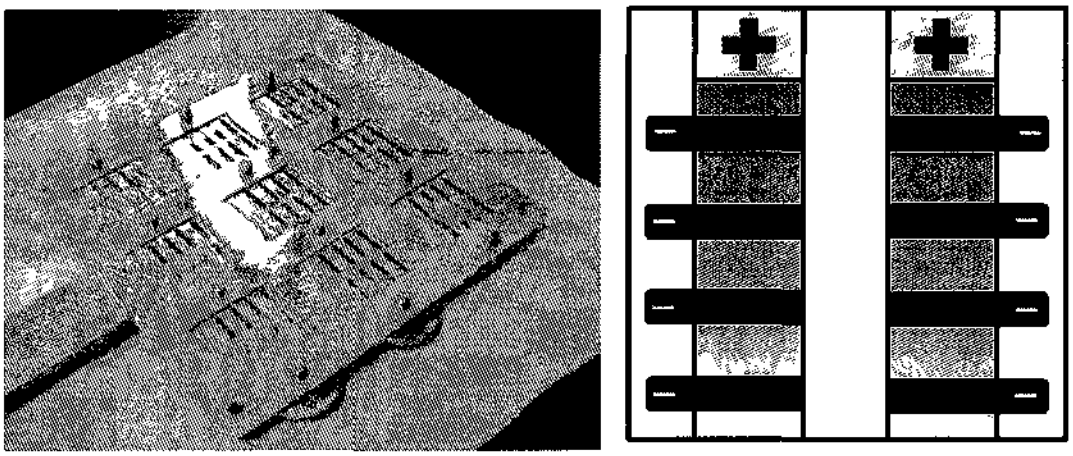

Figure 79. Nine-sample substrate holder and schematic of individual mask. Active areas are ~11 mm^2.

1) Using the Operational Manual for the Varian 3118 Electron Beam Evaporator, open the Bell jar to its maximum height.
2) After the substrate is secured to the holder, it is placed upside down in the electron beam evaporator (ebeam) above the aluminum target located in the crucible of the electron gun. Ensure there is no distance between substrate and holder as this causes "shadowing" and could cause a change in the size of the active area of the devices.
3) Ensure there is a sufficient amount of aluminum in the crucible and that the graphite liner is not cracked.

4) Close the bell jar.
5) Ensure cooling water is turned on to the electron gun, diffusion pump, and cooling trap.
6) Turn roughing pump on.
7) Open roughing valve on Automatic Valve Controller.
8) Turn diffusion pump on.
9) WAIT TWENTY (20) MINUTES – FAILURE TO DO SO WILL LIKELY DAMAGE THE DIFFUSION PUMP.
10) Open high-vac valve and wait ten minutes.
11) Wait until ion gauge pressure reaches at least 5e-6 Torr.
12) Turn on high voltage circuitry to the electron gun.
13) Deposit 100nm thickness of Al at a rate of 1-2 angstroms/second.
14) The melted Al target will appear orange in color. A "mist" will appear above the target – this is the evaporated aluminum rising up to the substrate.
15) The substrate is not heated as this would damage the polymer.
16) The deposition rate is maintained between 1 and 2 angstroms/second.
17) After deposition, cool down under vacuum for 30 minutes to account for differences in thermal coefficients between the polymer and aluminum.
18) The deposited Al should be very shiny and highly reflective.

COPYRIGHT PERMISSIONS / AUTHORIZATIONS

Chapter Three, Pages 71 – 79, "**OPTICAL SIMULATION: OPTIMIZING ACTIVE LAYER THICKNESS**", are based on the following journal article:

P. Boland and G. Namkoong, "**Optimization of Active Layer Thickness in Planar Organic Solar Cells via Optical Simulation Methods,**" *Japanese Journal of Applied Physics*, vol. 49, (2010), pp. 030205-1-3.

This paper was published in the Japanese Journal of Applied Physics and is made available as a part of this PhD thesis with the permission of the Japan Society of Applied Physics. This article can be found on JJAP Online at:

http://jjap.jsap.jp/cgi-bin/getarticle?magazine=JJAP&volume=49&page=030205

Chapter Three, Pages 79 – 92, "**OPTIMIZING LOW-BANDGAP PCPDTBT:PCBM SOLAR CELLS**", are based on the following journal article:

P. Boland, K. Lee, and G. Namkoong, "**Device Optimization in PCPDTBT:PCBM Plastic Solar Cells,**" *Solar Energy Materials & Solar Cells*, vol. 94, (2010), pp. 915–920.

Supplier: Elsevier Limited
The Boulevard, Langford Lane
Kidlington, Oxford, OX5 1GB, UK

Registered Company Number: 1982084

License Number: 2672631307099

License Date: November 12, 2011

Licensed Content Publication: Solar Energy Materials and Solar Cells

Licensed Content Title: Device Optimization in PCPDTBT:PCBM Plastic Solar Cells

Licensed Content Date: May 2010

Licensed Content Volume Number: 94

Licensed Content Issue Number: 6

Number of Pages: 6

Start Page: 915

End Page: 920

Type of Use: Reuse in a thesis/dissertation

Portion: Full article

Format: Both print and electronic

Dissertation Title: HYBRID INORGANIC/ORGANIC NANOSTRUCTURED TANDEM SOLAR CELLS: SIMULATION AND FABRICATION METHODS

Dissertation Completion Date: Dec 2011

Estimated Size (number of pages): 204

Chapter Three, Pages 92 – 109, "**ORGANIC TANDEM CELLS: LOW- & HIGH-BANDGAP DONOR POLYMERS**", are based on the following journal article:

P. Boland, K. Lee, J. Dean, and G. Namkoong, "**Design of Organic Tandem Solar Cells using Low- and High-Bandgap Polymer:Fullerene Composites,**" *Solar Energy Materials & Solar Cells*, vol. 94, (2010), pp. 2170–2175.

Supplier: Elsevier Limited
The Boulevard, Langford Lane
Kidlington, Oxford, OX5 1GB, UK

Registered Company Number: 1982084

License Number: 2672631307099

License Date: November 12, 2011

Licensed Content Publication: Solar Energy Materials and Solar Cells

Licensed Content Title: Design of Organic Tandem Solar Cells using Low- and High-Bandgap Polymer:Fullerene Composites

Licensed Content Date: December 2010

Licensed Content Volume Number: 94

Licensed Content Issue Number: 12

Number of Pages: 6

Start Page: 2170

End Page: 2175

Type of Use: Reuse in a thesis/dissertation

Portion: Full article

Format: Both print and electronic

Dissertation Title: HYBRID INORGANIC/ORGANIC NANOSTRUCTURED TANDEM SOLAR CELLS: SIMULATION AND FABRICATION METHODS

Dissertation Completion Date: Dec 2011

Estimated Size (number of pages): 204

Chapter Three, Pages 109 – 121, "**ORGANIC TANDEM CELLS: PCPDTBT:PC_{61}BM & P3HT:PC_{71}BM SUBCELLS**", are based on the following journal article:

G. Namkoong, P. Boland, K. Lee, and J. Dean, "**Design of Organic Tandem Solar Cells using PCPDTBT:PC_{61}BM and P3HT:PC_{71}BM,**" *Journal of Applied Physics*, vol. 107, (2010), pp. 124515-1-6.

Supplier: American Institute of Physics

License Date: November 12, 2011

Licensed Content Publication: Journal of Applied Physics

Licensed Content Title: Design of Organic Tandem Solar Cells using PCPDTBT:PC_{61}BM and P3HT:PC_{71}BM

Licensed Content Date: Jun 2010

Licensed Content Volume Number: 107

Licensed Content Issue Number: 12

Number of Pages: 6

Start Page: 124515-1

End Page: 124515-6

Type of Use: Reuse in a thesis/dissertation

Portion: Excerpt (> 800 words)

Format: Both print and electronic

Dissertation Title: HYBRID INORGANIC/ORGANIC NANOSTRUCTURED TANDEM SOLAR CELLS: SIMULATION AND FABRICATION METHODS

Dissertation Completion Date: Dec 2011

Estimated Size (number of pages): 204

Chapter Three, Pages 128 – 137, "**INFLUENCE OF ANNEALING ON POLYMER BLEND PROPERTIES**", are based on the following journal article:

P. Boland, S. S. Sunkavalli, S. Chennuri, K. Foe, T. Abdel-Fattah, and G. Namkoong, "**Investigation of Structural, Optical, and Electrical Properties of Regioregular Poly(3-hexylthiophene)/Fullerene Blend Nanocomposites for Organic Solar Cells,**" *Thin Solid Films*, vol. 518, (2010), pp. 1728–1731.

Supplier: Elsevier Limited
The Boulevard, Langford Lane
Kidlington, Oxford, OX5 1GB, UK

Registered Company Number: 1982084

License Number: 2672640118554

License Date: November 12, 2011

Licensed Content Publication: Thin Solid Films

Licensed Content Title: Investigation of Structural, Optical, and Electrical Properties of Regioregular Poly(3-hexylthiophene)/Fullerene Blend Nanocomposites for Organic Solar Cells

Licensed Content Date: January 2010

Licensed Content Volume Number: 518

Licensed Content Issue Number: 6

Number of Pages: 4

Start Page: 1728

End Page: 1731

Type of Use: Reuse in a thesis/dissertation

Portion: Full article

Format: Both print and electronic

Dissertation Title: HYBRID INORGANIC/ORGANIC NANOSTRUCTURED TANDEM SOLAR CELLS: SIMULATION AND FABRICATION METHODS

Dissertation Completion Date: Dec 2011

Estimated Size (number of pages): 204

COPIES OF ALL COPYRIGHT AUTHORIZATIONS ARE ON FILE

WITH THE OLD DOMINION UNIVERSITY REGISTRAR'S OFFICE

VITA

Patrick Michael Boland Jr.
Department of Electrical and Computer Engineering, KH 231
Old Dominion University
Norfolk, VA 23529

EDUCATION

Ph.D. Electrical and Computer Engineering, December 2011
Old Dominion University, Norfolk, Virginia
Dissertation: **HYBRID INORGANIC/ORGANIC NANOSTRUCTURED TANDEM SOLAR CELLS: SIMULATION AND FABRICATION METHODS**

Masters in Engineering Management, August 1996
Old Dominion University, Norfolk, Virginia

B.S. Engineering, Cum Laude, December 1990
University of South Carolina, Columbia, South Carolina

SELECTED PUBLICATIONS AND CONFERENCE PRESENTATIONS

Gon Namkoong, **Patrick Boland**, Si-Young Bae, Jae-Phil Shim, Dong-Seon Lee, Seong-Ran Jeon, Kurniawan Foe, Kevin Latimer, and W. Alan Doolittle, "Effect of III-nitride polarization on V_{OC} in p–i–n and MQW solar cells," *Physica Status Solidi Rapid Research Letters*, vol. 5, no. 2, (2011), pp. 86–88.

Patrick M. Boland Jr. and Gon Namkoong, "Simulation of Organic/Inorganic Tandem Solar Cells," *Virginia Space Grant Consortium Research Conference*, (2011).

Patrick Boland, Keejoo Lee, James Dean, and Gon Namkoong, "Design of organic tandem solar cells using low- and high-bandgap polymer:fullerene composites," *Solar Energy Materials and Solar Cells*, vol. 94, (2010), pp. 2170-2175.

Patrick Boland, Sri Sabarinadh Sunkavalli, Sampath Chennuri, Kurniawan Foe, Tarek Abdel-Fattah, and Gon Namkoong, "Investigation of structural, optical, and electrical properties of regioregular poly(3-hexylthiophene)/fullerene blend nanocomposites for organic solar cells," *Thin Solid Films*, vol. 518, (2010), pp. 1728–1731.

Patrick Boland, Keejoo Lee, and Gon Namkoong, "Device optimization in PCPDTBT:PCBM plastic solar cells," *Solar Energy Materials & Solar Cells*, vol. 94, (2010), pp. 915–920.

Patrick Boland and Gon Namkoong, "Optimization of active layer thickness in planar organic solar cells via optical simulation methods," *Japanese Journal of Applied Physics*, vol. 49, (2010), pp. 030205-1 – 030205-3.

Gon Namkoong, **Patrick Boland**, Keejoo Lee, and James Dean, "Design of organic tandem solar cells using PCPDTBT:$PC_{61}BM$ and P3HT:$PC_{71}BM$," *Journal of Applied Physics*, vol. 107, (2010), pp. 124515-1 – 124515-6.

Patrick M. Boland, Kurniawan Foe, and Diefeng Gu, "Estimation of organic tandem solar cell power conversion efficiency via optical simulation methods," *218th ECS Meeting*, vol. 33, Iss. 17, (2010), pp. 199-205.

Kurniawan Foe, **Patrick M. Boland**, and Diefeng Gu, "Controlled synthesis of ZnO nanospheres using hydrothermal process," *218th ECS Meeting*, vol. 33, Iss. 21, (2010), pp. 51-55.

Patrick M. Boland Jr. and Gon Namkoong, "A study of charge transportation at organic/metal oxide interfaces in bulk heterojunction solar cells," *Virginia Space Grant Consortium Research Conference*, (2010).

Patrick M. Boland Jr., Helmut Baumgart, Gon Namkoong, and Tarek Abdel-Fattah, "Optimization of active layer thickness in planar organic solar cells via optical simulation methods," *International Semiconductor Device Research Symposium* (ISDRS), vol. 2, (2009), pp. 1-2.

Sacharia Albin, Bing. Xiao, Makhin Thitsa, and **Patrick Boland**, "Tungsten oxide nanorods: synthesis and properties," *214th ECS Meeting*, vol. 802, Iss. 23, (2008), Abs. 1854.

Patrick Boland, Gopakumar Sethuraman, Alexis Mendez, Tom Graver, Dmitry Pestov, and Gregory Tait, "Fiber Bragg grating multichemical sensor," *Proceedings: The International Society for Optical Engineering (SPIE)*, vol. 6371, (2006), pp. 637109 – 637109 – 11.

Gregory B. Tait, Gary C. Tepper, Dmitry Pestov and **Patrick M. Boland**, "Fiber Bragg grating multi-functional chemical sensor", *Proceedings: The International Society for Optical Engineering (SPIE)*, vol. 5994, (2005), pp. 599407.

FELLOWSHIPS/SCHOLARSHIPS

Graduate Assistance in Areas of National Need (GAANN) Fellowship, August 2006 – August 2009.

Virginia Space Grant Consortium (VSGC) Graduate Research Fellow, August 2009 – May 2011.

POSITIONS HELD

Graduate Assistant (GRA): ODU Applied Research Center (ARC) located at Thomas Jefferson National Accelerator Facility (Jefferson Lab) under Dr. Gon Namkoong.

Fall 2008 to Present –

Developed fabrication methods for low-, and high-bandgap planar organic solar cells. Designed standardized solar cell structure and masks for use by all lab members to allow daily production of PV devices. Identified critical procedures and parameters for substrate preparation, spin-casting of solutions, annealing techniques, and electron beam deposition of electrode materials.

Developed fabrication methods for hybrid tandem inorganic/organic solar cells. Incorporated TiOx electron transport/optical spacing layers into dual tandem structures using all-solution methods.

SKILLS

Extensive experience installing, repairing, maintaining, and calibrating microelectronics cleanroom processing tools including:

Microwave Chemical Vapor Deposition System (MWCVD)
Plasma-Enhanced Chemical Vapor Deposition System (PECVD)
RF Sputterer,
Inductively-Coupled Plasma/Reactive Ion Etcher Systems (ICP/RIE)
Electron Beam Evaporation System
Nitrogen Glove Box
Solar Simulator
Diffusion/Oxidation Furnaces